Correlative analysis between sampling direction and the mechanical properties of the friction stir welded AA5083/AA6082 dissimilar joints

By

MOLEBOGENG OARABILE MMANYANE SEGAETSHO

Master of Engineering: Mechanical Engineering

in the Faculty of Engineering and Built Environment at the

Cape Peninsula University of Technology

Supervisor: Dr V. Msomi

Co-Supervisor: Mr V. Moni

Bellville

September 2022

DECLARATION

This is to declare that this document is the work of Molebogeng Oarabile Mmanyane Segaetsho and that it has never been submitted for academic reasons in the pursuit of any qualification.

Signature  Date: 08 March 2023

ABSTRACT

Welding is one of the most popular and established methods of joining metals. However, it can be difficult to weld aluminium (Al) and its alloys, or to create various joints between different types of aluminium, or between aluminium and other metals, by employing conventional welding techniques. Conventional techniques cause a variety of issues, including weak joints and changes in the mechanical characteristics of the materials. This makes it difficult for a number of cutting-edge and modern ideas to develop as a consequence. Friction stir welding (FSW), a method of solid-state material joining, provides a solution to these problems of weak joints and alterations of the mechanical properties by necessitating minimum heat to fuse materials. The FSW technique, in using a non-consumable tool, does not rely on additional welding consumables such as flux, filler metals, or post-welding treatment and can be applied on heat sensitive materials such as aluminium and its alloys. FSW and its influence on the mechanical properties of various materials forming comparable and dissimilar joints has been the subject of several studies.

This investigation intended to assess the relationship between the mechanical characteristics of the friction stir-welded AA5083/AA6082 dissimilar joints and the sample direction. A modified vertical milling machine was employed to weld two aluminium alloys, AA5083 and AA6082, each with a 6 mm thickness. With the aid of high-pressure water technology (waterjet), samples were collected while taking note of the start, middle and end locations in both the traversing and retreating directions. To evaluate the joint's quality and characterisation, visual tests, metallographic tests (including macro-structural and microstructural analyses and fractography), as well as mechanical tests (including tensile testing, three-point flexural tests and micro-hardness tests) were all performed. The results of the traverse, longitudinal and parent materials proved comparable despite the defects identified in the joint.

The macrostructure analysis of the traverse samples revealed all four major FS welded joint zones: the parent material zone (PM), heat affected zone (HAZ), thermo-mechanically affected zone (TMAZ), and stir zone (SZ). An inter-material flow pattern was observed, an evident indication that the material in the joint had plasticised, albeit not sufficiently judging by the tunnel defect present. As a result, there were no onion rings in any of the samples from any of the locations which explain the underdeveloped stir zone. Micro-voids were also discovered in the samples, predominantly on the advancing side, right under the material bands. The longitudinal examination of the samples revealed material stacking, as well as a tunnel flaw that extended across the sample.

The microstructure of the traverse samples revealed that the materials were subjected to considerable stress and high temperatures, resulting in dynamic recrystallisation of the joint materials. AA6082 possessed minute grains that resembled shards of glass, but AA5083 had no discernible grains. The mean grain size of the traverse start sample was 10.328 µm; the mean grain size of the middle sample was 11.884 µm and the mean grain size of the traverse end sample was 7.618 µm. The grain was measured in the longitudinal start samples at 15.608 µm; the middle sample measured 19.881 µm; and in the end sample at 9.187 µm. There was no obvious association between the microstructure and the location of the samples.

The stir zone was identified as the point of failure in each sample after tensile test analysis of the traversing samples. All samples showed a meandering tear, a slight necking, and a cup-cone fracture mode, a unique plastic deformation mode common in ductile materials. Samples taken at the start, middle, and end of the joint were recorded maximum ultimate tensile strength of 152.722 MPa, 130.694 MPa, and 122.278 MPa, respectively, at strains of 5.35%, 9.72% and 9.80%, respectively. At distances of 5, 11, and 10 mm from the bottom edge of the gripping end, the longitudinal tensile samples failed along the gauge. The longitudinal samples obtained from the joint's start location resulted in maximum ultimate tensile strength values of 137.417 MPa, 127.833 MPa, and 109.500 MPa, respectively, all at stresses of 13.8%, 8.3%, and 12.7%. The findings of the traverse and longitudinal samples indicated a weakening of the sample. The traverse samples that underwent face testing respectively measured 6.414 MPa, 47.513 MPa, and 78.575 MPa, indicating an increase in proportion to location while the longitudinal samples measured respective strengths of 218.05 MPa, 272.125 MPa, and 176.313 MPa. The traverse samples attained angles of 40°, 46°, and 150º, whilst the longitudinal samples reached an overall bending angle of 140º. The root tested traverse samples measured 196.438 MPa, 47.075 MPa, and 239.05 MPa, respectively. The maximum deflection angles for the traversal samples were 5, 10, and 20º. The longitudinal root tested samples from the SME locations had strength readings of 108.250 MPa, 198.888 MPa, and 196.438 MPa, respectively. The start, middle, and end samples of the longitudinal samples had bend angles of 140° and 135°, respectively.

The traversal start sample's mean $HV_{0.2}$ value was determined by micro-hardness assessment to be 79.70. The mean values for the samples' longitudinal halves, AA5083 and AA6082, were 100.59 $HV_{0.2}$ and 104.84 $HV_{0.2}$, respectively. After accounting for the mean micro-hardness values derived from both the parent samples and the welded samples, the joints had a greater micro-hardness than that calculated from the parent materials. While the AA5083 and AA6082

sections both registered 73.385 $HV_{0.2}$, the traverse middle sample registered 75.152 $HV_{0.2}$. When compared to the PMs results, the mean micro-hardness values of the samples revealed a drop. The mean micro-hardness of the traverse end sample was determined to be 78.79 $HV_{0.2}$. The mean micro-hardness values were 79.555 and 76.641 $HV_{0.2}$ for the longitudinal AA5083 and AA6082 sections, respectively. The hardness and grain sizes are correlated, according to the Orowan mechanism and the Hall-Petch.

The start, middle, and end traverse samples' fractographic analysis revealed micro-voids and tunnel defects. The image at high magnification shows several dimples of various sizes. The samples also had cleavage facets and voids. The material's ductility is confirmed by the emergence of large dimples, which indicates that the material has gone through a suitably malleable course. The bigger dimples at the bottom were found to have bases of shattered particles, which was determined to be the reason for the joint's fragility. Surface cleavages and micro-voids on the longitudinal sample suggested ductile and brittle fractures. The picture showed portions with smooth surfaces and others with dimples of various sizes at extreme magnification. Similar to the traverse samples, the dimples contained particles embedded at the bottom of them.

No trend was observed to ascertain that longitudinal or traverse samples performed better than parent materials over a range of locations. The study will advance the knowledge of the impact of friction stir welding on aluminium and its alloys and deepen the comprehension of those effects. It will also open new avenues for the investigation of cutting-edge solutions to contemporary issues in many sectors.

Keywords: Friction Stir Welding, correlation, sampling direction, aluminium alloys, dissimilar joints, (AA5083/ AA6082), mechanical tests, microstructure.

PAPER PORTFOLIO

Segaetsho, M.O.M., Msomi, V. and Moni, V. *Corrosion behaviour of friction stir welded dissimilar joints produced from AA5083 and other alloys of aluminium: A critical review.* Materials Today: Proceedings, Volume 56, Part 4, 2022, Pages 1696-1701

ACKNOWLEDGEMENTS

Words could never fully express my gratitude. This voyage, like many others that have gone before it, was not simple, and it is not something to which you can become used to. I have cried a lot and had sleepless nights during the course of this work. Of course, we all do at some time in our lives, but every journey is unique since we never get to tell the same narrative. I am not sure where to begin, but all I know is that neither this page nor any other book could ever be sufficient to should you all just how grateful I am. I have, if anything, been blessed several times during my lifetime to have the support structure that I have, from my supervisors and friends, but most of all my beloved family.

To the BIG 5 (Thabo, Mmakgori, Tumisang and Thabo II Segaetsho), to my aunt Lucia Sina Mamoralo Seate (Mommy) and siblings Mabaka and Ramoeti Seate and Maria "Nane" Mathe, I could say thank you for the entire of my existence. One may say those are just words, but a mere thank you could never sum up for all you are and what you have done for me. There is no greater love than what I have witnessed in each and every one of you. Thank you for your encouraging words, warm embraces, and kisses as well as for just being there for me in all I do.

Dr. Tawanda Marazani, you have always shown faith in my ability to improve and advance intellectually. You have been one of my biggest supporters, constantly motivating me to keep going in the face of any difficulty. From my undergraduate days to the present, I want to thank you for being there for me at every turn.

I hope it has been as pleasant for you as it has been for me, Dr. Msomi, Mr. Moni, and Dr. Mabuwa. Thank you for allowing me to learn from you, for your time, effort, and every encouraging remark. It was not always easy for me, however, I gave it my all and hope I did not disappoint. Thank you for believing in me and trusting me as you have.

Thank you to Ms. Shaheeda Petersen. You have always saved the day for me. Thank you for being patient with me each time I visited the lab and for imparting your expertise. Mr. Malwande Masekwana, you gave me my first lesson on the application and fundamentals of FSW in my Diploma year. I appreciate your on-going encouragement and support both now and throughout the years.

To the Mechanical engineering workshop stuff, thank you for letting me be a part of you and for always making me feel at home, where support is plentiful. For funding my education, I would like to thank the postgraduate office at Cape Peninsula University of Technology.

The only way I can express my deepest gratitude to my friends, Ms. Matshidiso Kgosimore, Ms. Mankgoana Mosisili, Ms. Kebaeditse Botswe, Ms. Dieketso Rakatana, Ms. Lisa Kadzutu, Mr. Sam Molefe, Mr. Thabiso Sebecho, Mr. Aobakwe Thupaemang and Mr. William Mukind is through prayer. I pray for you all to be richly blessed and that we all rise to become the best versions of ourselves that we were meant to be. I appreciate you all being an example that not all friendships are ones that end in the deep.

TABLE OF CONTENTS

LIST OF TABLES

LIST OF ILLUSTRATIONS

LIST OF EQUATIONS

ABBREVIATIONS

AA- Aluminium Alloy

AD- Advancing Side

ASTM- American Society of Testing Materials

BHN- Brinell Hardness Number

BM- Base Metal

DT- Destructive Test

EDXS- Energy Dispersive X-ray Spectroscopy

EISM- Electrochemical Impedance Spectroscopy Measurement

EN- European Standard

FS- Friction Stir

FSW- Friction Stir Welding

GDOES- Glow Discharge Optical Emission Spectroscopy

HAZ- Heat Affected Zone

HCHCr - High Carbon High Chromium

HV- Vickers Hardness

ID- Identification

ISO- International Organization for Standardization

Mg- Magnesium

Mn- Manganese

MUTS- Maximum Ultimate Tensile Strength

MPa- MegaPascal

NDE- Non-Destructive Evaluation

NDT- Non-Destructive Test

PWHT- Post-Weld Heat Treatment

PM- Parent Material

PMs- Parent Materials

RS- Retreating Side

SD- Standard Deviation

SEM- Scanning Electron Microscope

SKPFM - Scanning Kelvin Probe Force Microscopy

Si- Silicon

SME- Start, Middle and End

SZ- Stir Zone

TMAZ- Thermo-Mechanically Affected Zone

TS- Technical Specifications

TWI- The Welding Institute

CHAPTER 1

1.1 Introduction

Welding of materials is an ancient method faced with varied challenges prompted by the ever-increasing demand for innovative designs fitting for the current times. Currently, varied materials are used in single components or structures as an attempt to improve their performance and functionality most fitting for present day life and without compromising their strength. As these design modifications take place, modern methods are warranted able to meet the standards that ensure that designs are of improved quality. The welding of aluminium is a long-standing challenge. Aluminium has been used for various applications, in numerous ways and across multiple industries. The material is most commonly applied for construction purposes of enormous structures like airplanes, ships and space crafts. With that said, it is essential to study modern technologies and their effect on the materials to acquire the necessary knowledge to improve these technologies and their applications to enable the emergence of greater designs across industries.

Being the third most popular element following oxygen and silicon, aluminium in its pure form is rather weak; thus, it was necessary to develop suitable alloys for aluminium to be useful as a structural metal [1]. Over the last half-century, while aluminium has trailed iron in industrial use, it was recognised as having the potential to be used in engineering long before it became an industrial metal [2]. Al and its alloys possess some exceptional properties – their machinability, recyclability, high tensile strength and light weight – rendering them better than other many other materials such as steel that have been used previously [3].

The application of the material has seen immense growth in copious industries in attempts to manufacture products that are more conscious of the environment and its conditions. Al usage encompasses households, aircrafts, railway cars, boats, space crafts, and other components used in the already mentioned areas. The use of Al enables the reduction of carbon dioxide emissions, weight and fuel consumption while optimising the general performance of products in, but not limited to, the automotive industry, construction, transport and aeronautics [4].

While pure aluminium has quite exceptional properties, especially as it is corrosion resistant with high electrical conductivity, it is known for being soft and ductile. Thus, the addition or presence of alloying elements improves its machinability, further making it either heat treatable or non-heat treatable by improving hardness and reducing adhesion to the cutting tools [5]. In 1906, Alfred Wilm discovered the basic procedure for heat treating some aluminium alloys where the precipitation hardening techniques have been used to strengthen a variety of automotive and aerospace components today [6].

As alloys possess a combination of formidable properties, they are multipurpose and quite cost-effective to use. These non-ferrous metals have realised a far-reaching use in domestic, commercial and industrial spaces. Al alloys are classified into separate series classes based on the alloying metal used, from the AA1XXX series to the AA8XXX series [7]. The materials possess prodigious physical and mechanical properties, including augmented corrosion resistance properties, qualifying them for application in the marine environment. Table 1.1 below details the alloys, their alloying elements and their classification.

Table 1.1: Heat treated, non-heat-treated alloys and elements [8]

Heat treated alloys	Elements	Non-heat-treated alloys	Elements
2XXX	Al, Cu, Mg	1XXX	Al
6XXX	Al, Mg, Si	3XXX	Al, Mn, Mg
7XXX	Al, Zn, Mg	4XXX	Al, Si
8XXX	Al, Li, Cu, Mg	5XXX	Al, Mg

Some of the most commonly used alloys for construction purposes rise from the 5XXX and 6XXX families. Due to their adequate strength and great corrosion resistance properties, the 5XXX and 6XXX are the most preferred alloys, especially in corrosive environments such as seawater [9]. AA5083 is a high strength material which is found in multitudes of components in the marine, automotive and mine industries, known to resist damage caused by seawater and chemicals. AA6082 is a medium strength material; its application can be seen in construction and automobile industries. These materials can be used in conjunction with each other or individually. Table 1.2 below details the quantity of each of the elements in AA5083 and AA6082.

Table 1.2: Alloys and chemical composition percentages [10]

Alloy	Composition %								
	Al	**Si**	**Fe**	**Cu**	**Mn**	**Mg**	**Cr**	**Zn**	**Ti**
5083	Balance	0.11	0.31	0.06	0.52	4.71	0.07	0.12	0.02
6082	Balance	0.93	0.18	0.008	0.55	0.60	0.011	0.002	0.011

Many factors influence or contribute to the corrosive behaviour of materials. All surroundings are in some way destructive including gases, fuel gases, water, oils, soils and solvents [11]. Metal corrosion is regarded as one of the most hazardous kinds of corrosion, potentially leading to the debilitation of structures [12]. This may be a slow or rapid process depending on the surrounding medium (water, natural environment, underground or the atmosphere), causing damage by degrading the materials of machines, structures and other metallic equipment materials, in turn then, lowering the overall value of the product.

The deterioration of metals or metal properties, including chemical, mechanical and aesthetic, can result from reactions with chemical solutions or other harsh conditions [13]. Corrosion manifests itself in three ways: as attack on the overall surface progressively decreasing the material thickness; secluded corrosion attacking only the surface; and lastly, corrosion along grain boundaries where there are dissimilarities to the resistance of corrosion [14].

There are different categories of corrosion that may occur on metals categorised under eight types, based on appearance [5]. These categories are inclusive of uniform, pitting, crevice, inter-granular and galvanic corrosion as well as erosion-corrosion, de-alloying and environmentally-assisted cracking. Industries including transport, construction and manufacturing experience degradation of materials on their components. In chemical and petroleum industries, the leakage of oil and gas may allow for seepage of water leading to possible corrosion of the internal or external surfaces of components [15].

Al is well known for its high corrosion resistivity related to the formation of an aluminium oxide coating on its surface. A bayerite coating on metal submerged in water at temperatures below 70 °C and in seawater dissolves more quickly, with the chloride ion inhibiting the repair [16]. However, Al can still be affected by corrosion. The susceptibility of Al alloys to corrosion is due to the quality and content of alloying metals [17].

Al alloys realise degradation in various forms including pitting and crevice corrosion in saline conditions such as those found in marine environments caused by the adsorption of an anion, specifically the chloride ion (Cl) at the oxide solution interface [18]. Materials may be susceptible to corrosion as a result of the establishment of a new material resulting from the dissimilar joint produced through FSW material processing of dissimilar blanks or by the alteration of the electrochemical and mechanical characteristics in FS welded similar joins [19].

Quality assessments of welds allow for the determination of the weld's integrity. The assessment of joints comprises two categories of tests: namely, destructive or non- destructive. The tests provide information on the physical condition of joints using varied techniques to allow for exposure of any or all alterations to properties and defects in a welded joint. The difference between destructive and non-destructive tests is that non-destructive tests allow a physical examination of samples without changing their properties or functional utility, whereas destructive tests require damaging samples to expose surfaces of interest which may allow for defects that are not detectable using non-destructive testing methods [20].

Visual, penetrant, ultrasonic, radiographic, eddy current inspection and non-destructive evaluation (NDE) techniques (nonlinear vibrometry, JENTEK MWM®-arrays) are among the non-destructive testing methods for discovering faults in friction stir welded joints [21]. In addition to the non-destructive tests already mentioned, another test called magnetic particle testing is employed in the detection of surface and minor subsurface discontinuities or defects in ferromagnetic materials [22, 23].

Tension, fracture hardness, shear, bend, hardness, corrosion and break tests are several of the mechanical tests governed by the American Society of Testing Materials (ASTM) standards, which describe the significance of each test, the test apparatus, the preparation of the test specimens and the test procedure [24, 25].

1.2 Friction stir welding

In 1991, The Welding Institute (TWI) in the United Kingdom introduced FSW, an invention by Wayne Thomas as a technique initially applied to aluminium alloys [26]. The technique is regarded as one of the solid-state processes, requiring low heat inputs to join materials along with ultrasonic, cold, friction and explosive welding techniques. Solid-state welding is grounded on the principle of solid-state interatomic bonding, producing weld joints without requiring them to be liquefied, known as plastic deformation [27].

1.2.1 Principle of operation

The application of FSW involves plunging a rotating non-consumable tool in material until its shoulder is in contact with its surface. This contact, increasing the heat between the two surfaces due to friction, softens the material. Another contributing factor to the heat is the adiabatic heat produced all through plastic deformation of work pieces around the rotating tool which also aids in containing the material which may flow out and produce flash [28]. Plastic deformation at high temperature softens the material around the pin; this material is moved as the tool pin traverses along the joint line to complete a weld bead. A three-dimensional diagram of the FSW application is illustrated in Figure 1.1. The diagram shows the tool's advancing and retreating sides, leading edge, shoulder, and pin, as well as three arrows representing the tool's rotation (rotation arrow), plunging (down arrow), and travel direction (diagonal arrow).

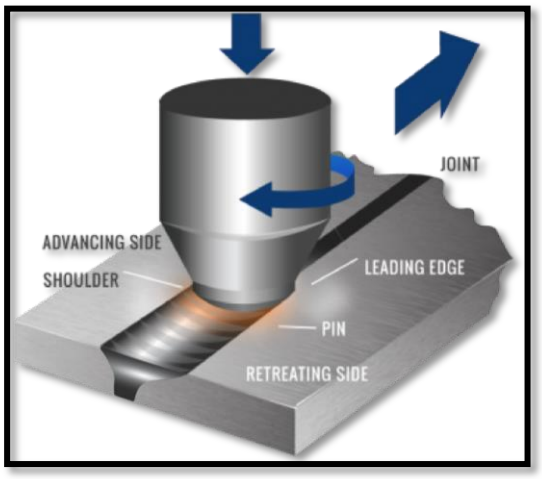

Figure 1.1: Friction stir welding [29]

Using a non-consumable tool, the process of FSW requires no additional welding consumables like flux; filler metals are not required, nor is post-welding treatment. The process is considered quite economical and efficient, more so for applications on nonferrous metal alloys than for ferrous metal alloys [30]. The method has advanced substantially in the metal industry, especially as the world aims towards more _green‘ or eco-friendly methods to evade negative contributions to the fast-deteriorating environment. The energy usage of FSW is observed to be 42% in comparison with Gas Metal Arc Welding (GMAW), using 10% less material for similar maximum tensile design. This results in a 31% reduction of greenhouse gas emissions [31]. Additionally, this process offers improved mechanical and metallurgical properties with no or only trivial defects as compared to conventional welding techniques [32]. However, its access into smaller establishments has been limited because of the high price of the equipment and the high initial costs for the acquisition of materials and components best suited for constructing the system.

1.3 Problem statement

Emanating from the background, aluminium applications in various industries have escalated rapidly because of its properties: it leads to lightweight, robust, corrosion resistant and aesthetically pleasing innovative and contemporary designs. Fusion welding has been the predominately applied and most favourable permanent joining technique for aluminium and its alloys. However, its applications are limited, unable to produce welds of dissimilar materials and may lead to undesired defects of joined materials due to chemical compositions. This limits the exploration of many innovative ideas because alterations to the metallurgical and mechanical properties of the joined metals may cause undesired defects andresult in poor designs.

The preceding statement permitted the subsequent research questions:

- What is the correlation between the sampling direction and the mechanical properties of friction stir welded AA5083/AA6082 dissimilar joints?
- What is the effect of sampling position on the mechanical properties?
- What similarities or differences can be observed between sample direction and sample position?

1.4 Background

The application of aluminium has grown enormously with increasing demand for modern designs to adhere to very particular specifications, including maintenance, performance, magnitude, contour, aesthetic, ergonomic and environmental factors. At most,this can be achieved by introducing the use of varied materials that are lightweight, corrosion resistant, aesthetically pleasing, but most importantly, tough. The most commonly used material joining techniques include soldering, brazing, adhesive bonding, mechanical fastening and welding. And the most commonly used of these techniques, especially for more permanent and sturdy structures, is welding. Welding is the favourable permanent material joining method for metals used where other joining methods have proven inadequate to construct structures which must perform a particular function.

Every so often, varied materials may be used in the construction of sole structures, but this can prove challenging through the various welding techniques. To date, including hybrid types, there are more than 75 types of welding techniques accessible to manufacturers for processing materials [33]. The most commonly applied of the welding techniques for aluminium includes Gas Tungsten Arc Welding (GTAW) and Gas Metal Arc Welding (GMAW) [8]. Gradually, these techniques become antiquated with the advancement of technology and the need for unprecedented modern designs, often requiring the use of dissimilar materials to produce joints. However, due to the variances in the material compositions, which contribute to their mechanical and metallurgical properties, such joints are often difficult to achieve.

Heat in welding is essential; conversely, it is also a contributing factor to the challenges associated with material joining, particularly with dissimilar joints. According to Godiganur and Biradar [34], significant welding drawbacks are especially noticeable during the solidification process in conventional welding of aluminium alloy, rendering undesired defects like distortion, weak or defective joints and inadequate fusion. This may lead to structure instability or even complete failure with detrimental consequences. Porosity, hot cracking, and incomplete fusion are a few observable defects with this form of welding of aluminium [3].

Friction stir welding (FSW) is a modern and uniquely innovative technique that has been introduced to the world of engineering for overcoming many of the challenges associated with fusion welding or conventional welding, especially concerning welding of dissimilar metals of

different properties. The technique has achieved great success in research, having demonstrated advantages typically unattainable by conventional welding and other permanent fastening methods [35]. The first partial use of aluminium in bridge construction was in 1933, with the Smithfield Street Bridge in Pittsburgh as the first of its kind; later, in 1950 and 1996, the Arvida and Forsmo bridges (Figure 1.2), respectively, were completed in an attempt to improve load carrying capacity over the existing steel and wood types [36].

Figure 1.2: Arvida and Forsmo bridges [36]

Other construction composed of aluminium can be found in a different industry. These, however, were made after the advent of the FSW process which made its way into the marine industry. Companies in the marine industry, for example, have used FSW to create massive metal panels built from aluminium extrusion profiles. Sapa created the first friction stir welded freezer panels (Figure 1.3) in 1996 to keep fish trawlers frozen [37]. FSW was also used to complete the riveting of numerous components of the Eclipse 500 business aircraft (Figure 1.4) [38].

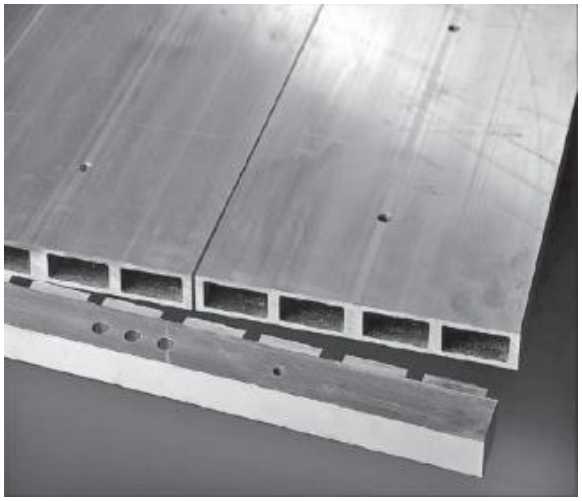

Figure 1.3: Sapa friction stir welded freezer panel [37]

Figure 1.4: Eclipse 500 business jet [38]

1.5 Aims and objectives

This study aims to establish and define the correlation between sampling direction and the mechanical properties of the friction stir welded AA5083/AA6082 dissimilar joints. The following objectives will be functional in attaining the study's aims:

- Execute friction stir welding to produce AA5083/AA6082 dissimilar butt joint with a reconfigured milling machine.
- Extract samples from three points along the joint at the tool plunging, traverse and tool exit in both transverse and longitudinal directions.
- Perform mechanical tests, including tensile tests, three-point flexural tests, micro-hardness tests, corrosion test and fractography, and macrostructural and microstructural analysis, to ascertain the quality of the weld joints.
- Establish the correlation of sampling direction on mechanical properties and characterise the samples extracted transverse and longitudinal to the joint.

1.6 Research significance

The research on the correlative analysis between sampling direction and the mechanical properties of the friction stir welded AA5083/AA6082 dissimilar joints should contribute to an understanding of the similarities and differences of samples when considering sampling directions and sampling positions from a welded joint. The intent is to acquire knowledge and to contribute to an in-depth understanding of the effects of friction stir welding on aluminium and its alloys.

- Experiments and secondary data sources including books, journals, articles and web pages.

1.7 Dissertation organisation

Chapter 1: This chapter contributes a comprehensive introduction into aluminium and its welding. It is inclusive of a problem statement, the background (covering both classic and modern methods for welding aluminium) and examples of various aluminium structures processed with friction stir welding. It further presents the aims and objectives and importantly, the significance of this research.

Chapter 2: This chapter presents an overview of previous research on the issues under examination. It investigates friction stir welding parameters, metallographic and fractography analysis, mechanical and chemical testing of similar and dissimilar joints made of aluminium alloys 5083 and 6082, corrosion of friction stir welded joints, and sampling direction and sample extraction position.

Chapter 3: This chapter describes the experimental organisation and execution of friction stir welding in this study, as well as sample preparations and assessment using metallographic and fractography analysis.

Chapter 4: This chapter introduces; analyses and discusses the results obtained throughout the study.

Chapter 5: This chapter concludes the study based on the results attained and offers endorsements for prospective work.

CHAPTER 2

LITERATURE REVIEW

2.1 Introduction

Much research on the friction stir welding (FSW) procedure has been undertaken to acquire a better understanding of the process. This required significant research into a variety of areas – the equipment, variables or parameters, the application and a variety of quality assurance procedures – to thoroughly grasp the technique's performance and superiority over traditional approaches. Much of the research was successful, resulting in new information about the process and other factors that has served to advance the technique into more sectors. The following section presents the findings of some of the research into the application of FSW on similar and dissimilar joints on 5083 and 6082 aluminium alloys (AA). It will primarily concentrate on the FSW of variable and invariable joints incorporating AA5083 and AA6082 testing.

2.2 Friction stir welding parameters

The application of FSW works on the principle of utilising customised parameters for specific joint designs, whether similar or dissimilar. These parameters hold great supremacy over the outcome of the joints and their quality. This section reviews some of the work that examined parameters and tests conducted to ascertain the optimality of the joints.

2.2.1 Parameters for FSW of AA5083

The high magnesium (Mg) content of AA5083 boosts its physical strength. AA5083, like other non-ferrous metals, is usually difficult to weld using traditional techniques due to high heat input required to generate a weld, which affects the mechanical qualities and results in poor joints. The friction stir welding of AA5083 is described in the following section.

The outcome of tool rotating speed on mechanical attributes of aluminium alloy 5083 weldments in friction stir welding using a 24 mm shoulder diameter high-speed steel (HSS) tool with a 6 mm diameter pin with length of 3.7 mm on 4 mm thick plates was reported [39]. The researchers found that high gyratory speeds lead the generation of coarse grains owing to high heat input which outcomes in a lower tensile strength of joints. From the empirical speeds, 1120 rpm and

40 mm/min were identified as creating superior mechanical properties compared to the other speeds with tensile strength and elongation percentage values of 203.5 MPa and 12.4%; this concurs with the fine grains identified in the microstructure. Microhardness tests, however, elucidated that the hardness of joints produced at 900 rpm was 97.93 HV, while those produced at 1120 rpm were 92.27 HV.

The results of welding variables on microstructure and mechanical characteristics of friction stir welded EN AW 5083 H111 plates on 6 mm thick plates were studied [40]. Two different H13 tools (threaded circular and triangular) with 20 mm shoulder diameters were used at rotating and traverse speeds of 800 rpm and 80 and 125 mm/min sequentially, at a tool inclination of 2º and a dwell time of 30 seconds. Regardless of the tool pin shape, both tools produced joints with high ultimate tensile strength (UTS) and elongation percentage values, with all joints fracturing at the nugget zone at both traverse speeds. In tests, the ultimate tensile strength of samples welded at 800 rpm and 80 mm/min was 309 to 311 MPa, while those welded at constant rotation speed and 125 mm/min showed values of 277 to 258 MPa. Triangular pin joints have a 97% joint efficiency.

To establish an understanding of the mechanical properties, effects of temperature variations and dissemination on FS welded joints, a study on friction stir welding of aluminium alloy 5083-H116 similar joints on 6.3 mm thick plates in a butt joint configuration was conducted [41]. An 18 mm diameter tool was used with rotary speeds of 450, 560 and 710 rpm, traverse speeds of 69, 86 and 116 mm/min, an angle of 2º, a dwell time of 20 seconds, and a plunging depth of 0.25 mm. At 560 rpm, nugget zone hardness decreased slightly, but at 700 rpm, hardness dropped considerably due to increased frictional heat, resulting in dynamic recrystallisation. According to their findings, the optimum settings in this study produced the greatest tensile strength of 330.58 MPa, resulting in 95.8% joint efficiency at 450 rpm and116 mm/min rotational and traverse in the order given.

The influence of process parameters on micro-hardness and mechanical properties of FSW aluminium 5083 alloy butt joint was reported [42]. Researchers used an 18 mm shoulder diameter straight cylindrical H13 tool on 4 mm thick plates at rotational and welding speeds of 700, 900, and 1100 rpm and 60, 80 and 100 mm/min at tilt angles of 90°, 90.5° and 91°. At a tool revolving speed of 1100 rpm, a traverse speed of 100 mm/min and a tool tilt angle of 91º, fault-free welds were attained. According to the study's findings, the tool rotational speed had minimal effect on the weld's heat input and tensile attributes; the attributes were likely controlled by heat contribution rather than mechanical deformity. The researchers concluded that optimising joint properties

entails varying traverse and rotational speeds as they extensively impact the mechanical characteristics of a weld.

2.2.2 Parameters for FSW of AA6082

The medium-strength alloy AA6082, with high silicon (Si) and magnesium content (Mg), is well-known for its strong resistance to corrosion. AA6082, like other non-ferrous metals, is difficult to weld using typical techniques due to the large heat input necessary to make a weld, resulting in poor mechanical qualities and defective joints. The friction stir welding of AA6082 is described in the next section which examines the ideal settings for friction stir welding of the material.

The designs of friction stir welding tools and their outcome on the welding AA-6082 T6 5 mm thick plates were studied [43]. Researchers discovered that the concave shoulder tool generated defects-free joints when used with four AISI H13 threaded pin tools (flat, concentric, scroll and concave shoulder) at a rotational rate of 1000 rpm and traverse speed of 100 mm/min and plunging depths of 4.93, 4.3 and 4.8 mm. The researchers note that FSW comprises of three phases: plunging, dwell, and tool traversing, all of which are required for a successful weld. [43] explain that the heat and stirring softens the material at the shoulder, allowing the tool to maintain contact with the work piece in both diagonal (X) and adjacent (Y) directions. However, because the concave area acts as a reservoir, filling up with softened material and potentially pushing the tool away from the work piece, additional force is required for successful joint formation. Furthermore, the researchers state, to achieve operability of shoulder design, the tool gradient should be at 2° to 4° and travel should be in the opposite direction.

The impact of procedure parameters on the perpendicular forces produced during friction stir welding of AA6082-T6 and on the mechanical characteristics of the joints on 2 mm thick plates was examined [44]. A 12 mm shoulder diameter truncated cone tool with a 30° pin angle, a base diameter of 3.5 mm and height of 1.7 mm; rotational and traverse rates of 1200, 1500, and 2500 rpm and 30, 60, and 100 mm/min, respectively; 20 seconds dwell time, and a tool tilt angle of 2º at 0.1 mm plunging depth was used in this study. Tensile tests were undertaken in conjunction with ASTM E8 and BS EN 895 standards, each repeated thrice. In this study, the mechanical attributes of the joints were assessed in relation to the process variables and the correlations between ultimate tensile strength, ultimate elongation and vertical force. From the results, it was observed that with a surge in rotating speed, the accompanying heat input enables provision of higher work-

piece temperatures, softening the material and reducing its vertical force during FSW. Fractures of the tested samples occurred in the heat affected zone (HAZ) regardless of the varied speeds being investigated. The results exhibited that the process parameters at 2500 rpm and 60 mm/min offer the optimum balance between the requirement to capitalise on mechanical qualities and the demand to decrease perpendicular force. However, the traverse speeds up to 60 mm/min endorsed an increase in ultimate tensile strength and elongation. Researchers pointed out that at 1200 rpm, ultimate tensile strength and vertical strength, as well as ultimate elongation and perpendicular force, are directly connected, and that the difference in particle and grain size becomes more apparent as FSW is performed at maximum welding and rotating speeds. [44] also pointed out that as rotational speeds increase, more intricate linkages between mechanical properties and vertical force are produced.

Gopi and Manonmani [45] investigated process parameters like rotational speed, traverse speed, shoulder penetration, and pin and shoulder profiles to explore how shoulder profile and shoulder penetration altered joint strength in friction stir welded AA6082 on 4 mm thick plates, at 700, 900, 1100, 1300 and 1500 rpm; and 48, 96, 144, 192 and 240 mm/min; 12 mm shoulder diameter high carbon high chromium (HCHCr) steel tools with heptagon, hexagon, pentagon, square and triangle tool 4 mm pin profiles with taper angles of -10° -5°, 0° -5° and 10° were used, with plunging depths of 0.00, 0.04, 0.08, 0.12, and 0.16 mm. The Taguchi Experimental Design method was employed to investigate the impact of various elements and measure the tensile strength of the joints; the American Society for Testing of Materials (ASTM E8) standard was used. The tensile samples bared fractures occurred at the retreating side of the heat affected zone, indicating that the joint established between the two panels is solid. The authors state that rotational and weld speeds, are crucial. The researchers indicate that substantial heat is generated with the combination of considerable rotational and lower traverse speeds, which ensures that plasticising of material and overcoming of adhesion of material onto the tool is sustained. Taking shoulder penetration and profile into account, the researchers suggest that increasing shoulder penetration results in increased tensile strengths. The researchers found that 1300 rpm rotation speed, 192 mm/min traverse speed, hexagonal pin shape, 0.08 mm shoulder penetration, and 5° convex shoulder taper were the best process parameters for improving tensile strength in this investigation.

The exploration of FSW welds made of aluminium alloys AA6082-T6 was reported on 5 mm thick plates [46]. A tool of 6 mm pin diameter and a length of 4.8 mm, shoulder diameter of 19

mm, was used to manufacture joints at rotational speeds of 230, 330, 460, 630, 880, 1230 and 1700 rpm with traverse speeds of 115, 170, 260, 390 and 585 mm/min and dwell time of 20 seconds. According to the researchers, when the traversal speed increases, the mechanical resistance of the samples improves due to reduced heat input and limited softening of the material in that region at constant rotating speed. The authors also mentioned that solid joints were achieved by reducing rotational and traversal rates. In their study, it was determined that non-defective and solid joints were identified at 1700 rpm and 585 mm/min, suggesting a link between traverse speeds and greater rotational speeds. It was concluded that the tensile strength of joints is proportional to traversal speeds.

2.2.3 Parameters for FSW of AA5083 and AA6082

As discussed in Chapter 1, AA5083 and AA6082 are marine grade aluminium alloys. They may be utilised in single structures to generate various connections that would be difficult to achieve otherwise owing to mechanical and metallurgical variations. The next sections cover the study of dissimilar joints of AA5083 and AA6082.

Kumar and Ramana [47] investigated the effects of tool variables on the tensile properties of friction stir welded aluminium 5083 and 6082 alloys in a butt joint configuration using 4 mm plate. The purpose of the study was to investigate the tensile strength using three shoulder diameter tools, tool offsets, and tilt angles at gyrating and traverse speeds of 1000 rpm and 900 mm/min; tool shoulder diameters (16, 18 and 20 mm) with square faces at fixed lengths of 3.4 mm and a top face width of 3 mm and a bottom face width of 5 mm; tool offsets (-2, 0 and 2 mm); and tool tilt angles (0°, 1°, and 2°) were all considered in the study. Tensile, yield and elongation results were monitored. The tensile samples are produced in accordance with ASTM E8M standards. The research began with the creation of a mathematical prototype for forecasting the tensile properties of the joint, which was subsequently validated by the ANOVA test. According to the data, a shoulder diameter of 18 mm, no offset, and a tilt angle of 1° yielded no defects, 210 MPa maximum tensile, 203 MPa yield strength and 12 % elongation. Kumar and Ramana claim that the correct incident of dynamic recrystallisation and grain progression results in a stable state of material flow rate and plastic deformation, which explains why the highest tensile strength was achieved at 0 mm offset. In contrast to tool tilt angle, it was observed that tool offset had no impact on the tensile strength. Furthermore, tensile, yield and elongation are affected by shoulder diameter and tool tilt angle, although tool offset affects only elongation %.

The optimisation and characterisation of dissimilar welding of AA5083 and AA6082 aluminium alloys 6 mm thick plates was reported [48]. The investigation focused on the impact of optimising process parameters with a 5-thread tool, taking into account tool tilt angles (0°, 1° and 2°), tool angular speed (700, 900, 1100 rpm), and transverse speed (70, 90, 110 mm/min). The welded joint efficiency and hardness of the dissimilar alloys tested were superior to equivalent aluminium alloys (5083 and 6082). With the tool rotation set to 700 rpm, travel speed set to 110 mm/min, and tool slope angle set to 2°, the highest tensile test was 217 MPa.

Kasirajan *et al.* [49] investigated the effect of process parameters on joint efficiency by varying tool rotation speed and pin profiles while keeping transverse speed, tilt angle and axial force constant in the processing of 6 mm thick aluminium alloys 5083 H111 and 6082 T6. The tool with 20 mm shoulder diameter and pin profiles straight cylinder, taper cylinder and threaded cylinder were used at rotation speeds of 700, 800 and 900 rpm, respectively. To determine a weldment's structural behaviour, the ASTM E3 standards for metallographic and mechanical testing were utilised. Tensile and bend tests were executed according to ASTM: E8 and E190-92. Weldments at tool rotation speed of 800 rpm and 900 rpm produced onion rings in the nugget zone. Dynamic recrystallisation occurred in the nugget zone due to considerable plastic deformation, ensuing in highly refined equiaxed grains according to a microstructure analysis of a 700-rpm weld nugget. The microstructure of the nugget zone exemplifies the heterogeneous mixing process. The results clarified that the cylindricalthreaded tool produced higher tensile strength joints with values at 224 MPa. The micro- hardness at the TMAZ in alloys 5083 and 6082 decreased significantly when compared to that of the weld nugget. Heedless of the varying pin profile, the tensile strength and tool rotation were proportional to each other.

In another study, Kumar *et.al.* [30] observed dissimilar friction stir welding of aluminium alloys (5083-H111 and 6082-T6) on 4 mm thick plates. The authors conducted a comparative study on similar and dissimilar butt joints of AA5083/AA5083 (F55), AA6082/AA6082 (F66) and AA5083/AA6082 (F56) using a taper square tool. The parameters considered in the study comprised traverse speed of 1200 rpm, traverse speed of 63 mm/ min, tool diameter of 18 mm and tilt angle 1°. The study showed that joint F56 demonstrated a higher value of hardness and joint efficiency than the other joint configurations of 56.3 BHN at the nugget zone and 85%, respectively. The authors concluded that dissimilar joints are superior in strength than joints of similar alloys.

2.3 Metallography and fractography analysis of joints

Microstructure and fractography reveal information on imperfections, impurities, granules and grain structure; broken surface properties can aid in determining the kind of failure.

2.3.1 Metallography and fractography analysis of AA5083

This section looks at studies into the metallography and fractography of similar joints of AA5083.

Kumar and Pancholi [50] examined the three-dimensional material flow in course of friction stir welding processing of AA5083 on 6.35 mm thick plates. The study intended to generate knowledge on material course in FSW in a three-dimensional view by planting tracers into the material prior to processing. The tracers were set in three different positions: normal, parallel to the welding direction and parallel to the surface to be treated. The parameters in this study were 1025 rpm rotating speed and 67 mm/min traverse speed at tool tilt angle of 1.5 º using a 25 mm shoulder diameter cylindrical concave tool. The authors noticed a difference in grain sizes (5, 8 and 13 µm) due to varying temperatures at various points of the joint, with the material in close contact with the shoulder having coarser grains than that in the stir zone, which had finer grains due to lower temperatures and increased deformation due to stirring motion. According to the researchers, grain size increases as temperature rises and decreases and as strain rate of recurrence rises. From this work, three movements were identified: the material extrusion and layer reordering from the leading to the trailing sides; twirling of material collected from the advancing side about the tool pin; and finally, the material pushed downward due to the tilt angle.

Similarly Torzewski *et al.* [51] found similar effects of the tool on the material when investigating the microstructure and low cycle fatigue properties of an AA5083 H111 friction stir welded joint of 5 mm thick plates, using traverse and rotational speeds of 100 and 200 mm/min and 500 and 900 rpm, respectively, joined in a butt joint configuration. Microhardness measurements revealed little variation in hardness values. At 0.5, 2.5 and 4.5 mm, measurements were obtained from the upper face, middle and bottom parts of the joint surface. The higher area of the TMAZ had the maximum micro-hardness of 88 HV, while the lower section had the lowest micro-hardness of 85 HV, demonstrating that grain refinement enhances tensile properties in the stir zone. The micro-hardness of the joint rose from 82 HV0.1 to 88 HV0.1 under specified friction stir welding settings due to the dynamic effect of the tool and alterations in the microstructure. The base metal, the

thermo-mechanically affected zone (TMAZ) and the parent metal had modest shifting hardness values. It was found that rotating and traversal speeds of 500 rpm and 200 mm/min produced the highest tensile values, each of which was 98% of the base material. The existence of fatigue markings as well as some fractures was shown by scanning electron microscopy investigations of the fatigue fracture progression zone for all strain amplitudes and classes of materials. The fractures were examined using a scanning electron microscope, which revealed fast breaking and hence a shorter fatigue life.

The effects of the kissing bond on the mechanical properties and fracture behaviour of AA5083-H112 friction stir welds on 6 mm thick butt-welded plates were reported [52]. At varied tool rotational and traverse rates, welds were accomplished with a 20 mm diameter tool with a concentric cylindrical pin with triangular conical right-hand threads: 800, 1000 and 1200 rpm, and 100, 200 and 300 mm/min, respectively, with a 2.5º tool tilt angle. According to the authors, FSW optimality is established by assessing the combined influence of traverse and rotation rates. It was pointed out that, as is widely known, heat input increases with increasing rotational speed and reduces with decreasing traverse speed during FSW. Furthermore, if strength were solely driven by grain magnitude, the grain enormity in the nugget zone of the welds should rise in lockstep with the upsurge in rotational speed to support the surge in hardness, concluded the researchers. With 328 MPa, 178 MPa and 14.5% ultimate tensile strength, yield strength and elongation percentage, scanning electron microscope (SEM) analysis revealed equiaxed dimples of several widths, representative of ductile failure of the material.

Dada [53] considered the fracture mechanics and mechanical behaviour in AA5083-H111 friction stir welds on 2.8 mm thick butt joined plates. This study used a 20 mm diameter cylindrical tool with a 6 mm tool pin with rotational rates of 400, 500 and 600 rpm with traverse speeds of 50, 60 and 70 mm/min and no tool tilt angle. Samples in this study were prepared in accordance with ASTM standard E8/E8M perpendicularly to the joint. According to Dada, there is no apparent relationship between welding parameters and hardness profiles, with better hardness values on the retreating side and worsening hardness values on the advancing side due to frictional heat and grain enlargement, as well as a reaction in frictional heat on the retreating side due to frictional heat. Fragmentation occurred in two directions in tensile samples: diagonally across the TMAZ and HAZ at 45° and then perpendicularly in the nugget's upright orientation. Low vertical force and 0° tool tilt angles, according to Dada, were the major contributors of tunnel faults in the joints in this experiment, likely compensating for force and improved material flow in the downward

direction. Furthermore, on the retreating side, the finer grains and material mixing resulted in a bigger weld zone. The root of the weld, tool marks, tunnel defects, portion of the onion ring structure, and the region of quick fracture were all visible on the fracture surface using the SEM. Poor consolidation resulted from the loss in fluidity and flow of material, culminating in the weld tunnel. The weld root had dimples with large edges indicating a failure by mixed micro-void coalescence and quasi-division fractures initiated by crack initiation by micro-void coalescence and proliferation by tearing of division surfaces forth of the moving crack.

2.3.2 Metallography and fractography analysis of AA6082

This section examines studies of the metallography and fractography of similar joints of AA6082.

The microstructure and properties of 6082 aluminium alloy friction stir welded with different parameters of welding was investigated by Mroczka *et al.* [54], with a 6 mm thick plates at the tool rotating and traverse speeds of 1120 rpm and 1120 mm/min using a 25 mm shoulder diameter tool with an 8 mm pin at 1.5º tool tilt angle. The studies of the mechanical properties were carried out to establish the hardness profiles; measurements were taken at the cross-section at interspaces of 1 mm, 3 mm and 4.5 mm from the surface (face of weld). Vertical analysis shows a similar hardness of the material in the area of the tool pin. The heat- affected zones on both sides of the joint had the lowest hardness. It was observed that the advancing side has a hardness of less than 87-90 HV, whereas the retreating side has a hardness of 95-93 HV. The hardness values in the tool pin area are higher, whereas hardness in the heat affected zone (HAZ) is lower. SEM analysis made evident that across the cross section, one type of ductile fracture can be detected, with locally visible dimples on the particles.

Cavaliere *et al.* [55] studied the influence of welding variables on mechanical and microstructural properties of AA6082 joints processed by friction stir welding on 4 mm thick plates, using a rotational speed of 1600 rpm and traverse speeds (40, 56, 80, 115, 165, 325 and 460 mm/min). The chosen cylindrical threaded tool has a diameter of 14 mm, pin diameter of 6.0 mm and 3.9 mm long. A 3º tool tilt angle was employed for the process. The microstructure of the material appears very fine with equiaxed grains in all the welding conditions. An alteration in grain magnitude and dissemination was distinguished for varying scales of traverse speed; from 40 through to 115 mm/min the microstructure was recrystallised yet not uniform in view of the fact that distinct temperature and strain reached through deformation at reduced rates. SEM images reveal fracture

surfaces filled with very fine dimples, indicating that the material is ductile before failure prior fatigue limit of 80 MPa. Considering the advancing side of the tool the samples region of the samples failed at 100 and 95 MPa. Such enormous flaws are frequently linked to the swirling created in the material on the advancing side, where a more disorganised stream forms, resulting in voids with a mean diameter of hundreds of microns, which characterise the preliminary locate of fatigue fractures. The habitation of dimples on the surface exposed ductile behaviour of the material preceding the fracture. From lesser speeds up to 115 mm/min, the yield strength continuously increases, with the highest yield point value at approximately 185 MPa and elongation at 11.6%.

The parametric optimisation of friction stir welding of Al-Mg-Si alloy: A case study was reported by Khan *et al.* [56] on 5 mm thick plates. H-13 tools with threaded conical pins of 5.5 mm root diameter, 3.5 mm tail diameter, and 4 mm pin length were employed at rotating speeds of 710, 900 and 1120 rpm and traverse rates of 50, 63 and 80 mm/min, with a tool plunging depth of 0.25 mm and a tool tilt angle of 2.5º. The authors summarise: as rotational speeds climbed, the ultimate tensile strength increased as well, and that a further rise in speed enhanced the ultimate tensile strength (UTS) seen between speeds 710 and 900 rpm. Their findings also suggest that when traverse speeds increase, UTS decreases owing to limited heat dispersion. At greater traversal speeds, as explained, heat propagation takes place in a shorter period of time for the same length, lowering overall heat input and consequently grainformation, reducing UTS.

2.3.3 Metallography and fractography analysis of 5083 and 6082

This section reports on studies into the metallography and fractography of similar joints of AA6082.

Kasman *et al.* [57] reported a case study for the welding of dissimilar EN AW 6082 and EN AW 5083 aluminium alloys of 5 mm by friction stir welding. The mechanical and macrostructural properties of dissimilar joints were investigated as a function of tool geometry and the ratio of tool rotating speed to traverse speed, using a 20 mm shoulder diameter triangle and pentagon-profiled tools with a 2º tool tilt angle. Other parameters included tool rotational rates (400, 500, 630 and 800 rpm), traverse speeds (40, 50, 63 and 80 mm/min) and a 20-second dwell duration. Welded joints showed three unique zones, showing that tool rotating and traverse speeds and tool pin profile all impact the zones. According to Kasman *et al*., the FSW parameters and pin profile

significantly impact the geometry of the nugget zone (NZ) and thermo-mechanically affected zone (TMAZ). When compared to a triangular-profiled pin, the visibility of onion rings created by a pentagonal-profiled pin is clearer and the width of NZ is greater. The tool pin profile and settings influence the flow of deformed and lengthened grains in the TMAZ. Moreover, it produced greater ultimate tensile strength values as well as elongation percentages as high as 198.48 MPa and 4.26%, respectively, when compared to the pentagon shaped tool. When employing a triangle profiled tool, the authors discovered that ultimate tensile strength is related to tool gyratory speed and traverse speed while maintaining their ratio constant, as increasing speeds result in increased ultimate tensile strength.

The mechanical, fatigue and microstructural characteristics of friction stir welded 5083-H111 and 6082-T651 aluminium alloys on 6 mm thick plates were studied [58]. The parameters considered in the study include tool shoulder diameter of 20 mm, 2° tool tilt angle, 1250 rpm rotational speed and 64 mm/min transverse speed. Joint designs included similar and dissimilar butt joints AA5083/AA5083 (F55), AA6082/AA6082 (F66) and AA5083/AA6082 (F56). Findings determined that similar and dissimilar alloy junctions showed excellent fatigue limits and tensile strength, indicating that increasing the heat-treating effect results in better joints with fewer flaws when microstructural and mechanical attributes are considered. Onion rings are visible in the nugget zones of various joints in the microstructure; however all joints produce refined grains as a result of recrystallisation. The micro-hardness of AA5083 comparable joints was found to be 80-84 HV greater than that of dissimilar joints. The TMAZ of the AA5083/AA6082 joint was identical to that of similar joints. Weld nugget had an average hardness of 84 HV, whereas TMAZ had an average hardness of 81 HV. In AA5083/AA5083 fracture surface seemed to be inhabited of precisely fine dimples divulging an extremely ductile behaviour of the material in advance of failure, and fatigue patterns were evidently realised in SEM images. AA5083/AA5083 micro-hardness was measured within 80–84 HV with virtually no reduction in micro-hardness values. AA6082/AA6082 micro- hardness was measured between 67–85 HV. The hardness measurements in weld zone were measured at 82 HV, while hardness reduction in thermos-mechanically affected zone (TMAZ) measured 67.9 HV.

Cho *et al.* [59] looked into the evolution of microstructure and mechanical properties during friction stir welding of AA5083 and AA6082 using 15 mm thick plates and 38- and 26-mm shoulder diameter concave tools with a 2º tool tilt angle. Other parameters included tool rotational rates (1200, 1500 and 1800 rpm) and traverse speeds (50, 100, 150, 200, 250 and 300 mm/min).

The intention of this study was to examine the criticality of temperature distribution on the materials. During the process, vigorous recrystallisation was revealed by a fine and equiaxed grain structure in the stir zone. AA5083's stir zone crystallographic orientation exhibited a random distribution, while AA6082's was close to significant shear texturing.

Svensson *et al.* [60] studied the microstructure and mechanical characteristics of friction stir welded aluminium alloys with special reference to AA 5083 and AA 6082. For each material, different thicknesses were used, including 6, 10 and 15 mm for AA5083 and 5- and 10-mm thick plates for AA6082. Welding rates include the following: 92 and 132 mm/min for 6- and 10-mm thick plates; 66 mm/min for a 10 mm thick plate; 46 mm/min for 15 mm thick plates; 530 and 750 mm/min for 5 mm thick plates; and 264 and 374 mm/min for a 10 mm thick plate. Bend testing was done at an angle of 180° over a mandrel of a diameter six times as great as the sample thickness. The presence of microscopic grains in the nugget zone highlighted the distinction between sections that were recrystallised and those that were not throughout the materials' processing, according to the SEM photographs of the researchers. Furthermore, it was reported that grains in the thermomechanical affected zone (TMAZ) showing no evidence of recrystallisation, but having been rotated, and the presence of tiny grains in the nugget zone revealing the differentiation between sections that were recrystallised and those that were not throughout the materials' processing.

2.4 Mechanical and chemical testing of joints

Mechanical testing encompasses a wide range of procedures to determine the mechanical characteristics of material. The section below reviews studies detailing flexural tests and hardness tests of joints.

2.4.1 Mechanical testing of joints

The impact of process parameters on the mechanical characteristics of friction stir welded 5083-O aluminium alloy plates with a thickness of 6.35 mm, using an 18 mm shoulder diameter AISI H13 steel tool with a 6 mm conical tool were examined [61]. The rotational and traverse at speeds of 1100, 1200 and 1300 rpm, at 25, 30 and 35 mm/min, respectively, with shoulder penetrations depths of 0.10, 0.15 and 0.20 mm, at 30 seconds were applied. The American Society for Testing and Materials (ASTM) E8 tensile test and the International Organization for Standardization (ISO) 25239-4 root bending test was performed. Despite their good exterior features,

microstructural examinations found problems in the advancing side of the joints, potentially voids or porosity. The temperature disparities amid the surface in interaction with the tool and the base of the work piece were reduced by irregular stirring, according to the researchers. With bending test samples reaching a bend of 150º, no evident fractures were found. With the lowest micro-hardness of 65 HV and the highest of 85 HV, the yield and ultimate tensile strengths were 145 and 259 MPa, respectively. According to the results, the parameters that produced the fewest defective products were 1100 rpm rotation speed, 30 mm/min traverse speed, and 0.20 mm shoulder penetration.

Babu *et al.* [62] concluded that the mechanical characteristics of friction stir welded 6082 were susceptible to the influences of process parameters. Rotating and traverse speeds in this study – at 460, 630, 880, 1230 and 1700 rpm and 115, 170, 260, 390 and 585 mm/min – revealed that the microstructure of the joints contained refined grains. The results of the tensile tests revealed that sample failure transpired in the heat-affected zone (HAZ) on the advancing sides but passed the 90º bending tests. It was explained that the tensile strength of FSW samples is directly proportional to the speeds (both transverse and rotational) to which they are subjected, concluding that an optimising rotational speed 1230 rpm and traverse speeds of 115 and 170 mm/min can minimise defective joints.

The evaluation of bending strength of friction stir welded AA 6082 aluminium alloy butt joints was reported [63]. The aim was to inspect the bending attributes of friction stir welded AA6082 by differing the employed variables including rotational (1800 and 2400 rpm), traverse (30 and 50 mm/min) and plunging (10 and 20 mm/min) speeds. In this investigation, the bend strength of the FSW AA6082 butt joints was subsequent to processing the 5 mm thick work piece with a taper cylindrical tool pin profile. Their findings show that the samples welded using 50 mm/min and 1600 rpm yielded defective joints while those welded using traverse and rotational speeds of 30 mm/min and 2400 rpm reached adequate temperatures that sufficiently softened the metal to support a higher bending strength. It was observed that with the taper cylindrical tool, a traverse speed of 30 mm/min and a rotating speed of 2400 rpm, the temperature of the parent material softened sufficiently to allow for increased bending strength. The authors state that high bending strength for taper cylindrical tool pin profile can be achieved by using a lower traverse speed of 30 mm/min and a greater rotating speed of 2400 rpm.

Dickerson and Przydatek [64] investigated the fatigue of friction stir welds in aluminium alloys that encompass root defects. AA5083-O and AA5083-H321 with thicknesses of 6 mm and 7 mm, and A6082-T with thicknesses of 6.35 and 6.4 mm were utilised. Welding speeds for AA5083-O are 90 and 140 mm/min; AA5083-H321 is 90 mm/min; and AA6082-T6 is 216 mm/min. For AA5083 materials, a 4:1 bending ratio was used, and for AA6082, a 6:1 bending ratio was used, all of which resulted in no visible cracking at a 180° bending angle. The bending defects that were exposed during bending were investigated using a scanning electron microscope (SEM). According to the researchers, defective surfaces have micro-void convergence characteristics or manifestations, although the depth of the cup and cone voids is smaller than in the area, suggesting either poorer ductility at the flaw face or inadequate bonding. The cup and cone behaviour on the defect face is likewise intermittent, indicating that the material's ductile behaviour on the bond surface grew more defined as the weld progressed away from the root surface. The root defects were only partially bonded, resulting in a mechanical strength that was lower than the surrounding material.

2.4.2 Corrosion of FSW joints

Corrosion tests are used to investigate the degradation of material due to the environment to which they are subjected. Many corrosion test techniques have been devised. The studies below explore the corrosion of friction stir welded joints.

In their study, Saravanakumar *et al.* [65] investigated friction stir welding of AA5083-H32 marine grade aluminium alloy by varying the process parameters on 6 mm thick plates. The aim of the study was to examine the effects of friction stir welding on the microstructure and hardness of AA5083 using circular and threaded profile tools with a shoulder diameter of 15 mm. Rotating speeds of 710, 900, 1220 and 1400 rpm were used, with traverse speeds of 20 and 40 mm/min. For both tools, rotating speeds of 710 and 900 rpm were paired with traverse speeds of 20 mm/min, while 1220 and 1400 rpm were paired with traverse speeds of 40 mm/min. Hardness testing revealed that the circular tool and rotating and traverse speeds of 1220 rpm and 40 mm/min produced higher hardness values of 86.7 HV. Tensile tests were in support of the hardness test results, with a tensile strength value of 205.1 MPa. Using a Plexiglas chamber, samples were immersed in 25 litres of 3.5% NaCl solution. According to the researchers, longer exposure durations increased the area of pitting corrosion.

Gharavi *et al.* [66] studied the corrosion evaluation of friction stir welded lap joints of AA6061-T6 aluminium alloy. The preparation and testing of the immersion corrosion tests were done in accordance with the ASTM G-1-03 and 110-92. The samples were immersed into 3.5% of NaCl solution. The results of the tests showed that subsequent to 48 hours of immersion, the heat affected zone (HAZ) of all the welded samples exhibited susceptibility to intergranular corrosion, as opposed to after 24 hours. On the other hand, the parent material exhibited vulnerability to pitting corrosion and intergranular attack after 24 hours of immersion, and further transgranular attack and pitting corrosion after 48 hours. It was revealed that decreasing the size of the grains in the weld region reduces the corrosion resistance of the materials; processing of materials through FSW affected the joint's corrosionresistance due to the dilapidation of intermetallic particles.

Davoodi *et al.* [67] studied the microstructure and corrosion characterisation of the interfacial region in dissimilar friction stir welded AA5083 to AA7023, with a rotation speed of 1600 rpm, traverse speed of 50 mm/min, and a tool tilt angle of 2º on 7 mm thick plates. A three- electrode electrochemical cell was employed for the electrochemical measurements containing 3.5% NaCl solution exposed to 24 to 26º C using a IVIUM instrument model. According to researcher findings from scanning kelvin probe force microscopy (SKPFM), optic, and scanning electron microscopes, two potential locations for pitting corrosion origination were identified on margins of the two materials and on the AA7023 side.

The effect of processing parameters on strength and corrosion resistance of friction stir- welded AA6082 was reported [68]. The aim of this study was to test the micro-hardness, microstructure and the electromechanical properties of the welded material. The experiment made use of 3 mm thick pieces welded with an 18 mm diameter shoulder with hexagonal thread pin at traverse speeds of 200 and 250 mm/min and rotating speeds 1000 and 1250 rpm and angles 0º and 2º. It was pointed out that the microstructure of FSW products is greatly influenced by operating parameters in particular traverse and rotating speeds as well as tool tilt angle. Electromechanical measurements were executed using 3.5% NaCl solution at a measured temperature of 20º C. It was discovered that tool tilt angles make significant contributions to the improvement of weldment corrosion resistance, as samples produced with tool tilt angle 2º showed an increase in corrosion potential, suggesting that resistance was improved showing less severe dilapidation of material.

2.5 Sampling direction and extraction position

Naumov *et al.* [69] reported on the metallurgical and mechanical characterisation of high- speed friction stir welded AA 6082-T6 aluminium alloy at 2 mm thickness. The purpose of this study was to ascertain if speed has a greater impact on the weld arrangement than it does on the joint's mechanical qualities by utilising low and high-speed friction stir welding parameters. The traverse and rotational rates used in this investigation were 200 and 2500 mm/min, 710 and 2100 rpm, 4 and 6 kN axial forces, and 2 and 1.2º tool tilt angle, respectively. Tensile samples were taken 50 mm from the weld's start and exit point, in the direction of the work piece‘s centre. Results revealed that with lower speeds on the retreating and advancing sides, a decrease of hardness values was observed at 68 HV and 71 HV, respectively. While in the case of high speeds, the comparable values were 77 HV on the retreating side and 69 HV on the advancing side. According to the researchers, higher speeds contribute to increased hardness values of joints and contribute to finer and uniform grains in the nugget. The SEM image of the fracture surface was largely comprised of a great quantity of shallow and homogenous dimples, signifying that the material was mostly ductile. The presence of dimples of various sizes revealed the joint's ductile activity prior to breakage.

In another study looking at the experimental and finite element analysis of progressive failure in friction stir welded AA6061-AA7075 joints on 6.1 mm thick plates. Garg *et al.* [70] adopted several process parameters: 660 rpm rotational speed, 63 mm/min welding speed, and a total plunge depth of 6 mm. Samples were cut longitudinally across the stir zone and transversely to the joint from two sets of welded plates for tensile testing. The researchers reported that the longitudinal tensile samples showed relatively higher ultimate tensile strengths (UTS) because of containing the stirred metal in comparison with transverse samples which house all the varied zones inclusive of the stir zone, heat affected zone, thermo-mechanically affected zone and base metal for samples prepared using both cylindrical and three intermittent flat tools.

The tensile attributes of 6061-T6 friction stir welds and successive modelling in transverse and longitudinal directions on 4.95 mm thick plates was studied [71]. The processing parameters were used as follows: tool rotational speed of 2000 rpm; tool tilt angle 3º; and varied travel speeds of 300, 600 and 900 mm/min. Characterisation of the welded material stress and strain were acquired using longitudinal and transverse samples to the welded joint. Both longitudinal and transverse oriented joint samples showed values of flow stress that were much lower than those of the base

material; equally, the work hardening in the stir region was increased. The longitudinal tensile properties of the joint test pieces welded under like conditions were constantly higher to those in the transverse orientation.

de Giorgi *et al.* [72] examined the outcome of shoulder geometry on residual stress and fatigue properties of AA6082 FSW joints observing the effects of three shoulder geometries (a shoulder with scroll, a shallow cavity and a flat face on 1.5 mm material). The welding parameters used in this study include 1810 rpm rotational speed, 460 mm/min transverse speed, 2° tool tilt angle and 0.1 mm plunge depth. The mechanical characteristics of the joints and the mixed zone were evaluated using transverse and longitudinal tensile assessments at ambient temperature, while fatigue tests were conducted transversally to the joint line.

2.6 Conclusion

A considerable amount of work has been directed at studying the friction stir welding (FSW) process of aluminium and its alloys in consideration of various aspects to it. Very few studies, however, were aimed at the friction stir welding of dissimilar joints AA5083/AA6082 despite their extensive use in industry. Much of the work on these materials is of similar joints which is adequate, as a gap is evident for research of these materials in dissimilar joints.

2.6.1 Parameters

Several researchers have successfully carried out FSW investigations of dissimilar joints AA5083/AA6082, emphasising the need to determine the best parameters for performing and achieving good FSW joints. The following factors have received significant attention: rotational and traverse speeds, dwell time, plunging depth and tool tilt angle.

- It was suggested that appropriate ratios between traverse and rotational speeds be calculated in order to produce high-quality joints.
- It was indicated that the dwell duration, along with speed selection, are key components to consider since these are necessary to guarantee that the material is suitably plasticised prior to the tool traverse motion.
- Plunging depth was taken into account, with many speculating that insufficient plunging of the tool might result in poor joints owing to an unstable vertical force that varies as the material plasticises.

- Tool tilt angle was mentioned as one of the factors that may be used as a supplement in cases when the force fluctuates.

2.6.2 Sampling direction and position

Many friction stir welding researchers have conducted their studies using longitudinal samples. Much of the study has focused on publications looking at traverse samples but these do not specify where the samples were taken from along the length of the joints.

CHAPTER 3

EXPERIMENTAL SETUP & PERFORMANCE

This chapter explains the entire set of friction stir welding, sample processing and sample assessment equipment utilised in this investigation, including descriptions and applications.

3.1 Processing equipment

This section covers a number of mechanical procedures, beginning with material blanking and progressing through welding, sample extraction, metallographic preparation, and ultimately mechanical and chemical testing of samples.

3.1.1 TA Master brand guillotine

A Truecut Mechanical Shearing machine QH11D-3.5 x 1250 guillotine, operated by either hand or foot, was used to cut various materials to the required dimensions. Figure 3.1 depicts a guillotine machine with two blades (upper and lower), the lower blade fixed and the upper blade moving downwards to pare the material. After the cut, the blank or off-cut falls from the rear of the machine or into a receiver located at the rear of the machine.

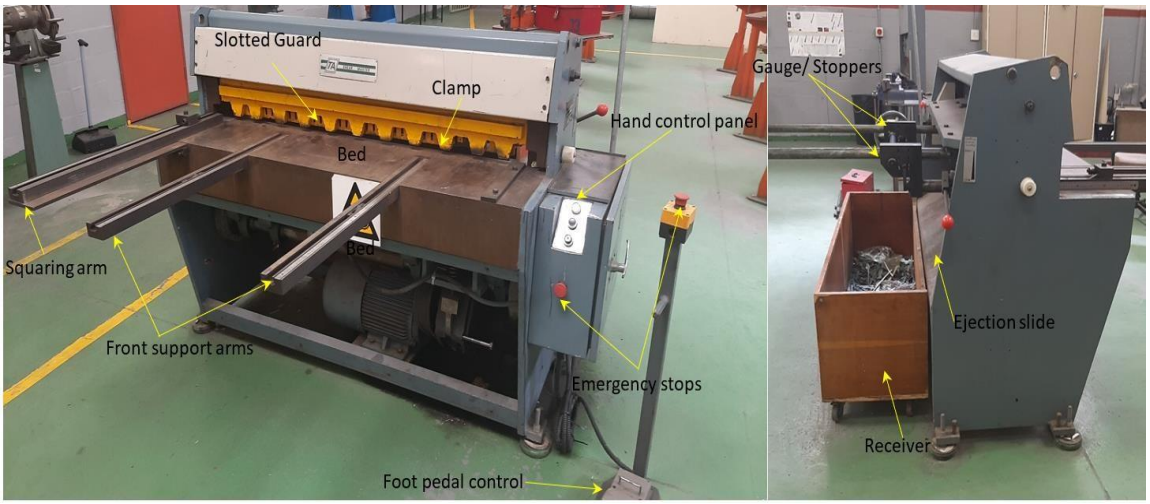

Figure 3.1: Guillotine machine

3.1.2 Belec Compact Port HLC

The Belec Compact Port Hybrid Low Carbon (HLC) was used to determine the material composition of the chosen material (Figure 3.2). This device can determine the amount of each element present in materials. A display monitor, argon cylinder, sparking argon probe and trolley are included with the spectrometer.

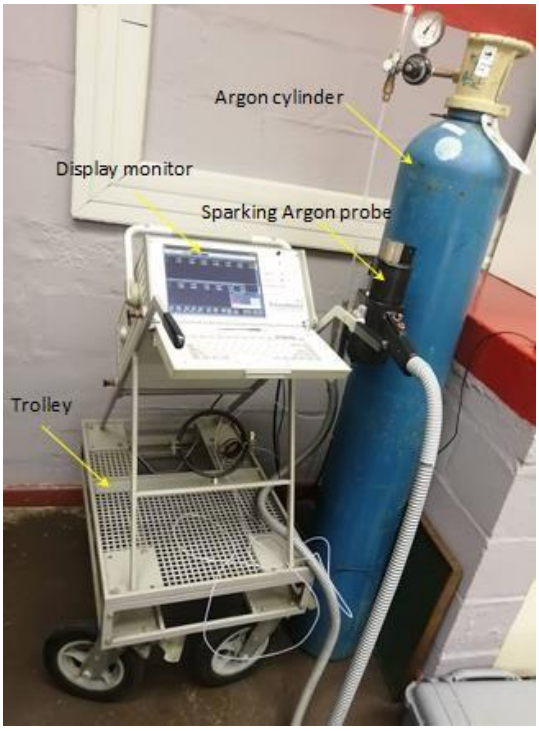

Figure 3.2: Belec spark optical emission spectrometer

3.1.3 Lagun FA. 1-LA conventional vertical milling machine

Friction stir welding was performed on a Lagun FA, 1-LA conventional vertical milling machine (Figure 3.3). The milling machine has a spindle, a table that can move in three directions: X, Y, and Z; cross feed hand wheel; spindle speed selector wheel; power table feed lever; vertical hand crank; and a control panel. This machine offers a 360° head rotation, 0 to 1800 rpm rotating and 0-100 mm/min table traverse speeds.

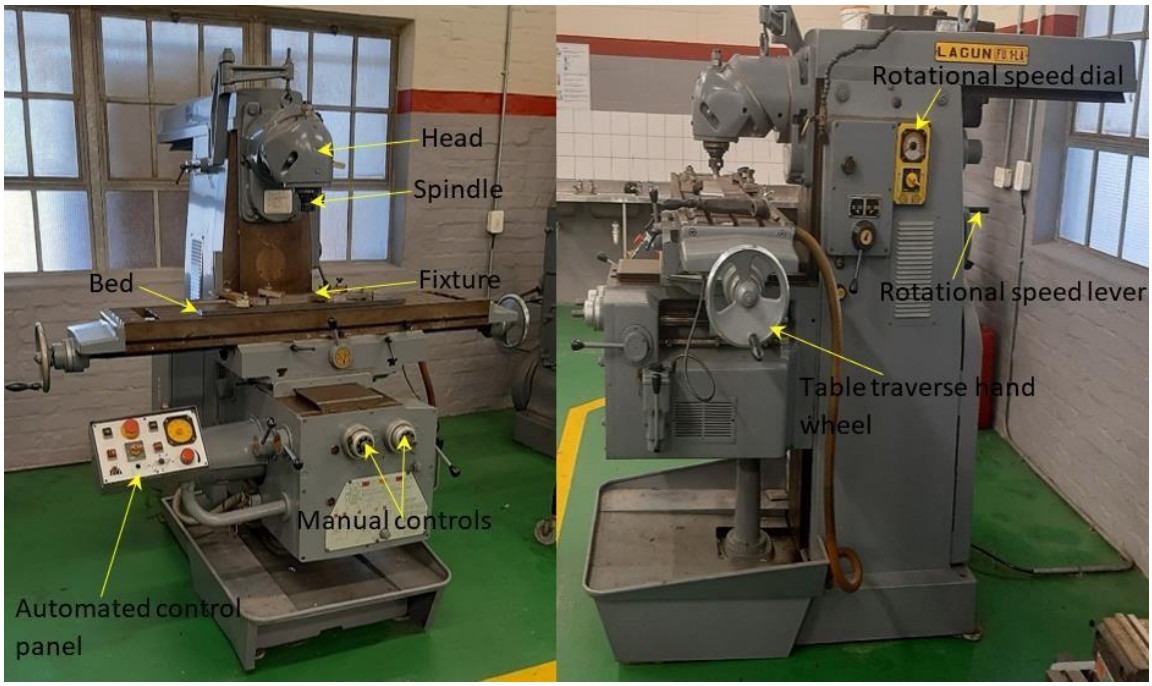

Figure 3.3: Vertical milling machine

3.1.4 Waterjet cutter

This type of industrial equipment can either use pure water or water with abrasives to cut a range of materials of various thicknesses at high pressure into simple or intricate shapes with clean and smooth surfaces, no burrs and no heat. The Mach 3b 7320 waterjet cutting machine is shown in Figure 3.4. The waterjet machine includes a controller, waterjet nozzle, cutting head, X-Y traverse system and cutting table.

Figure 3.4: Waterjet machine

3.1.5 Struers LaboPress-3 mounting press

To mount macro, microstructural, and micro-hardness samples, a Struers LaboPress-3 is required (Figure 3.5). The machine consists of a control panel, a top closure, a mounting unit and a mounting cylinder on which the samples are mounted. The sample is placed on the mounting cylinder, lowered into the mounting unit, hot mounting powder is poured, and the machine's top is closed.

Figure 3.5: Struers LaboPress-3 for mounting of specimens

3.1.6 Struers LaboPol-5 polisher

Metallographic grinding and polishing on three samples (Figure 3.6) may occur simultaneously using an automated Struers LaboPol-5 to eliminate subsurface damage using grinding discs and polishing discs with their corresponding polishing media. The choice of disc and medium is also dependent on the material being worked on. The machine's speed ranges from 50 to 500 rpm and comprises a control panel with start and stop buttons, speed settings, a turn table and a water tap.

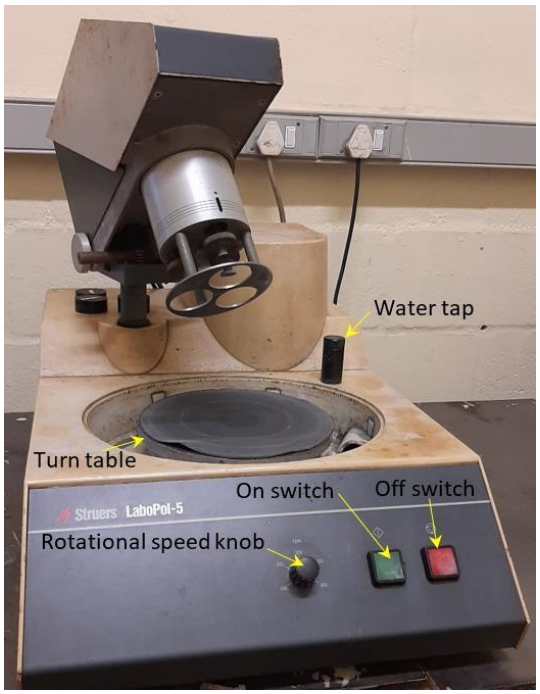

Figure 3.6: Automated Struers LaboPol-5 for polishing of three specimens

3.1.7 Labotec SonicClean ultrasonic cleaner

Labotec SonicClean Ultrasonic cleaner (Figure 3.7) cleaned the mounted samples to remove contaminants from tunnels, cracks and holes. The machine consists of a tank, net basket, a sink, a lid and control panel. Ultrasonic cleaning is accomplished by passing high-frequency sound waves for a set amount of time through the sample while submerged in the solution.

Figure 3.7: Labotec SonicClean Ultrasonic cleaner

3.1.8 Hounsfield Tinius Olsen 50kN

The Hounsfield Tinius Olsen 50kN (Figure 3.9) is a versatile piece of equipment that may be used to test a wide range of materials. Flexural, tensile and compression tests are among of the tests that can be performed on this device. The table, frame, loading cell, moving beam (crosshead), lower and upper fixtures and control panel are several of the Hounsfield components.

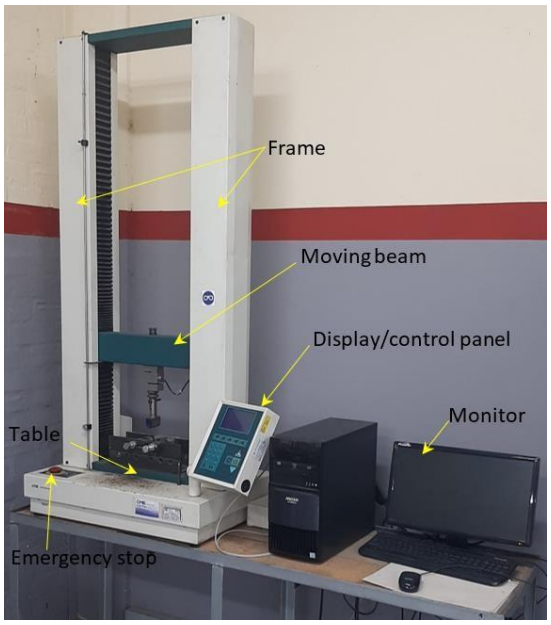

Figure 3.9: Hounsfield Tinius Olsen 50kN

3.1.9 Falcon 500 micro-hardness tester

A hardness testing machine such as the Falcon 500 (Figure 3.10) can perform a variety of hardness tests using several hardness scales: the Vickers (HV), Rockwell (HR), Knoop (HK) and Brinell (HB). The machine includes a turret and optical system, a stage camera, a motorised CNC X-Y stage, and an operator interface (touch screen). The testing method entails using a diamond or hardened steel indenter to make an indentation on a flat ground sample surface under steady load under controlled conditions.

Figure 3.10: Falcon 500 micro-hardness tester

3.1.10 AE2000 inverted microscope

Microscopes are used to examine objects under varied magnification and resolution levels. The AE2000 (Figure 3.11) is an inverted light source microscope. Unlike compound microscopes, the objective of such microscopes is located beneath the stage; therefore the sample will be placed facing down on the stage. The eyepiece, stage, nosepiece, stage adjustment lever, focus knobs, objective and sample clips comprise the parts of the AE 2000 inverted metallurgical microscope.

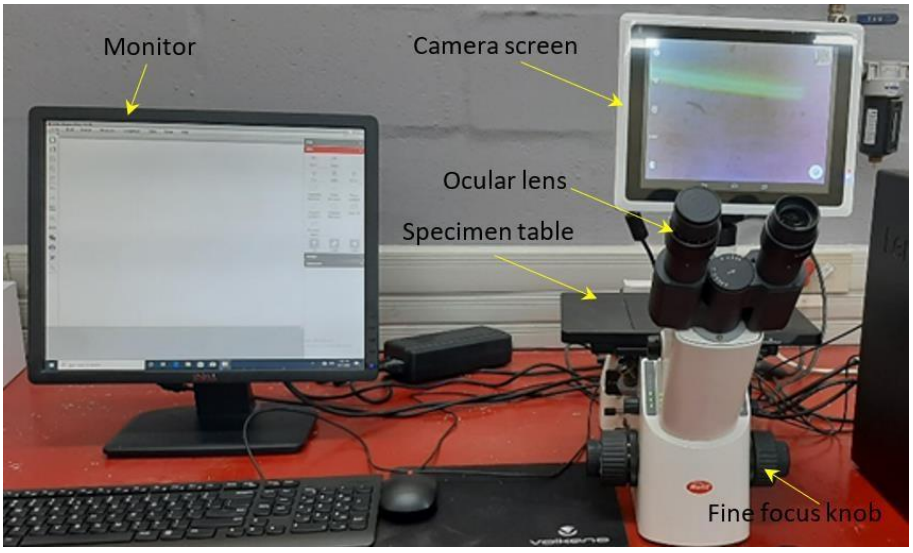

Figure 3.11: Inverted AE2000 metallurgical microscope

3.1.11 Zeiss Stemi DV4 Stereo microscope Binocular 640

Stereo microscopes are for analysing the surfaces of samples up to 10x magnification, giving the viewer a wider and closer view of the material than apparent with the human eye. Figure 3.12 shows the Zeiss Stemi DV4 Stereo microscope Binocular 640. An eye piece, stage, adjustment knob and focus knob are all included with the microscope.

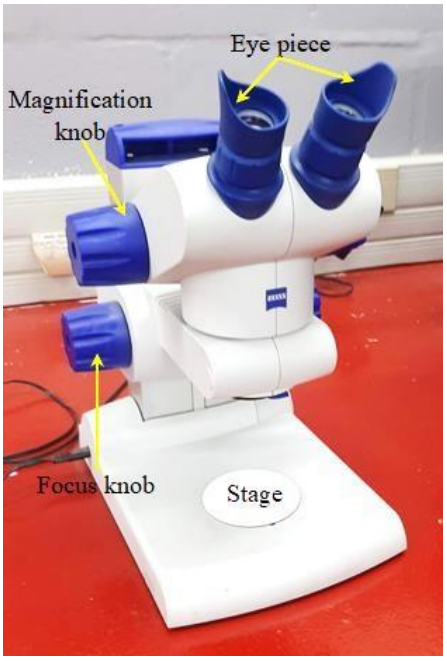

Figure 3.12: Zeiss Stemi DV4 Stereo microscope

3.1.12 Scanning electron microscope

Utilising an electron beam, scanning electron microscopes evaluate the quality of samples. Figure 3.13 shows a Tescan MIRA SEM with an electron chamber and monitors.

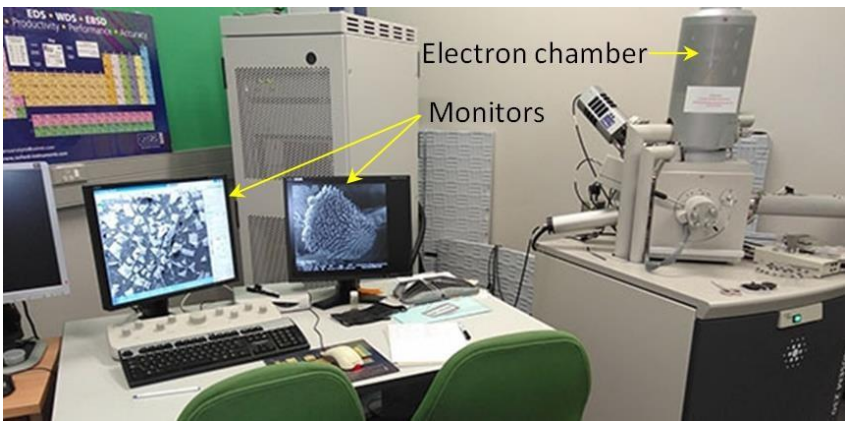

Figure 3.13: Tescan MIRA SEM [73]

3.2 Material processing

The following section discusses the preparations and steps for blanking and welding. This section includes the process from blanking of the stock, friction stir welding application and metallographic sample preparations.

3.2.1 Blanking

The dimensions of the required blanks were marked on the 6 mm thick raw stock of materials AA5083 (460 × 70 mm) and AA6082 (510 × 70 mm). Before cutting, the stock was placed on the guillotine bed with markings aligned with the shearing line (edge of top blade), which was checked by looking through the hole on top of the guillotine. Once a cut was completed, the off-cuts from the stock fell into the machine's reception box at the back of the machine. To remove any oil or other contamination, the blanks were wiped clean on both sides using a paper towel.

3.2.2 Friction stir welding

The blanks were positioned on the fixture as shown in Figure 3.14. The blanks were firmly held in place on the device with six clamps and nuts to prevent them from shifting during the welding operation. After the table was set up, the spinning high carbon steel tool was plunged into the weld line generated by the material's butting edges.

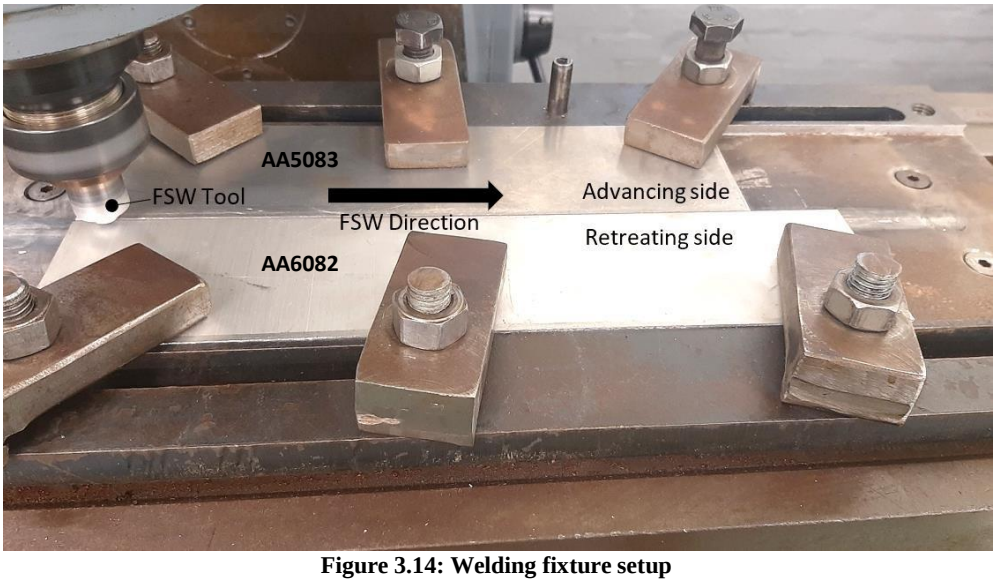

Figure 3.14: Welding fixture setup

The square threaded pin-tipped tool (Figure 3.15) was plunged into the material until its shoulder made contact. The tool was allowed to dwell in contact with the material to create adequate heat to facilitate plasticisation while the pin stirred the mixture. While this was taking place, the tool was permitted to continue traversing along the joint line, forming a solid joint behind it. As the table was lowered at the completion of the weld, an exit hole in front of the tool from the pin was left on the work piece. Table 3.1 presents the welding setup parameters.

Figure 3.15: FSW tool

Table 3.1: Friction stir welding parameters

Parameters and variables	Value/ profile
Tool shoulder dimension	20 mm
Tool pin dimension	6 mm
Tool pin type	Threaded square
Tool tilt angle	1˚
Dwell time	20 seconds
Rotational speed	900 rpm
Traverse speed	60 mm/min

3.3 Sample extraction

This section delves into the extraction method used for the samples. It is worth noting that all sample designs were created with SOLIDWORKS 2018 software, and all samples were extracted with a water jet machine, as in Figure 3.16 (a-c), Figure 3.17 (a-b), Figure 3.18 (a- b) and Figure 3.19 (a-b). Furthermore, samples were taken at three points along the work piece: the beginning, middle and end, as well as in two directions: perpendicular and parallel to the welded connection.

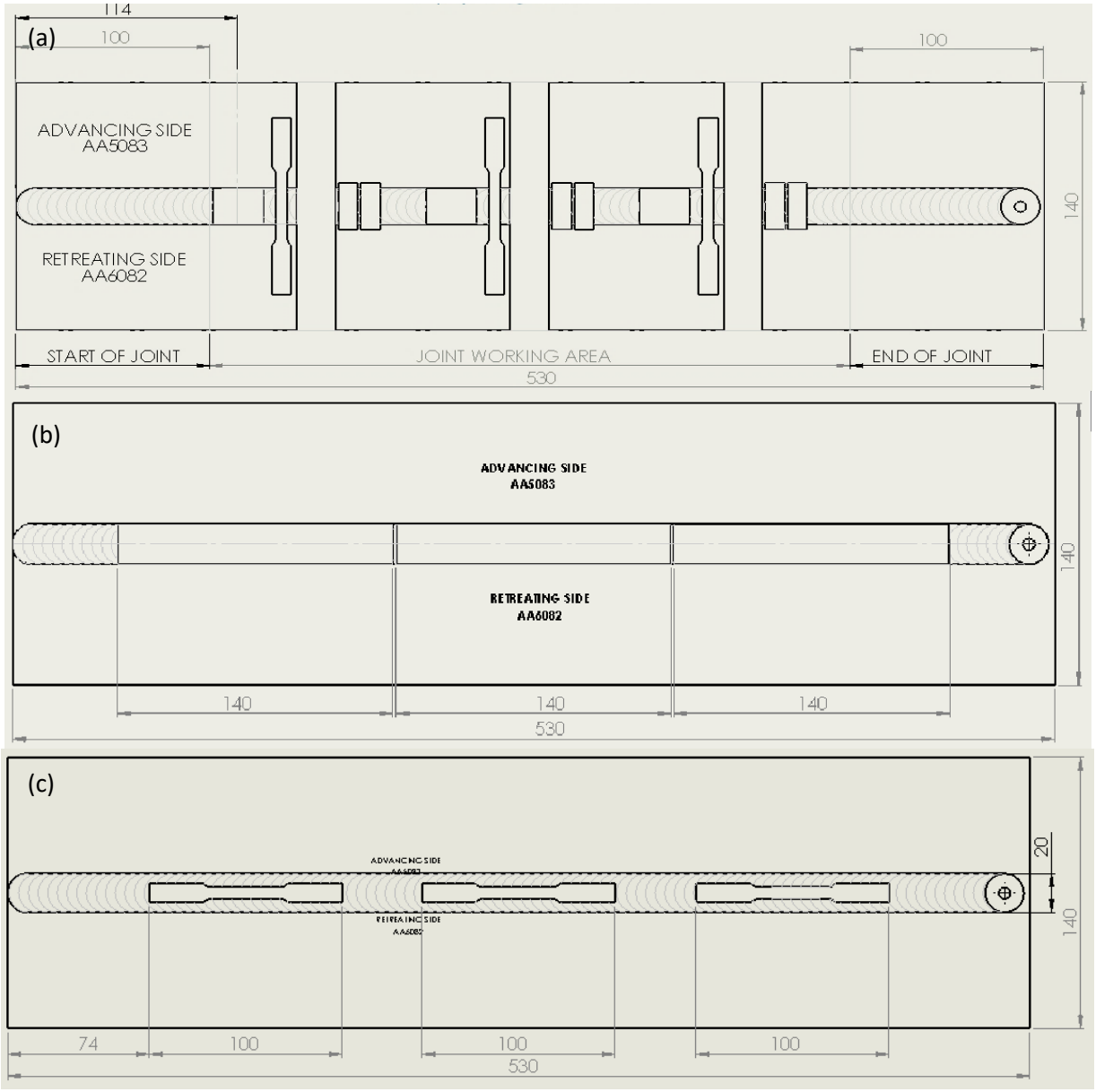

Figure 3.16: Extraction pattern (a) traverse samples, (b) longitudinal flexural, (c) tensile and micro-hardness/structure

3.3.1 Macro/microstructural and micro-hardness samples

Figure 3.17 is a depiction of the macro/microstructure and micro-hardness samples prepared in line with the ASTM-E112-12 and ASTM- E384-11 standards respectively.

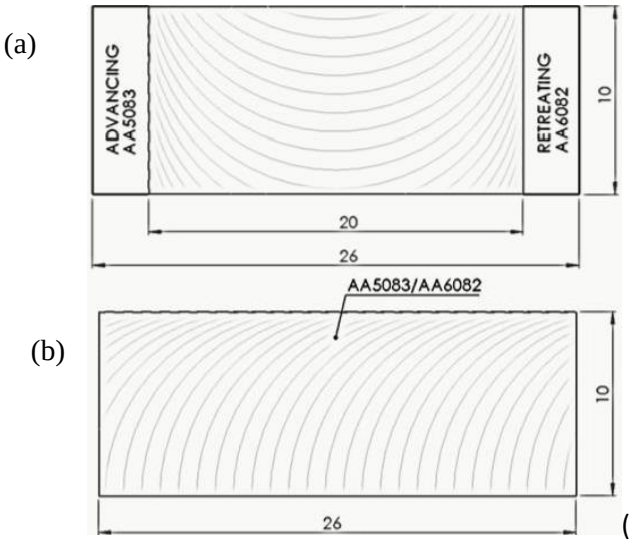

Figure 3.17: Macro/microstructure and micro-hardness samples (a) traverse and (b) longitudinal

3.3.2 Tensile test samples

Figure 3.18 shows a drawing of the tensile test samples which were prepared in accordancewith the ASTM-E8M-04.

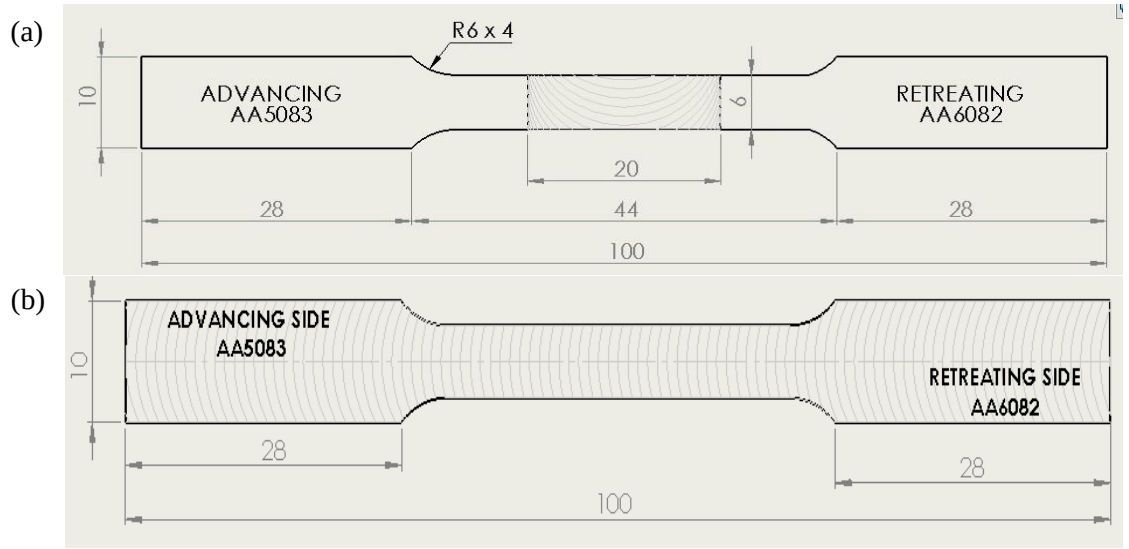

Figure 3.18: Tensile test samples (a) traverse and (b) longitudinal

3.3.3 Flexural test samples

Figure 3.19 shows a drawing of the flexural test samples which were prepared in accordance with the ASTM E290.

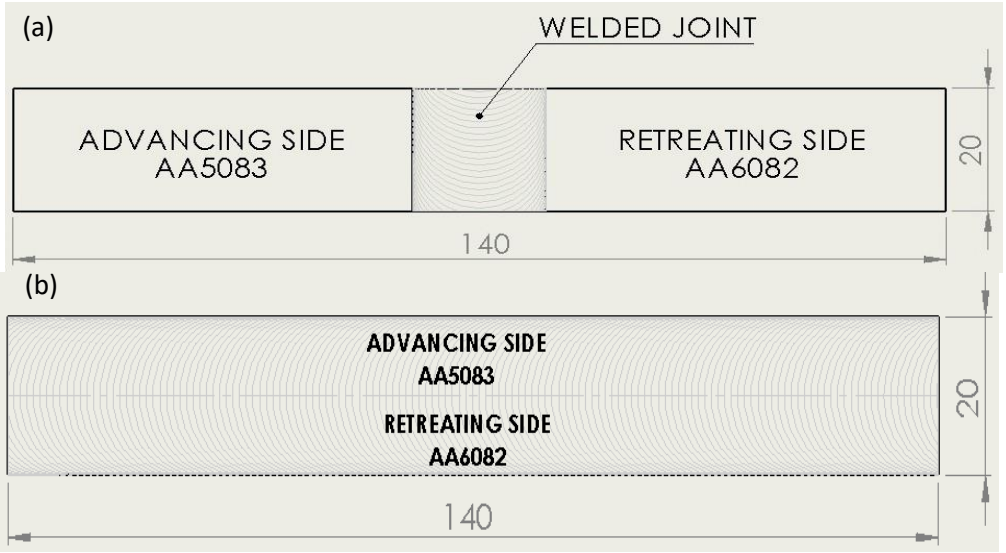

Figure 3.19: Flexural test samples (a) traverse and (b) longitudinal

3.4 Metallographic sample preparations

This section discusses the metallographic preparations of the samples.

3.4.1 Mounting and engraving of macro/microstructural and micro-hardness samples

In order to mount the sample, the Struers LaboPress-3 was turned on and the ram was lifted to place the sample. The ram was then lowered to the desired depth, measured using a Vernier caliper. The cylinder cap was sealed after carefully pouring in Bakelite black hot mounting powder. The mounting procedure was set up, including the force, heating and cooling times, and heating temperature, and then the start button was pressed to start the operation.

3.4.2 Grinding and polishing

The grinding and polishing process of the macro/microstructural samples was conducted on the Struers LaboPol-5. The process was started by mounting the required disc on to the turntable. Once secure, the start button was pressed. Table 3.2 shows the discs and the mediums used for

each the polishing steps. The final step included rinsing the sample with ethanol and then drying. The procedure used in this study was adopted from the AKASEL Aka-Brief #4 Aluminium Alloys. Figure 3.20 shows the mediums for polishing.

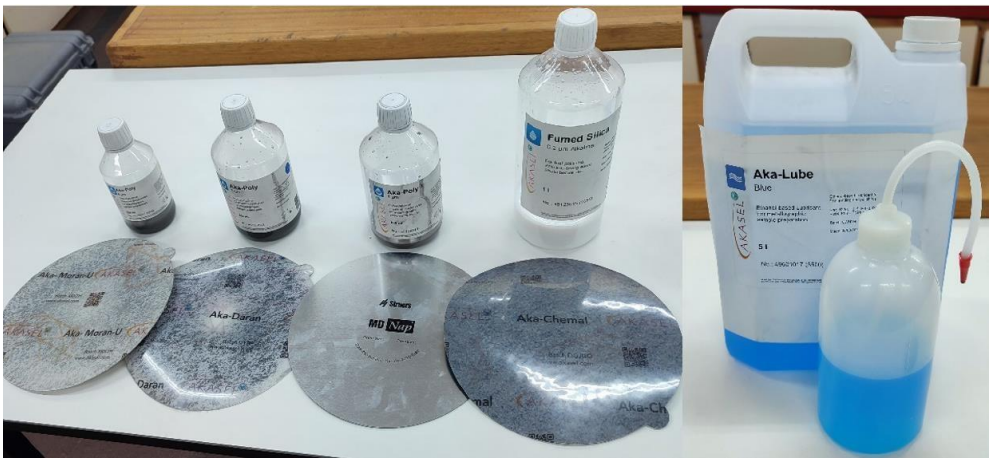

Figure 3.20: Discs and mediums

Table 3.2 Discs for grinding and polishing and the polishing mediums

Disc grade	Medium	Speed
P230	Distil water	300 rpm
P1200	Distil water	300 rpm
Aka- Moran	Aka- Poly 6 µm	150 rpm
Aka- Daran	Aka- Poly 3 µm	150 rpm
Aka- Napal	Aka- Poly 1 µm	150 rpm
Aka- Napal	Fumed Silica 0.2 µm Alkaline	150 rpm
Aka- Chemal	Aka- Lube	150 rpm

3.4.3 Etching

It should be emphasised that with the exception of etching, the macro/microstructure and micro-hardness samples were created in a similar manner. The purpose of this activity is to apply a strong acidic agent to invasively delineate the structure of material surfaces. In this research, two etching chemicals were used: Weck's and Pre-etch Sodium Hydroxide (Figure 3.21). Tables 3.3 and 3.4 include the pre-etch sodium and Weck's agent mixtures, respectively.

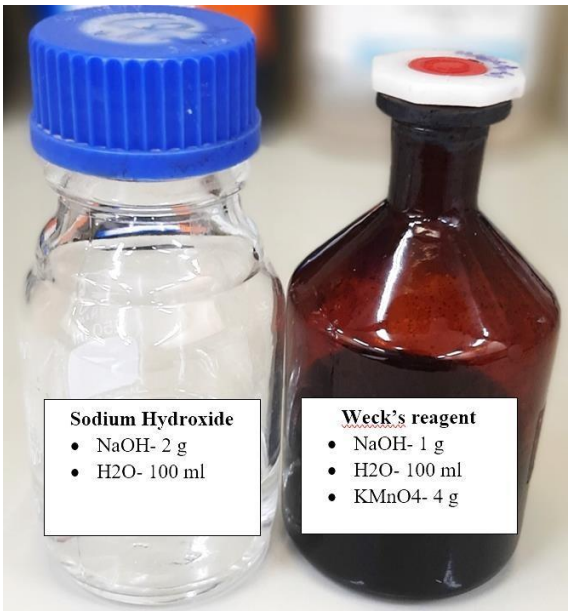

Figure 3.21: Sodium hydroxide and Weck's reagent etchants

Table 3.3: Pre-etch sodium hydroxide acid

Solution	Quantity
Sodium hydroxide (NaOH)	2 g
Distilled water (H_2O)	100 ml

Table 3.4: Weck's reagent

Solution	Quantity
Sodium hydroxide (NaOH)	1 g
Potassium Permanganate ($KMnO_4$)	4 g
Distilled water (H2O)	100 ml

The method used to etch samples from the joint's cross section entailed applying two etchants, one after the other, utilising a tap out method, as illustrated in Figure 3.22.

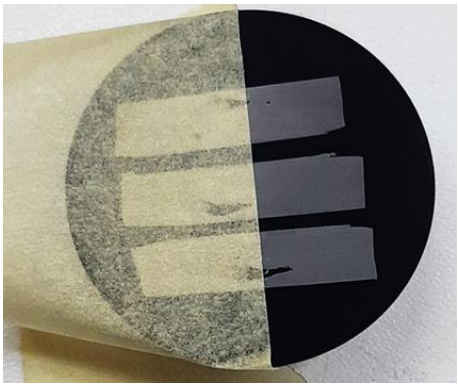

Figure 3.22: Tapped sample

The AA6082 parent and weld zone were exposed to sodium hydroxide for six seconds by covering the AA5083 parent with masking tape. The tape was then removed, and the entire sample was treated with Weck's agent for six minutes. The same agents were employed for longitudinal sampling, but the technique altered since there were thin layers of AA5083 and AA6082 and sealing them out was challenging. As a consequence, less time was spent on sodium hydroxide pre-etching to reduce AA6082 over-etching during the application of Weck‘s. After two seconds of sodium hydroxide, Weck's was given for five minutes.

3.5 Material and sample testing and analysis

The following section summarises the steps taken in numerous tests and analyses carried out in this study, including chemical analysis, mechanical testing, and sample metallographic and fractographic examination. All results from the tests will be discussed in the subsequent chapter.

3.5.1 Chemical analysis

The chemical composition analysis of the material was determined using the Belec compact spectrometer HLC as previously mentioned. Prior setups included placing the sample on the working table, opening argon cylinder, powering the machine, engaging the spark button which also powered the monitor. Once the monitor was on, the Belec WIN 21 software was started, the aluminium test option was selected and the correct description of the material wasinserted.

The process was carried out by placing the Belec probes face down on the sample and applying adequate pressure. A spark emerged at the point of contact after the probe start button was pushed. The probe was left to sit while measurements were taken, after which a yellow flash light indicated completion and a table of results appeared on the monitor.

3.5.2 Mechanical testing

Tensile and flexural tests were performed on the Hounsfield Tinius Olsen 50kN, while hardness tests were performed on the Falcon 500. For the experiments on the Hounsfield, two fittings were used, one for each best suited for those tests. Tensile testing was carried out using flat clamping jaws, while flexural tests were carried out with a three-point bending fixture.

3.5.2.1 Tensile testing

The purpose of the tensile test was to evaluate the ultimate tensile strength (UTS), yield strength (YS), elongation percentage and strain. Prior to mounting of the samples, the samples were measured mainly to verify the thickness and gauge length; these were recorded for the purpose of finding the stress and strain measurements. The tensile sample with a dog bone contour were tested one after the other, firmly gripped at each end by the upper and lower jaws of the flat clamping jaw and pulled apart in tensile testing (Figure 3.23). The data of this test, including tensile force (N) and distance (mm), were recorded using Horizon software and underwent further analysis. Table 3.5 presents the tensile test parameters.

The stress of the tensile samples was calculated using the formula below where A represents the area, F is force and σ is the tensile stress:

$$\boldsymbol{\sigma = \frac{F}{A}} \boldsymbol{\ldots(1)}$$

Strain was calculated using the formula below with ΔL as change in length and L_o indicatingthe initial length.

$$\boldsymbol{\varepsilon = \frac{\Delta L}{L_o}} \ldots (2)$$

Finally, the elongation percentage was calculated using the following equation:

$$\boldsymbol{Elongation\ \% = \frac{\Delta L}{L_o} \times 100 \ldots(3)}$$

Table 3.5: Tensile test parameters

Speed (mm/min)	Extension range (mm)	Load range (kN)	Load cell (kN)
1	0-15	0-10	25

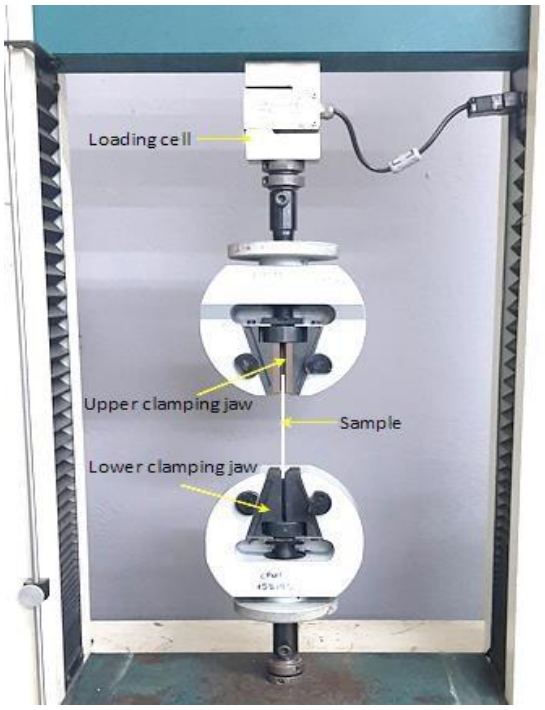

Figure 3.23: Tensile test setup

3.5.2.2 Flexural testing

The Hounsfield universal testing device was used in conjunction with a three-point bending fixture (Figure 3.24) to conduct flexural tests on both longitudinal and traverse samples using the same testing parameters. The initial flexural test entailed measuring each sample and marking the centre of each.

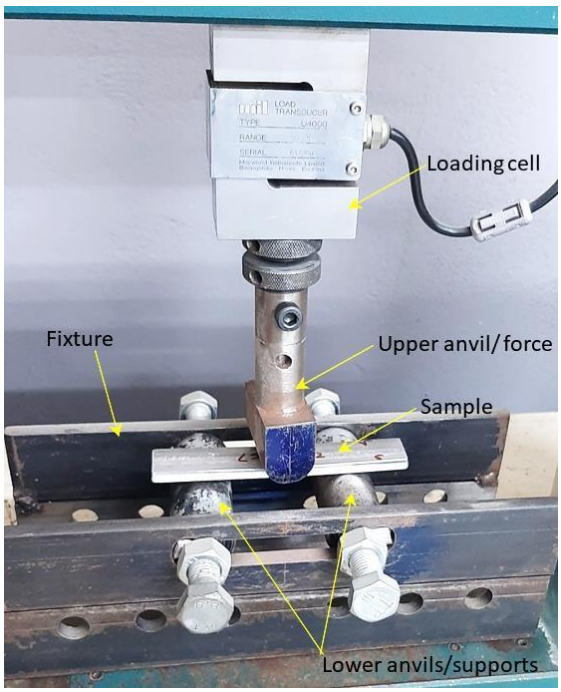

Figure 3.24: Flexural test setup

The samples were put on the roller support one at a time, and the plunger lowered until it came into contact with the sample and was not free to move. The centres were aligned, and the squareness of the sample was confirmed by using an engineering square. Force and extension on the display were set to zero once rigidity was achieved, prior to the start of the test. The testing was carried out by lowering the plunger into the samples until it failed.

The formula used to determine the maximum stress was as follows:

$$\boldsymbol{\sigma} = \frac{\boldsymbol{3Fl}}{\boldsymbol{2bd^2}} \quad \ldots(4)$$

An upper anvil is driven into the sample while it is supported by two lower anvil supports in the three-point flexural bending arrangement. The test is carried out to determine how the material reacts to three main forces – compression, tensile and shear forces – all of which occur simultaneously when the material is bent. The data from these tests, automatically entered into the computer software, enable the generation of graphs from the beginning until the sample failure point.

3.5.2.3 Microhardness test

Both the parent materials and welded samples had their hardness measured using the Vicker's test on an InnovaTest Falcon 500. The tests were undertaken with the Falcon Impressions software. The sample was then placed in the centre of the stage, with the objectives focused on it and the pattern, number of indentations necessary per line, spacing between indents, and distance between lines all established. A 0.2 kg test load was applied for 10 seconds at 1 mm intervals with a 2 mm offset between the lines (Figure 3.25 [a-b]). To test the hardness of the welded joints and parent materials, respectively, welded samples were indented 57 times in three rows, each with 19 indentions, while the parents were indented 34 times in two rows, each with 17 indents, as shown in Figure 3.25 (a-b). The data was recorded; a report was created and savedfor subsequent analysis.

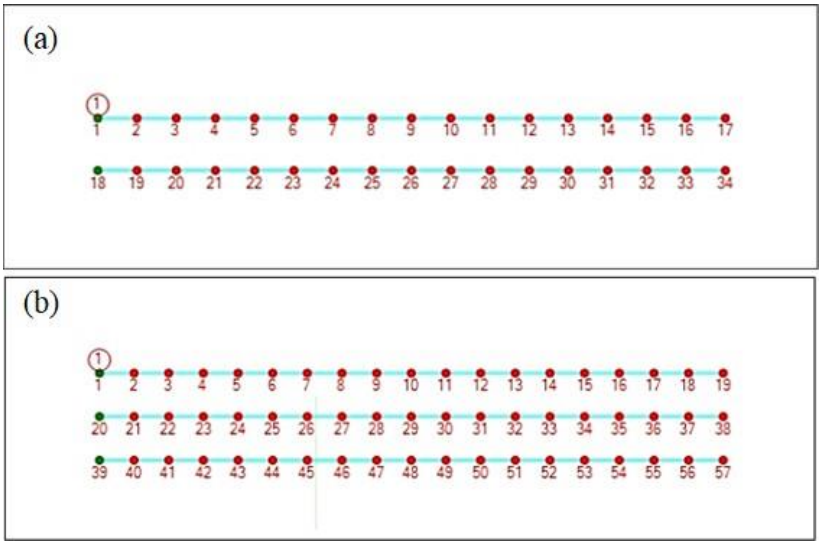

Figure 3.25: Microhardness test pattern (a) parent materials and (b) traverse and longitudinal

3.5.3 Metallographic and fractographic analysis

This section covers the metallographic and fractographic analysis of the FS welded samples.

3.5.3.1 Macro/microstructural analysis

The welded joints were examined macro and microstructurally using the Motic AE 200 microscope and Motic software. The procedure began with the sample being placed on the sample table after opening the Motic programme. The focus was adjusted until it was clear using the adjusting knobs. The software's scale was reset to 100 µm. Magnifications of 5, 10, 20, 50 and 100x were employed to explore different portions of the microstructure, with the highest magnification (100) providing a closer look at the sample and allowing the grains of the parent metals or joints to be seen and measured. The ASTM E112-13 linear intercept method and Image J software captured and saved images for later examination.

3.5.3.2 Scanning Electron Microscope (SEM)

The Tescan MIRA SEM was used to amplify and analyse the topographic characteristics of fractured surfaces of tensile test samples.

CHAPTER 4

RESULTS & DISCUSSIONS

This chapter presents the results and analysis of samples related to the friction stir welded (FSW) AA5083/AA6082 dissimilar joint and its parent materials. Among the characterisation methods used to study the properties of the samples are the visual, mechanical, metallographic and fractographic examinations, which will be further categorised into specific tests and their findings elucidated and deduced for this study. To provide improved material strength of the joint, high strength material AA5083 is applied to the advancing side [74].

4.1 Material chemical composition

Figure 4.1 below depicts the blanks of the material used AA5083-H321 and AA6082-T651 prior to being welded. The Belec compact spectrometer HLC determined the chemical composition of each parent materials. Table 4.1 details the findings for chemical composition, showing that AA5083 had the highest concentration of Magnesium (Mg) followed by Manganese (Mn), and that of AA6082 had the highest content of Silicone (Si), followed by Mg. The primary elements—Mg for AA5083 and Si and Mg for AA6082—all fit within the previously mentioned limitations in the literature [75, 76]. Mg and Si function together to augment the strength of an alloy by enabling precipitation hardening to occur in the heat-treatable alloy and enhance metal wear and corrosion resistance properties without compromising its ductility [75, 77] Manganese may strain-harden intermetallic phases that have finely precipitated or solidified while maintaining ductility and corrosion resistance [78, 79].

Figure 4.1: AA5083 and AA6082 blank materials

Table 4.1 Material chemical composition

	Al	Si	Fe	Cu	Mn	Mg	Cr	Zn	Ti
5083	Balance	0.148	0.163	0.015	0.684	4.022	0.040	0.011	0.017
6082	Balance	1.329	0.679	0.026	0.433	1.209	0.005	0.544	0.042

4.2 Visual inspection of joint

Ensuing the application of FS welding, inspections for surface defects were carried out. The welded work piece was examined on both its face and root to check for potential FS welding defects. The sample's face is the side to which the welding tool was applied, and its root is the side in contact with the jig during the welding application. Surface grooves and flash are defects frequently linked with the use of unsuitable or incompatible welding parameters for applied material in FS welding [80]. A minuscule amount of flash was seen throughout the length of the weld's edges (Figure 4.2[a]), and there was a noticeably larger amount of flash at the weld's start and end locations. Suitable welding parameter combinations including but not limited to speeds (rotational and traverse) and plunging depth, eliminates potential defects such as surface tunneling, flash and cracks from occurring [81-83]. The root inspection revealed no surface defects, as shown in Figure 4.2(b).

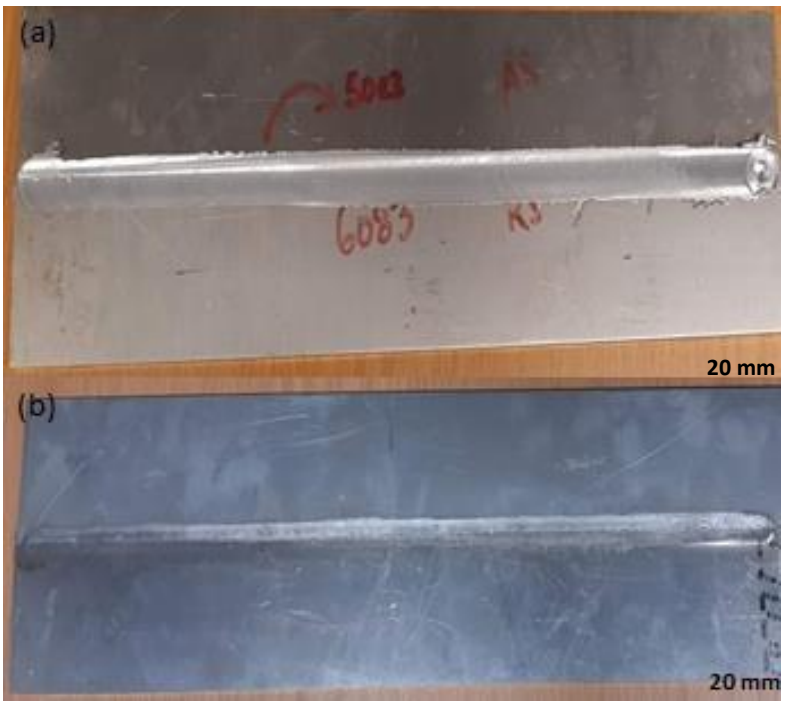

Figure 4.2: Welded blanks (a) face and (b) root

4.3 Metallographic analysis

This section presents the metallographic results obtained using the equipment detailed in Chapter 3.

4.3.1 Macrostructural analysis

The Zeiss Stemi DV4 Stereo microscope Binocular 640 captured the macrostructure images to examine and characterise the sample findings.

4.3.1.1 Macrostructure sample analysis: traverse

Figure 4.3(a) displays mounted traverse samples from the start, middle and end (SME) locations of the aforementioned FS welded joint. Figures 4.3(b)–(d) show the magnified macrographs of the samples, with AA5083 on the advancing side (left) and AA6082 on the retreating side (right). Micro-voids in the samples have been highlighted with circles, and the arrows have been used to highlight tunnel defects.

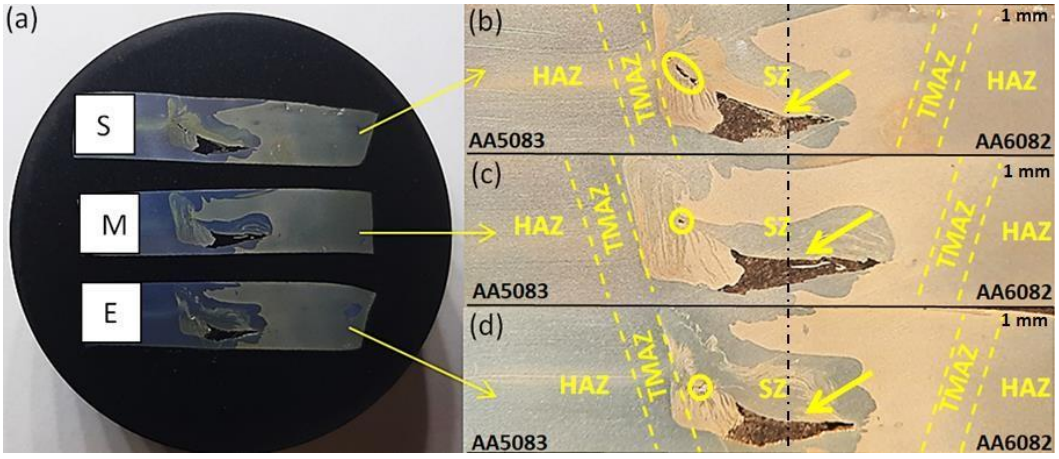

Figure 4.3: Traverse macrostructure (a) mounted samples (b) start, (c) middle and (d) end

Through sample examination, it was possible to identify the four primary FS welded joint zones the parent material zone (PM); heat affected zone (HAZ); thermo-mechanically affected zone (TMAZ); and stir zone (SZ) from the SME samples. The HAZ, TMAZ and SZ are the only areas displayed based on the micrographs (Figure 4.3 [b]–[d]) [84]. The HAZ and TMAZ are both discernible on both the retreating and advancing sides of the samples, and there is no evident onion ring due to the underdeveloped SZ caused by tunneling. As evidenced by the

bands and quantity of AA6082 on the samples' advancing side, and both materials having passed the butt line, there was some evidence of material plasticisation and interflow. The micro-void and tunnel defects were noted among the often-found FS weld defects [85-86]. A frequent spot on the advancing side, where much of the material interflow appears to have happened, is where the micro-voids (encircled in Figures 4.3[b]-[d]) are apparent. It was also observed that the micro-void appeared smaller with each sample from the SME. As previously mentioned, all three samples had visible tunnel defects discovered close to the bottom of each sample. These defects appeared to gradually get smaller as they approached the retreating side of the samples. Due to the different chemical and mechanical characteristics, such defects are more frequent, especially at joints where the materials have varying melting points [85-88]. According to recent research, hot or cold welding of the materials can also contribute to the presence of macrostructural defects due to poor welding parameter combinations which impede material swirling and mixing [89].

4.3.1.2 Macrostructure sample analysis: longitudinal

Figure 4.4 (a), (d) and (g) show the longitudinal samples that were acquired from various locations: the start, middle and end of the weld. The samples placed at the top section of the mount are from the advancing side, whilst those mounted at the bottom are from the retreating side. Figures 4.4 (b), (e) and (h) display the AA5083 advancing section (AS) macrographs, whereas Figures 4.4 (c), (f) and (i) display the AA6082 retreating section (RS) macrographs of the longitudinal samples. The tunnel defects have been indicated, together with yellow marks encircling micro-voids in (Figures 4.4 [b], [c], [e], [f], [h] and [i]) and crack in Figures 4.4 (e). The materials may be easily differentiated by their contrasting tones; AA5083 material appears grey whereas AA6082 has two shades of cream, one of which is virtually beige in appearance. The AA6082's different tones may have resulted from the material's various levels of contact and reaction with the etchant [90-91].

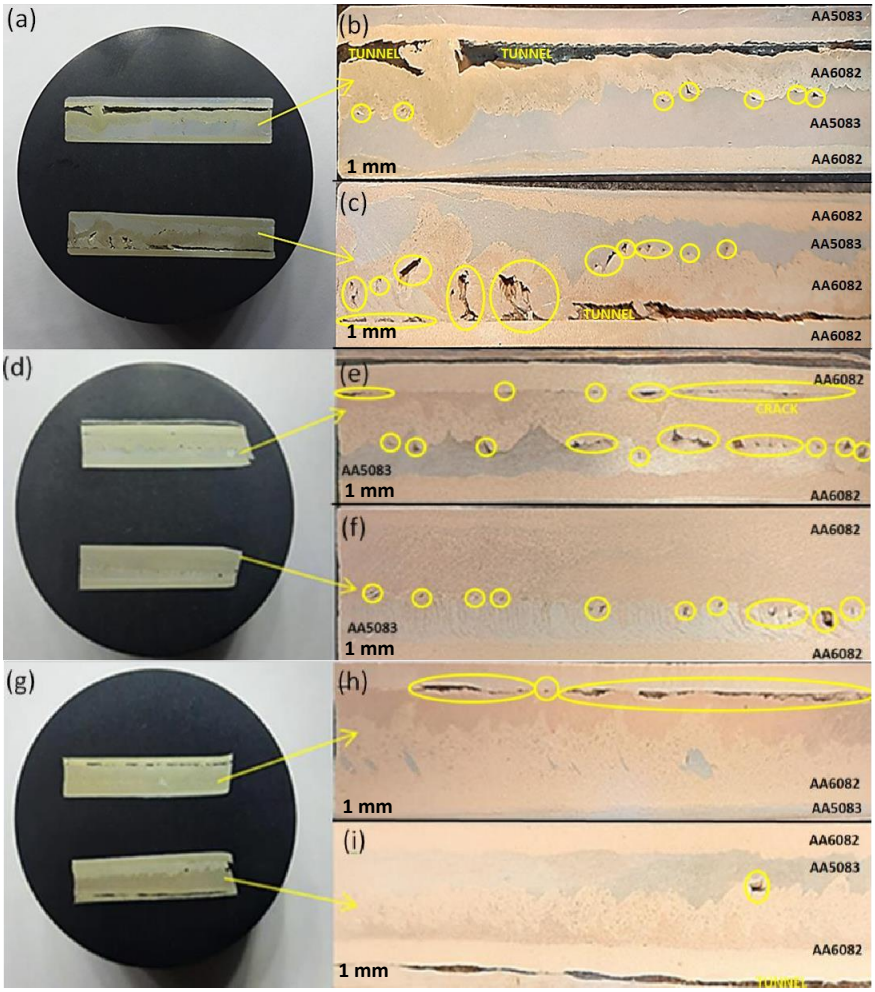

Figure 4.4: Longitudinal samples: (a) mounted start samples, (b) start AA5083 section, (c) start AA6082 section; (d) mounted middle samples, (e) middle AA5083 section, (f) middle AA6082 section; (g) mounted end samples, (h) end AA5083 section and (i) end AA6082 section

Each of the samples presented in the macrographs has materials that are intermittently layered, as shown in the longitudinal samples (Figures 4.4 [b], [c], [e], [f], [h] and [i]). This morphology, the consequence of the material interflow, is consistent with what was depicted in the macrograph images in Figures 4.3 (b-d). The samples were determined to have different amounts of each material, with some samples bearing more AA6082 than AA5083 and exhibiting micro- and tunnel-sized voids. Figures 4.4 (b), (c), (h) and (i) show that the start and end samples, respectively, have large and medium-sized tunnel flaws running along their lengths. As seen in Figure 4.4 (e), the middle sample showed distinct outcomes, with the tunnels appearing narrower and appearing as cracks or nearly fading more than those on other samples (Figure 4.4 [c]). In addition to the tunnel defects on the samples, all of the samples had micro-voids of various sizes. The majority of the voids formed at the material interface. Figures 4.4 (b) and 4.4 (c) illustrate that a squiggle pattern was primarily seen on start samples from both the advancing and retreating sections on the far-left end. This material flow pattern could have been

caused by stirring and the heat's failure to reduce the high material viscosity during the dwell period. On the middle sample's retreating section, another flow pattern was seen. Figure 4.4 (f) shows the presence of diagonal bands that are virtually identical to those on the advancing side of the traverse samples. The presence of these bands suggests plastic deformation and material interflow, with AA6082 material sloughing into AA5083 material caused during the stirring of the materials [92]. As was already indicated, the existence of tunnel and micro-void defects, which were also identified, result from insufficient heating, which impedes the material from reaching adequate viscositybefore the tool traverses [93].

4.3.2 Microstructure analysis

This section discusses the microstructural arrangement of the FS welded joint AA5083/AA6082. The AE2000 inverted microscope was used to conduct the analysis and characterise the microstructure of the samples, respectively. The Origin 2018 programme was used to obtain the mean grain and standard deviation values. Figures 4.5 (a) and (b) depict the micrographic images of the PMs AA5083 and AA6082, respectively. Figure 4.5 (a) depicts the cuboidal and columnar-shaped grains that define AA5083, whereas Figure 4.5 (b) depicts the flat, elongated grains that distinguish AA6082. The SZ of the samples will be the main focus in this section as the longitudinal samples only include the SZ.

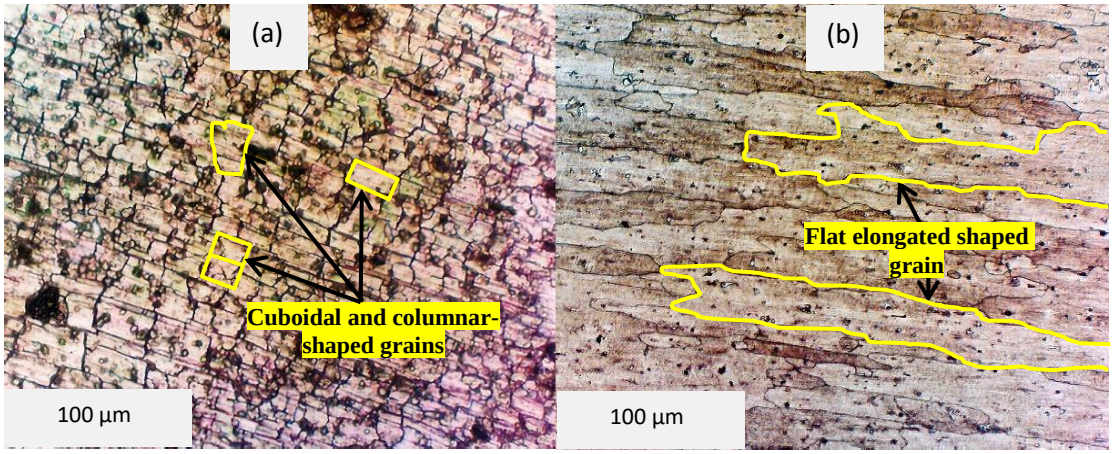

Figure 4.5: Microstructure of selected materials (a) AA5083 and (b) AA6082

4.3.2.1 Microstructure analysis: traverse

The SZ micrographs of the traverse samples from the aforementioned joints are shown in Figures 4.6 (a)–(c) from the SME locations. The micrographs of the start samples are shown in Figure 4.6

(a), those of the middle sample are shown in Figure 4.6 (b), and those of the end sample are shown in Figure 4.6 (c). The two materials may be clearly differentiated from one another wherein the AA6082 material was found to imitate shattered glass (Figure 4.6 [a]-[c]) whereas the AA5083 material had no distinct grains evident and appeared as a band of material (Figure 4.6 [c]). In comparison to the grains found in the parent materials but not equally distributed, fine grains were found in all the samples from the joint. When compared to the PMs and the start and middle samples, it was discovered that much of the region of the end sample had finer grains. Due to the presence of the tiny grains, it is evident that tremendous strain and increased temperatures were attained in the procedure, resulting in dynamic recrystallisation [94]. The grain sizes of each sample from the SME location showed various sized grains owing to grain refining, as seen in the micrographs (Figure 4.6 [a]-[c]). Greater temperature and strain were likely attained at the joint's end than at its start or middle location owing to the presence of finer grains (see Figure 4.6 [c]).The grain measurement results indicate a fluctuation from the varied locations. The traverse start sample measured a mean grain size of 10.328 µm with SD of 3.934 µm; the middle sample measured a mean grain size of 11.884 µm with an SD of 4.491 µm; and finally, the end sample measured 7.618 µm with an SD of 3.854 µm.

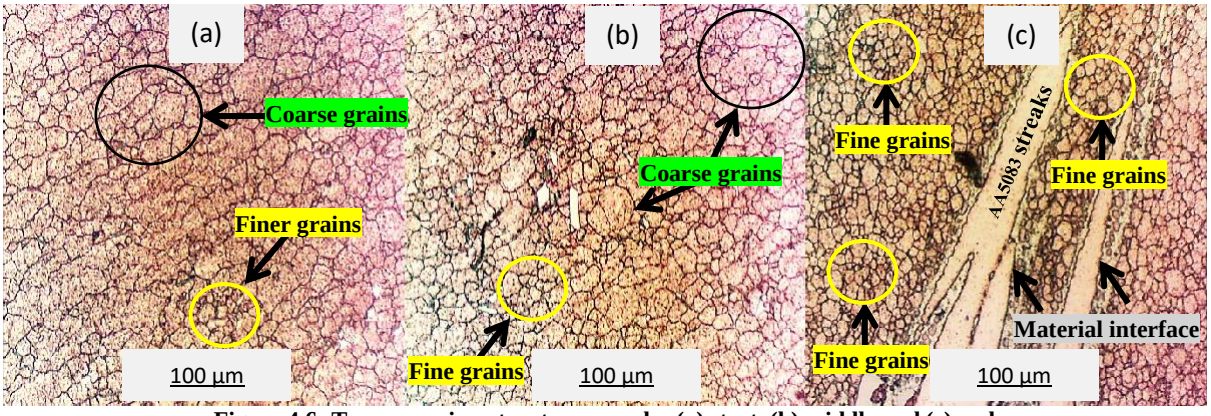

Figure 4.6: Traverse microstructure samples (a) start, (b) middle and (c) end

4.3.2.2 Microstructure analysis: longitudinal

Micrographs of the longitudinal samples from the aforementioned joints are shown in Figures 4.7 (a)–(c) from the SME locations. It should be emphasised that the samples taken longitudinally only contain the material in the SZ. Figure 4.7 (a) displays the start sample, Figure 4.7 (b) displays the middle sample, and Figure 4.7 (c) displays the end sample. The materials can be easily distinguished from one another. The results of the longitudinal samples were similar. AA6082 appeared identical in both the traverse and longitudinal samples, having undergone dynamic

recrystallisation with an appearance of shattered glass. AA5083, however, presented varying features. AA5083 appeared quite dense, indicating that it had undergone grain boundary migration spurred on by abnormal grain filling [95] (Figure 4.7 [a]). Additionally, a line that was not quite solid but still discernible was seen apportioning the materials. This dark line (interfacial layer), observed separating the materials from each other, and is due to intermetallic compounds [96]. Interface boundaries exist when the grains on either side of a boundary have dissimilar microstructures, lattice characteristics and/or chemical compositions, as when precipitation or overgrowth takes place [97]. The micrograph of the middle sample, Figure 4.7 (b), likewise shows a similar line enclosing the band of AA5083 material. Additionally, it was noted that the sample had uninform grains, with certain regions showing signs of a restricted strain due to the presence of still-large grains. The end sample, shown in Figure 4.7 (c), may be understood to have endured significant grain deformation given the extremely miniature grain size [98]. The longitudinal start samples measured grain 15.608 µm with SD of 6.839 µm; the middle sample measured a mean of 19.881 µm with an SD of 14.022 µm; and finally, the end sample measured 9.187 µm with an SD of 3.827 µm.

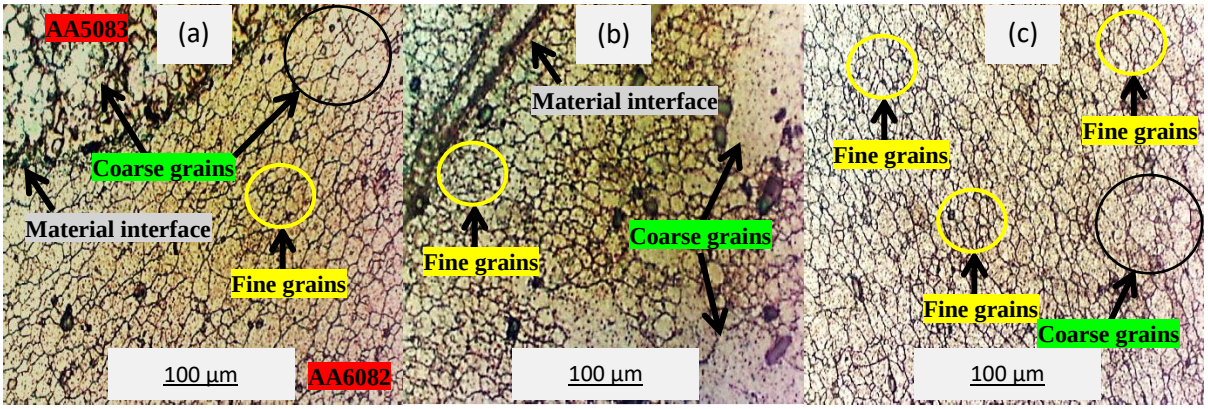

Figure 4.7: Longitudinal micrographs (a) start, (b) middle and (c) end

The results of the micrographs have been organised into a table format for an easier comparison (Table 4.2).

Table 4.2: Microscopic grain analysis results

ID		Mean grain size (µm)	Standard deviation ((µm)
AA5083	Parent	97.385	29.522
AA6082	Parent	130.832	50.066
Traverse	Start	10.328	3.934
Longitudinal	Start	15.608	6.839
Traverse	Middle	11.884	4.491
Longitudinal	Middle	19.881	14.022
Traverse	End	7.618	3.854
Longitudinal	End	9.187	3.827

4.4 Mechanical analysis

The mechanical properties of the AA5083/AA6082 joint are covered in detail in this section. The three primary discussion points in this section will be tensile, flexural and micro-hardness.

4.4.1 Tensile tests

This section presents the tensile behaviour of the samples that were sampled in the longitudinal and traverse directions. A Hounsfield Tinius Olsen 50kN was used to test the samples at a rate of 1mm/min.

4.4.1.1 Tensile tests: traverse samples

The traverse post-tested tensile samples from the SME locations of the AA5083/AA6082 FS welded dissimilar joint are shown in Figure 4.8. It should be noted that in this section, A and R stand for the sample's advancing and retreating sides. The SME samples' failure locations at the SZ were constant in all three samples encircled in Figure 4.8 which are encircled in the image. All of the samples' fracture directions were shown to differ, however. While the middle and end samples' fractures emerged at an angle of around 45º, the start sample's fracture appeared to be more perpendicular through the upper section of the joint and the lower section angled. All samples showed a meandering tear, slight necking and a fracture cup-cone mode.

These modes, recognised as peculiar to plastic deformation seen in ductile materials under tensile stress, are possibly a result of insufficient bonding between materials [99-101].

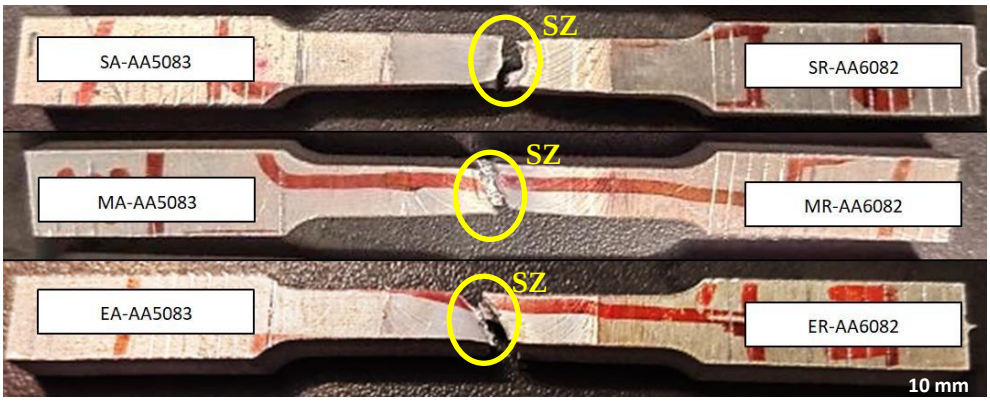

Figure 4.8: Post-test traverse tensile test samples

The samples' failure at the SZ could have been attributed to the presence of defects, specifically tunnels and micro-voids that increase the localised stress where they are [85]. There is a correlation between the position of the flow-induced defect and the location of the fracture as shown in Figure 4.8. The flow-induced defect serves as a site of stress concentration for crack development and propagation [81]. It has been reported in the literature that samples are most likely to fail at the HAZ for 5XXX and the TMAZ for 6XXX in dissimilar joints [102-104]. In general, the failure of a sample is dependent on its quality; thus, failure may occur at either of the zones identified in FS welding, including HAZ, TMAZ, BM and SZ [105-107]. Figure 4.9 graphically presents the tensile test results of the PMs and samples in the traverse direction.

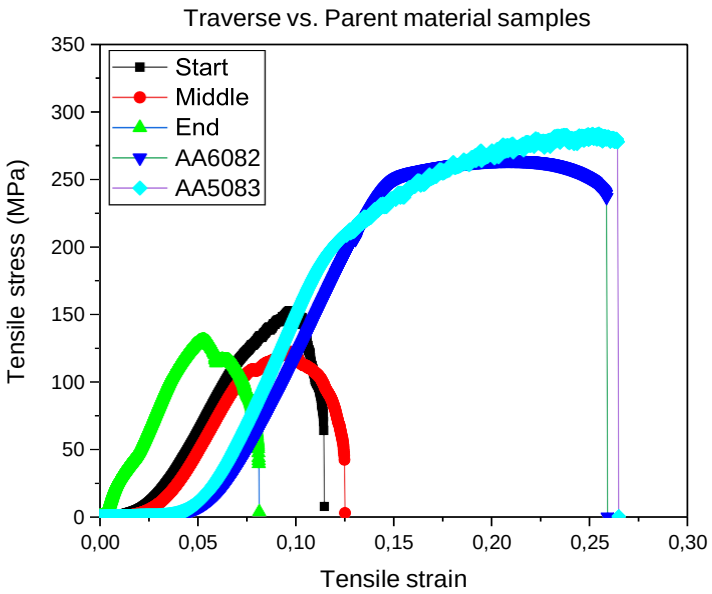

Figure 4.9: Graphical representation of traverse tensile samples vs. parent materials

The maximum ultimate tensile stress (MUTS) for the PM samples was measured at 283.889 MPa at a tensile strain of 25.55% and 264.36 MPa at a tensile strain of 20.93% for the AA5083 and AA6082, respectively. The sample taken at the joint's start position measured MUTS of 152.722 MPa at a strain of 9.72%, the middle sample at 130,694 MPa at a strain of 5.35%, and the end sample at 122.278 MPa at a strain of 9.80%. It was evident that the location from where the samples were taken had an impact on the results of the tensile strength, wherein a decrease with each sample was observed. Considering the microstructure of the samples, the findings also contradict the Hall-Petch hypothesis, which suggests that samples with finer grains often provide greater strength levels [102]. The Orowan effect, reported as possibly contributing to the rise in strength in samples travelling along the joint, may also be interpreted to be reversed in this study [108]. The decrease in MUTS can be attributted to the loss of precipitates from the high heat generated during the FSW procedure [109-111].

4.4.1.2 Tensile tests: longitudinal samples

Figure 4.10 displays the longitudinal tensile tested samples from the FS welded dissimilar joint. Each of the three samples from the SME locations experienced failure along the gauge at distances of 5, 11 and 10 mm from the lower edge of the gripping end, respectively which are encircled in the image [112- 113]. The start and middle longitudinal samples showed necking and cup-cone fracture mode, an indication of ductility, and are similar to the traverse joints, while the end sample exhibited a fracture at an angle to the gauge section. The three primary stages of ductile tensile failure are necking, cavity development and cavity coalescence [113-114]. It is reasonable to suppose that the place where the fracture occurred in the samples had a similar sequence of failure phases, and the already existing micro-voids and tunneling made it easy, accelerating the failure at those positions at the point more susceptible to failure [115]. Another possibility is that the samples' failure initiated in the areas where grain boundary migration and grain coarsening were seen (AA5083) thus opposing the Hall-Petch effect [116]. The MUTS measures were 137.417 MPa for the longitudinal sample from the joint's start location, 127.833 MPa for the middle sample, and 109.500 MPa for the end sample, all at strains of 13.8%, 8.3% and 12.7%, respectively (Figure 4.11). Similar to what was shown in the traverse samples, tensile strength testing of the samples showed a decrease with respect to the location. This again can be attributed to the reduced or absence of strengthening precipitates which are sensitive to temperature above 200 ^{o}C [109,117].

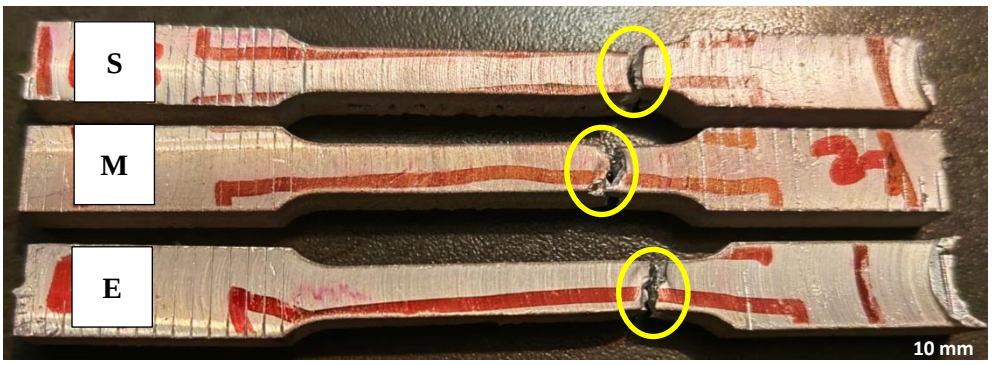

Figure 4.10: Post-test longitudinal tensile test samples

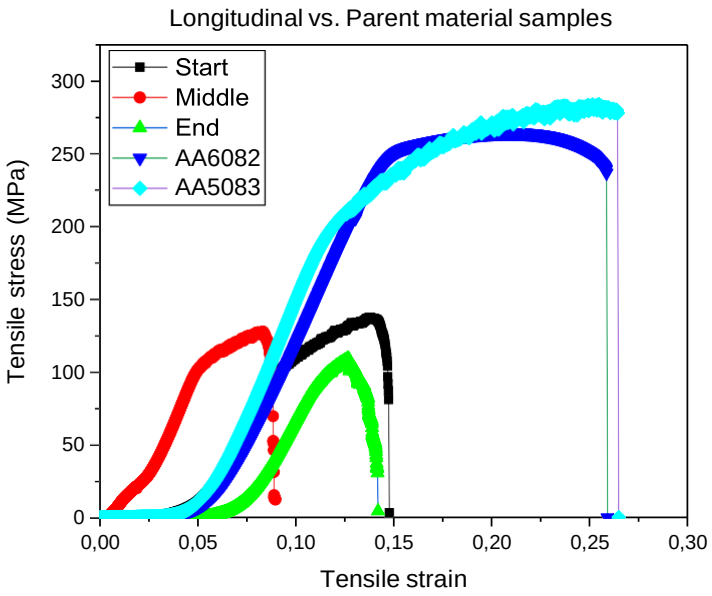

Figure 4.11: Graphical representation of longitudinal tensile samples vs. parent materials

For convenient analysis, the results of the samples have been presented in Table 4.3 in Page 61.

Table 4.3: Stress and strain values of traverse samples

ID		UTS (MPa)	Strain (%)	Fracture position
Parents	AA5083	283.889	25.55	Along gauge at 5 mm from the lower edge of the gripping end
	AA6082	264.360	20.93	Along gauge at 10 mm from the lower edge of the gripping end
Traverse	Start	152.722	9.72	SZ
	Middle	130.694	5.25	SZ
	End	122.278	9.80	SZ
Longitudinal	Start	137.417	13.80	Along the gauge at 5 mm from the lower edge of the gripping end
	Middle	127.833	8.30	Along the gauge at 11 mm from the lower edge of the gripping end
	End	109.500	12.70	Along the gauge at 10 mm from the lower edge of the gripping end

4.4.2 Flexural tests

This next section presents the flexural testing performed on the aforementioned joint samples. The three-point bending method outlined in Chapter 3 was used to test the samples at the face (side on which the welding is applied) and root to assess the flexural quality of the joints (the back side of where the welding was applied). Angles were measured using the four quadrants method, starting at 0° and progressing in the counter-clockwise direction. Figure 4.12 depicts the four-quadrant measurement graph.

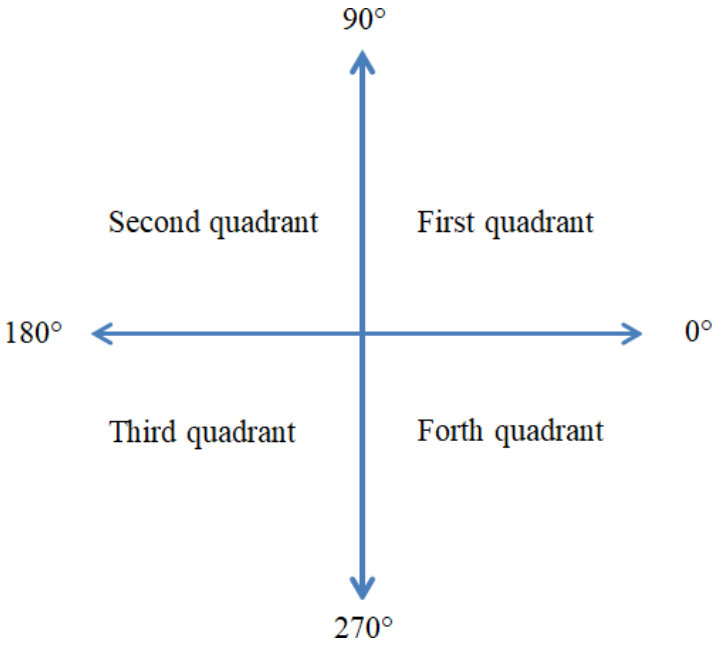

Figure 4.12: Four-quadrant measurement method

4.4.2.1 Flexural tests: traverse face

Figure 4.13 (a) depicts the side views of the bent traverse samples, and Figure 4.13 (b) depicts the outcomes of the bent surface. The start sample was measured to an angle of 40°, exhibiting meandering crack encircled in the SZ closer toward the advancing side. The failure of the start sample may have been induced by the tunnel defect that was observed, rendering it less impervious to failure [118]. The surface of the middle sample, showing a surface thinning/stretching effect, was bent to 46º. This surface stretching can be a sign that the surface material of the joint was strong enough to withstand fracture propagation. To draw attention to the failure positions on each sample, yellow boarders have been used to surround them (Figure 4.13 [b]). The key factor that could have contributed to these outcomes may have been the increased strength provided by the finely ground grains under the tool shoulder [119]. The end sample bent to an angle of 150º; cracking occurred at the interface of the TMAZ and PM (AA6082) being the softer of the two materials [120]. This one-sided behaviour shows that the joint is significantly stronger than the PM on which the failure occurred [121-122]. The graphical presentation of the traversal findings is presented in Figure 4.14. The samples' strengths were determined at the SME locations as 6.414 MPa, 47.513 MPa and 78.575 MPa, respectively, indicating an increase in relation to the position.

Figure 4.13: Face tested traverse samples (a) bent extent results and (b) surface and crack location results

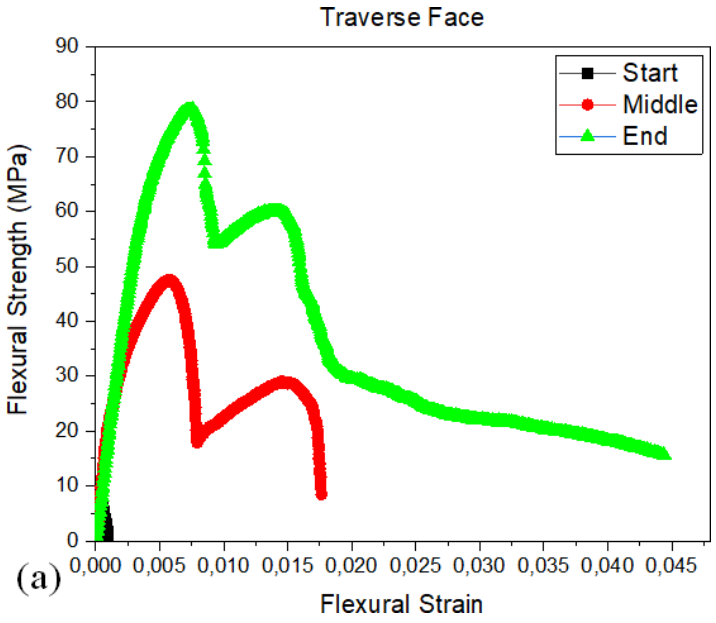

Figure 4.14: Graphical representation of the traverse samples

4.4.2.2 Flexural tests: longitudinal face

The longitudinal face-tested samples are shown in side views in Figure 4.15 (a), with their convex surfaces shown in Figure 4.15 (b). All three samples from SME positions exhibited exceptional flexural strength by achieving maximum bending angles of 140º, also attained by the PMs. Surface examinations of the samples revealed no sign of cracking on the start samples' surface; however, cracks were identified on the middle and end samples' surfaces which have been highlighted with yellow boarders on each of the failed samples (Figure 4.15 [b]) and a closer look at the fractures is shown in Figure 4.15 (c). The fracture in the middle sample is towards the flange of the bent sample, while the fracturing on the end sample is on the radius face as can be seen in Figure 4.15 (c). Rough surfaces such as grooves, one of the FSW defects,

are likely to have caused some points to be susceptible to forming fractures while under strain in the required direction, as seen in Figure 4.15 (c). Common causes of these flaws include insufficient welding force, poor tool-to-work piece surface contact or the shoulder face's shape, which promotes the buildup of concentrated stresses on the surfaces of joints [123]. Studies have reported deformation as well as misorientation of grains during the application of FSW [124]. On both samples, the crack patterns on the surfaces appeared very similar (Figure 4.15 [c]). From the fracture's contour, it may be surmised that crack nucleation occurred along individual grain boundaries which may have been arranged in a necklace pattern [125-127]. A visual depiction of the longitudinal face test results is shown in Figure 4.16. The SME samples had respective strength readings of 218.050 MPa, 272.125 MPa and 176.313 MPa. With the exception of the middle sample showing greater strength readings than the start and end samples, there is no clear trend in connection to the position.

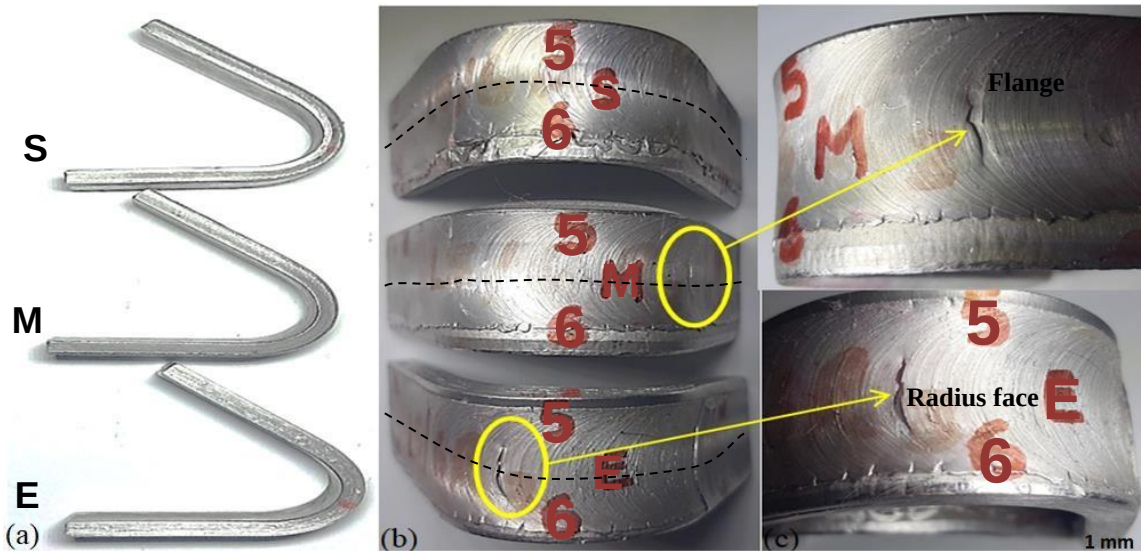

Figure 4.15: Face tested longitudinal samples (a) bent extent results, (b) surface and results (c) cracks on surfaces

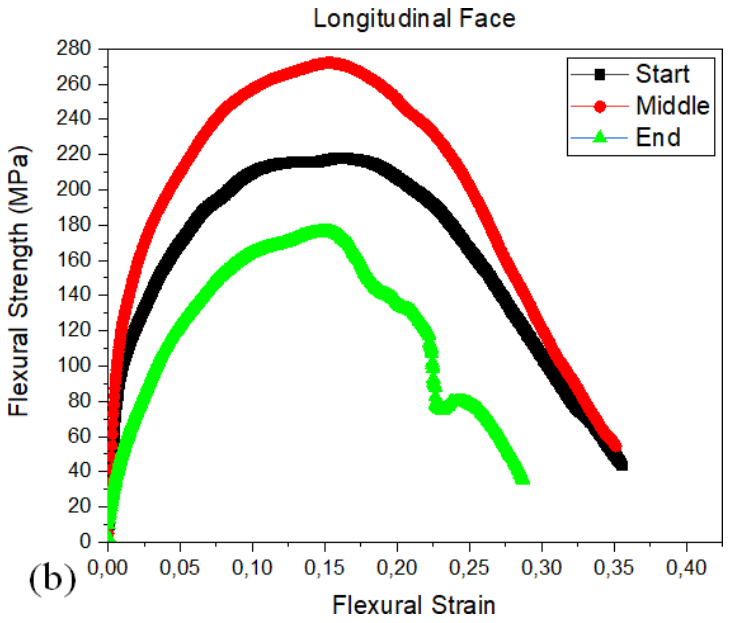

Figure 4.16: Graphical representation of the face tested traverse samples

For convenient analysis, the results of the samples have been presented in Table 4.4.

Table 4.4: Flexural strength face test analysis results

ID		UTS (MPa)	Angle (º)	Fracture position
Traverse	Start	6.414	40	SZ
	Middle	47.513	46	SZ
	End	78.575	150	TMAZ and PM interface
Longitudinal	Start	218.050	140	None
	Middle	272.125	140	Radius face
	End	176.313	140	Radius face

4.4.2.3 Flexural tests: traverse root

Figure 4.17 (a) depicts side views of the traverse root tested samples, and Figure 4.17 (b) depicts bent surfaces of the samples. All the samples from the SME locations achieved maximum deflection angles less than 90º, reaching the bending angles of 5º, 10º and 20º, respectively, as seen in Figure 4.17 (a). All three samples appeared to develop a fracture at the joint line circumscribed by yellow boarders (Figure 4.17 [b]). This behaviour may have been attributed to inadequate pressure, and a lack of penetrating or stirring, particularly at the plate's bottom [121,128-129], or in essence, the disparity between the input applied heat and the rate of heat transmission into the materials [130]. Furthermore, the joint's strength may have decreased

due to the presence of tunnel defects and internal microcracks. Furthermore, given that fine grains are known to contribute to joint strength, it is probable that the grains near the joint's bottom were less affected by the pin's churning, rendering the area more susceptible to cracking [131].

Figure 4.17: Root tested traverse samples (a) bent extent results and (b) surface and crack location results

Figure 4.18 depicts the graphical representation of the root-tested traverse sample. The SME samples measured 196.438 MPa, 47.075 MPa and 239.050 MPa, respectively. The findings revealed no obvious trend or evidence of samples taken from different locations. The results showed a significant decline in the middle sample before rising by 80% in the final sample.

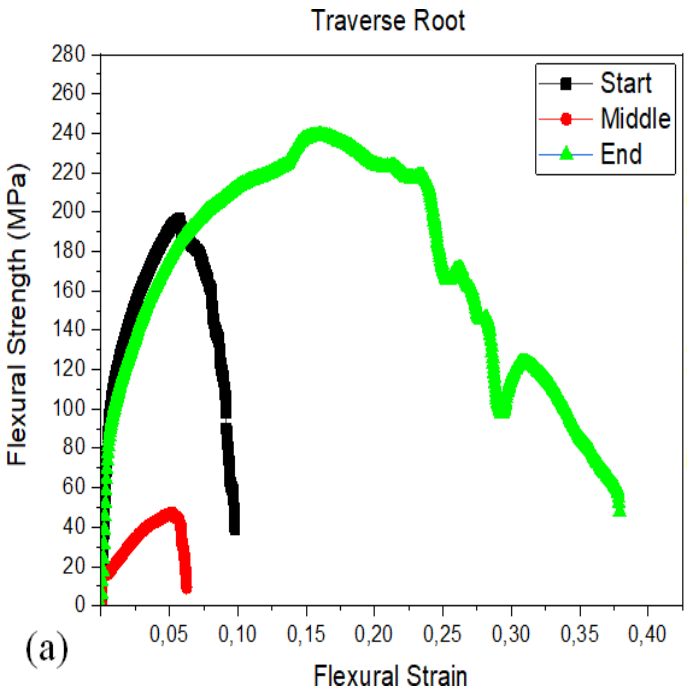

Figure 4.18: Graphical representation of the traverse root tested samples

4.4.2.4 Flexural tests: longitudinal root

Figure 4.19 (a) depicts side views of longitudinal root tested samples, whilst Figure 4.19 (b) depicts convex surfaces from SME locations. The root start sample bent at a 140° angle, and when its surface was examined, a fracture was observed at the joint line. A 140º bend angle was likewise attained by the middle sample, and inspections of its surface showed no discernible cracks. The end sample reached a bend angle of 135º. The advancing side of the joint of this sample was found to have a crack that was advancing towards the centre of the sample. Yellow boarders have been used to delineate each sample's failures on the radius face (Figure 4.19 (b)) and Figure 4.19 (c) offers a closer look at the fractures. The AA5083 material's susceptibility to failure may have been caused by the coarsened grains observed in the microstructure of the longitudinal samples [93]. As was previously supposed, the inefficiencies are brought about by incompatible parameters, resulting in subpar mechanical outputs and undesired joint defects [121,128-129].

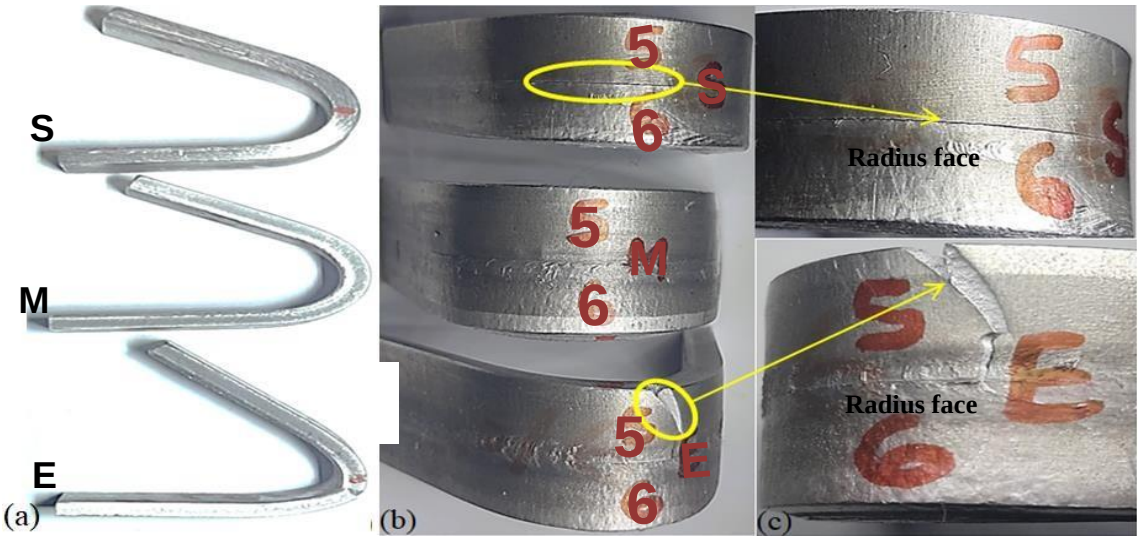

Figure 4.19: Root-tested traverse samples (a) bent extent results and (b) surface and crack location results

Strength measurements for the samples from the SME locations were 108.250 MPa, 198.888 MPa and 196.438 MPa, respectively (Figure 4.20). The results showed variance, with the middle samples exhibiting greater values than those of the start and end samples.

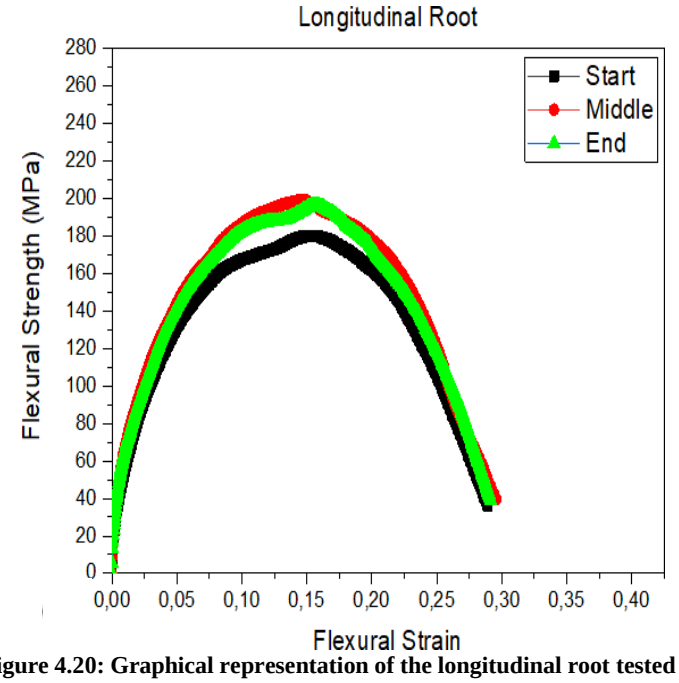

Figure 4.20: Graphical representation of the longitudinal root tested samples

For convenient analysis, the results of the samples have been presented in Table 4.5.

Table 4.5: Flexural strength root test analysis results

ID		UTS (MPa)	Angle (°)	Fracture position
Traverse	Start	196.438	5	SZ
	Middle	47.075	10	SZ
	End	239.050	20	SZ
Longitudinal	Start	108.250	140	SZ radius face
	Middle	198.888	140	None
	End	196.438	135	SZ radius face

4.4.3 Microhardness test

This section details the Vickers microhardness results of the AA5083/AA6082 dissimilar joint and its parent materials. Figures 4.21, 4.22 and 4.23 depict the graphical representation of the microhardness profiles of the start, middle and end samples, respectively. It should be noted that the information shown in the graphs is comprised of the mean values of the three rows of initial findings from the samples. The mean microhardness values for AA5083 with a mean of 83.93 $HV_{0.2}$ and AA6082 measured a mean microhardness of 97.701 $HV_{0.2}$

4.4.3.1 Microhardness: start sample

The graphical depiction of the start samples for the traverse and longitudinal samples as well as the PMs is presented in Figure 4.21. The traverse sample measured a mean of 79.70 $HV_{0.2.}$ The longitudinal portions of the samples, AA5083 and AA6082, measured a mean of 100.59 $HV_{0.2}$ with a range of 77.92 and 139.54 $HV_{0.2}$ and 104.84 $HV_{0.2}$ with a range of 90.70 and 153.73 $HV_{0.2}$, respectively. The joints had higher hardness than that determined from the parent materials after considering the mean micro-hardness values obtained from both the parent samples and the welded samples. The AA6082 section had the highest hardness of the evaluated samples. This is described as the Hall-Petch relation, which explains that having finer grains yields higher hardness values, as observed in the microstructure where AA6082 exhibited very fine, recrystallised grains [132-133].

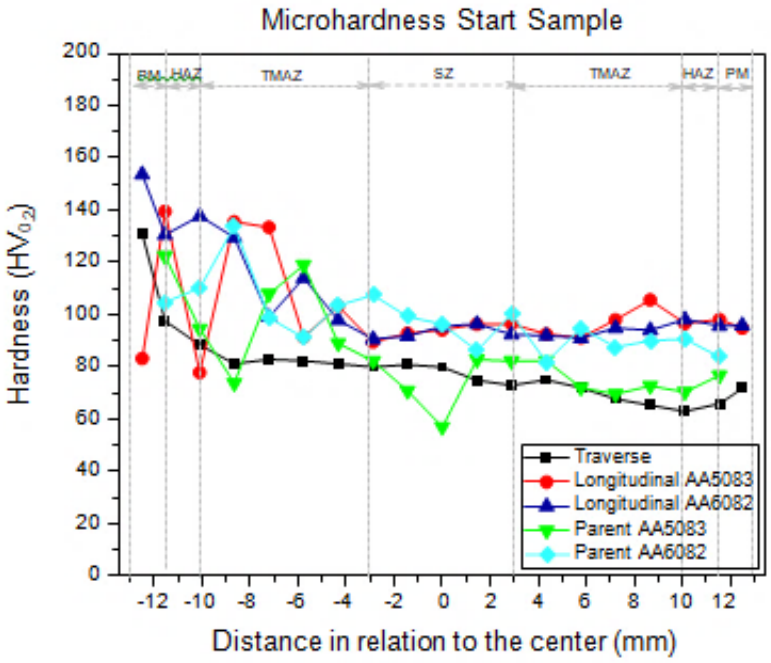

Figure 4.21: Graphical hardness representation start samples traverse and longitudinal and parent materials

4.4.3.2 Micro-hardness: middle sample

The middle samples hardness (Figure 4.22) for the traverse measured at 75.152 with ranges from 59.89 and 88.73 $HV_{0.2.}$ The longitudinal sections of AA5083 and AA6082 both measured 73.385 $HV_{0.2}$, with ranges from 55.77 and 102.60 $HV_{0.2}$. The similarity in the results of the middle sample indicates an even distribution of similar materials in the advancing and retreating sides of the joint. The mean hardness values of the samples showed a decline when compared to

the PMs results. According to studies, an uneven distribution of precipitates in the samples is primarily to blame for the reduction of hardness at joints between dissimilar materials [134]. Assuming that the measurements were primarily obtained from regions of the longitudinal samples that included the AA5083 material, reduced hardness in the joint could be ascribed to coarse grain dominance observed in the microstructure images [135].

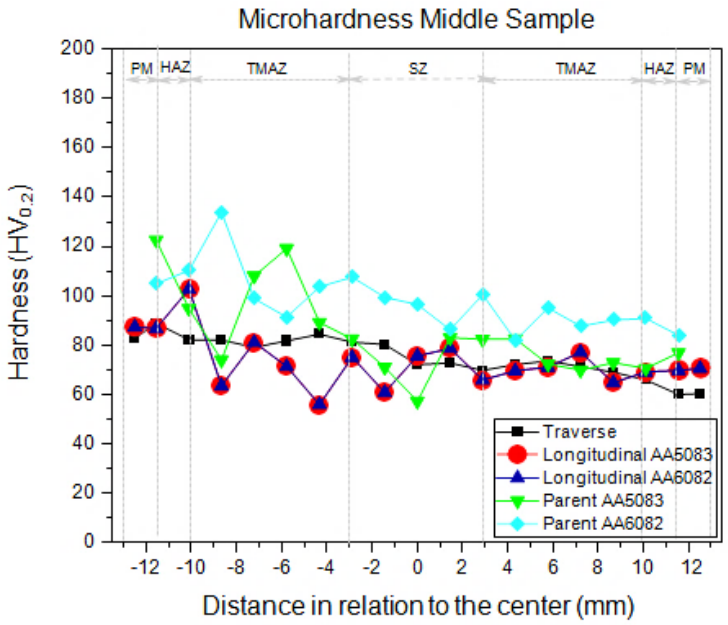

Figure 4.22: Graphical hardness representation middle samples traverse and longitudinal and parent materials

4.4.3.3 Microhardness: end sample

Figure 4.23 depicts the results of the end samples. The traverse sample mean micro-hardness was measured as 78.79 $HV_{0.2.}$ The longitudinal AA5083 and AA6082 sections measured mean hardness values of 79.555 and 76.641 $HV_{0.2}$ respectively. Similar to the middle samples, a drop was identified in the microhardness values of the joint samples. As mentioned previously, drops in hardness of samples are typically the result of uneven precipitate distributions and coarsening [135].

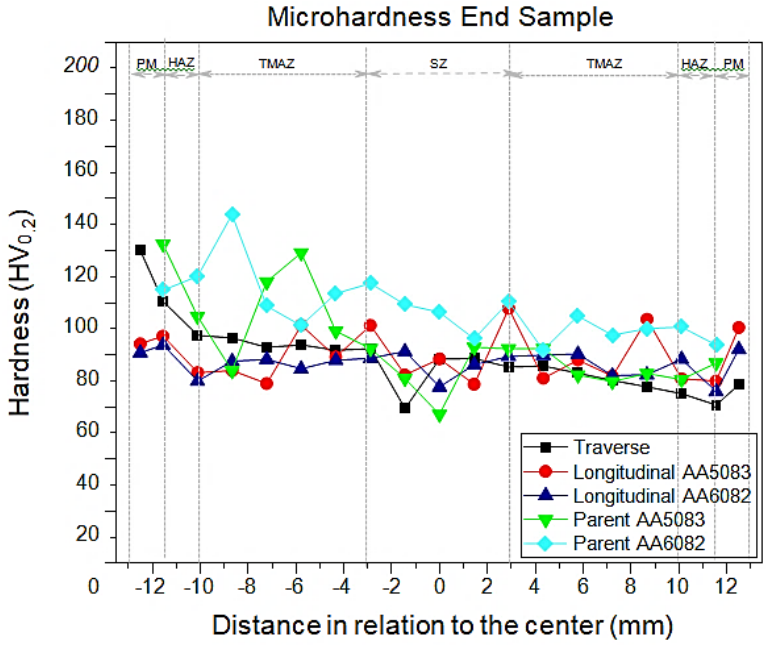

Figure 4.23: Graphical hardness representation end samples traverse and longitudinal and parent materials

4.5 Fractographic inspection

A Tescan MIRA SEM was utilised to conduct examinations of the fracture morphology of the tensile tested samples in order to unravel the fracture mechanism of the welded joint between AA5083 and AA6082. Figures 4.24 (a)–(c) depict fractographs at 50× low magnification while Figures 4.24 (d)–(f) depict at 2000× magnification.

4.5.1 Fractographic inspection: traverse

Figures 4.24 (a) and (d) depict the fractographs for the start traverse sample. The samples' low-magnification photograph is depicted in Figure 4.24 (a). The image depicts a slew of defects, including tunnel pockets and micro-voids. The development of pockets might have been caused by unfilled gaps that occurred during stirring as a result of the material not being sufficiently plasticised by the applied temperatures. Figures 4.24 (b) and (e) depict the middle traverse sample. From the fractograph shown, major tunnels were observed. Additional to what had already been posited as the cause of tunnels, it may be that fissures in the joint were unfilled due to insufficient material deposits brought on by accelerated heat dissipation, allowing the formation of cold welds [89]. Figures 4.24 (c) and (f) depict the end traverse sample. Similar to the start and middle samples, this sample had micro-voids and tunnel defects. The high magnification image reveals various and unevenly sized dimples. It was also observed that the same sample exhibited cleavage facets and voids. The formation of large dimples indicates that

the material underwent an adequate malleable course and should result in high ductility while those with smaller dimples indicate a reduction in the ductility of the material [136]. Shattered particles were observed embedded at the base of the bigger dimples. It is clear from the particles at the bottom of the dimples that precipitate coarsening transpired, which is why the samples' strength was lower than that of the PMs [137].

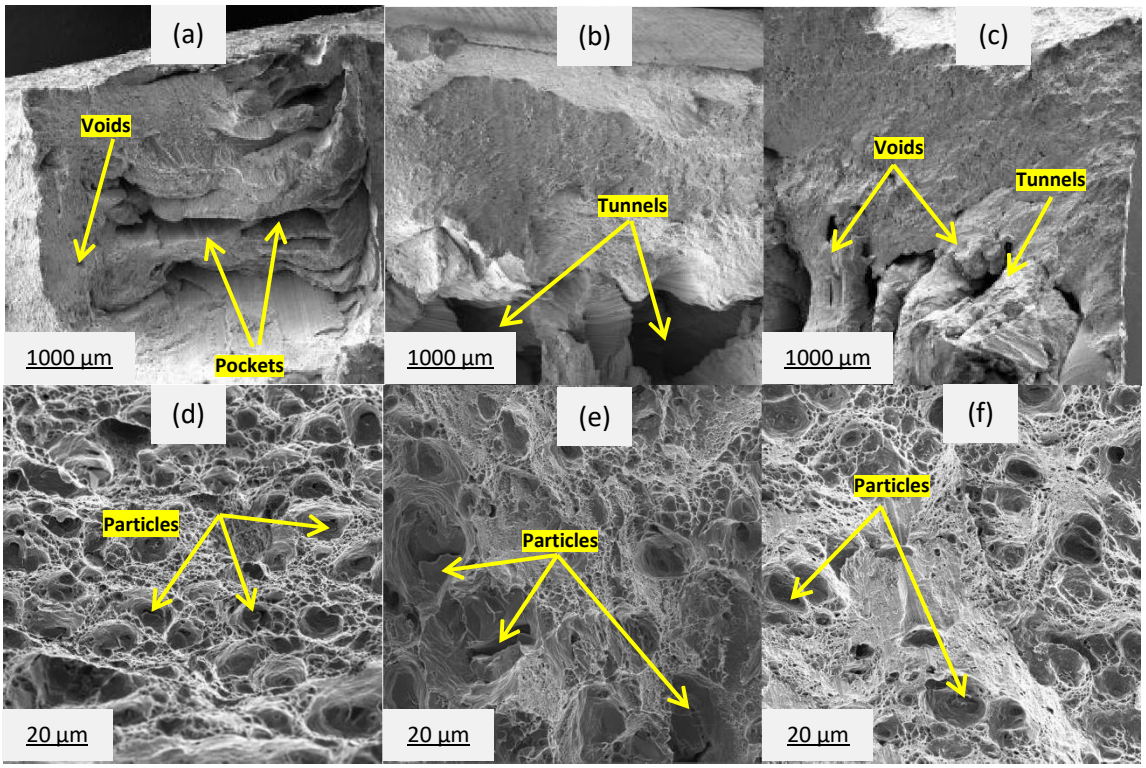

Figure 4.24: Traverse SEM sample: low magnification images (a) start, (b) middle and (c) end locations; high magnification images (a) start, (b) middle and (c) end locations

4.5.2 Fractographic inspection: longitudinal

The fractographs for a start longitudinal sample are shown in Figures 4.25 (a) and (d). Figure 4.25 (a) shows a low-magnification image of the samples. Figures 4.25 (a)–(c) depict images at 50× low magnification and at 2000× high magnification in Figures 4.25 (d)–(f). Figure 4.25 (a) depicts the start longitudinal sample exhibiting cleavages on its surface and micro- voids. Cleavages are typically associated with ductile and brittle fractures from uneven heat distribution that results in poor mixing of the material [138]. High-magnification images show a variety of dimples in various sizes, with a significant area on the sample predominately composed of fine dimples that assist in explicating the cleavage appearance on samples known to be associated with quasi-cleavage mode [139]. Similar to the start sample, the middle sample is depicted in Figure 4.25 (b) at low magnification; this image reveals a surface

that appears to be cleaved. The image at high magnification (Figure 4.25[e]) showed regions with smooth surfaces and other areas with dimples of various sizes. At the bottom of the dimples, there were shattered pieces inside. Results at higher magnification are comparable to those in traverse samples where particle-filled dimples of various sizes are observed. Images at high magnification show a variety of dimples of varying sizes, with a significant area on the end sample showing a cleavage surface. The middle sample is shown in Figure 4.25 (b); this sample has cleavages and voids. Low magnification images of the end sample revealed void, fracture, cleavage and tunnel defects (Figure 4.25[c]). A variety of dimples of various sizes are visible on the sample's face, as well as sections with flat surfaces, in the high magnification photograph as shown in Figure 4.25 (f). Moreover, the distribution of particles throughout the sample's surface was observed. The end sample showed intermetallic particles dispersed over the sample face, much like with the start and middle samples.

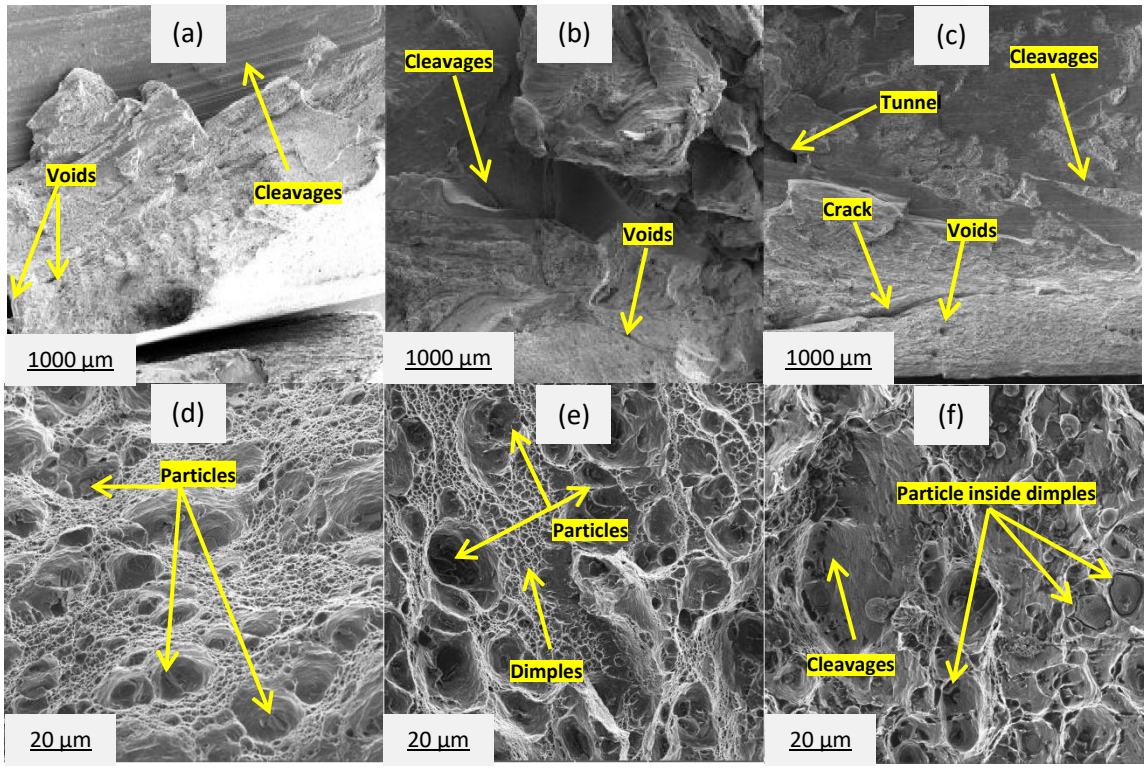

Figure 4.25: Longitudinal SEM sample: low magnification images (a) start, (b) middle and (c) end locations; high magnification images (a) start, (b) middle and (c) end locations

CHAP TER 5

CONCLUSION & RECOMMENDATIONS

This section discusses the study's findings and recommendations in light of all that has been investigated and reported in previous sections.

5.1 Conclusion

The correlative analysis between sampling direction and the mechanical properties of the friction stir welded AA5083/AA6082 dissimilar joints was conducted. This study sought to determine and characterise the relationship between the sample's location (start, middle and end), direction (traverse and longitudinal) and the mechanical properties of the friction stir-welded AA5083/AA6082 dissimilar butt joint. The samples were extracted using a waterjet machine; 6 mm thick plates were welded using a modified milling machine. Visual tests, metallographic tests including macro-structural analysis, microstructural analysis, and fractography, as well as mechanical tests including tensile testing, three-point flexural tests and micro-hardness tests, were all employed to assess the joint's quality and characterisation.

The traverse samples' macrostructure analysis identified the four main FS welded joint zones: the parent material zone (PM), heat affected zone (HAZ), thermo-mechanically affected zone (TMAZ) and stir zone (SZ). Given the inter-material flow pattern, this was also an apparent sign that the material in the joint had plasticised. However, the presence of tunnel defect suggests that it could not have plasticised sufficiently, which may also account for the underdeveloped SZ. This ultimately led to the lack of onion rings in the samples from all the locations. Micro-voids were also found in the samples, mostly on the advancing side, directly underneath the bands of material. The samples' longitudinal view showed a layering of the materials, and a tunnel defect was revealed to extend throughout the length of the samples and had micro-voids at certain areas of the materials' interfaces.

Microstructure examinations of the traverse samples revealed that a considerable measure of strain and high temperatures occurred in the sample. This resulted in the joint materials undergoing dynamic recrystallisation. While AA5083 showed no discernible grains, AA6082 had tiny grains that resembled shards of glass. The mean grain size of the traverse start

sample was 10.328 µm with a standard deviation (SD) of 3.934 µm; the mean grain size of the middle sample was 11.884 µm with an SD of 4.491 µm; and the mean grain size of the traverse end sample was 7.618 µm with an SD of 3.854 µm. On the microstructure and the location where the samples were taken, there was no evident correlation. The longitudinal samples exhibited AA6082 material that had undergone dynamic recrystallisation with an appearance of shards of glass, similar to the traverse samples. However, AA5083 displayed varying traits with an extremely thick appearance, indicating that grain boundary migration caused by aberrant grain filling had occurred. The grain was measured in the longitudinal start samples at 15.608 µm with an SD of 6.839 µm; in the middle sample at 19.881 µm with an SD of 14.022 µm; and in the end sample at 9.187 µm with an SD of 3.827 µm.

Tensile test examinations of the traverse samples revealed the SZ as the location of failure in all samples. All samples displayed a cup-cone fracture mode, a mode peculiar to plastic deformation found in ductile materials, a meandering tear and a slight necking. The fact that it was present also suggests that differing temperatures were encountered at various depths and that tool effects may have been minimal in the bottom half of the samples. The samples obtained at the start, middle and end of the joint recorded MUTS of 152.722 MPa, 130.694 MPa, and 122.278 MPa, respectively, at strains of 5.35%, 9.72% and 9.80%, respectively. The longitudinal tensile samples encountered failure along the gauge at a distance of 5, 11 and 10 mm from the lower edge of the gripping end. The region of failure in the samples was considered to be caused by the discovered tunnel and micro-void defects, which made it simple for the ductile failure to occur. Another hypothesis was that, in light of what was observed in the AA5083 material displaying coarse grains, the grains in certain areas were coarser than those in other regions, rendering the position less resistant to failure. The MUTS measurements were 137.417 MPa for the longitudinal sample taken from the joint's start location, 127.833 MPa for the middle sample, and 109.500 MPa for the end sample, all at strains of 13.8%, 8.3% and 12.7%, respectively. The traverse and longitudinal sample results showed a decrease in sample strength.

Face evaluated for flexural traverse samples presented that the start sample was bent to an angle of 40°, exhibiting a meandering crack in the SZ closer to the advancing side. The middle sample demonstrated surface thinning/stretching and was bent to 46º, with surface stretching strong enough to withstand fracture propagation through to the surface. This was assumed to be related to the presence of fine grains in the joint's top layer. The end sample

bent at a 150º angle and cracked at the interface of the TMAZ and PM (AA6082), being the softer of the two materials. The sample strengths were determined to be 6.414 MPa, 47.513 MPa and 78.575 MPa, respectively, at the SME locations, suggesting an increase in relation to location. Face tested longitudinal samples had exceptional flexural strength, with maximum bending angles reaching 140º. Surface examinations of the samples revealed no evidence of cracking on the surface of the start samples; however, cracks were noted on the surfaces of the middle and end samples. Rough surfaces, such as grooves, were determined to cause the regions to fracture while under strain. The strength measurements for the SME samples were 218.05 MPa, 272.125 MPa and 176.313 MPa, respectively.

Root evaluated traverse samples had maximum deflection angles less than 90º, with bending angles of 5º, 10º and 20º. All three samples fractured along the joint line. This behaviour was ascribed to insufficient pressure and a lack of penetration or stirring, especially at the plate's bottom. SME samples had a strength of 196.438 MPa, 47.075 MPa and 239.05 MPa, respectively. There was no trend in sample position and location, as the middle sample rose by 80% in the final sample after dropping from the start sample strength. The longitudinal samples featured bend angles of 140º for the start and middle samples, and 135º for the end sample. The root start sample had a fracture at the joint line, while the middle sample had no discernible cracks. The end sample was discovered to have a fracture progressing towards the centre of the sample. Strength measurements for the samples from the SME locations were 108.250 MPa, 198.888 MPa and 196.438 MPa, respectively.

Micro-hardness evaluation of the traverse start sample measured a mean $HV_{0.2}$ of 79.70. The longitudinal parts of the samples, AA5083 and AA6082, had mean values of 100.59 $HV_{0.2}$ and 104.84 $HV_{0.2}$, respectively. The joints had higher micro-hardness than that determined from the parent materials after taking into account the mean micro-hardness values obtained from both the parent samples and the welded samples. The traverse middle sample measured 75.152 $HV_{0.2}$ while the AA5083 and AA6082 sections both measured 73.385 $HV_{0.2}$. The mean micro-hardness values of the samples showed a decline when compared to the PMs results. The traverse end sample mean micro-hardness was measured at 78.79 $HV_{0.2.}$ The longitudinal AA5083 and AA6082 sections measured mean micro-hardness values of 79.555 and 76.641 $HV_{0.2}$ respectively. According to the Orowan mechanism and the Hall-Petch, there is a correlation with the hardness and grain sizes.

Micro-voids and tunnel flaws were discovered during the fractographic investigation of the start, middle and end traverse samples. The high magnification picture reveals a variety of dimples of varying sizes. There were also cleavage facets and voids in the samples. The appearance of huge dimples implies that the material has undergone a sufficiently malleable course, confirming the material's ductility. Shattered particles were discovered at the base of the larger dimples seen at the bottom, which was identified as the cause of the joint's weakness. The longitudinal sample had surface cleavages and micro-voids, indicating that it had undergone ductile and brittle fractures. At high magnification, the image revealed parts with smooth surfaces and others with dimples of varying sizes. The dimples, like the traverse samples, had particles embedded at their bottoms.

From the results of this study, it is evident that the joint was comparable to the parent materials in both directions and position despite the presence of tunnel and micro-void defects that may have led to some of the lower results.

5.2 Recommendations

Traverse and longitudinal examinations were conducted on FS welded dissimilar joints of AA5083/AA6082. According to the findings of this investigation, attributes of the parents and the joints (traverse and longitudinal) were comparable to each other. Based on these findings, varying tools with different contoured pins and different speed (traverse and rotation) ranges should be applied to investigate their impact on joint characteristics. Other mechanical and metallographic exams can be employed to examine the properties of the joint further having observed some variations, especially in the microstructure of the samples.

REFERENCES

[1] Dwight, J., 1998. *Aluminium design and construction.* CRC Press.

[2] Lumley, R. N., 2010. *Fundamentals of aluminium metallurgy: production, processing and applications.* Elsevier.

[3] Olabode, M., Kah, P. and Martikainen, J., 2013. *Aluminium alloys welding processes: challenges, joint types and process selection.* Proceedings of the Institution of Mechanical Engineers, Part B: Journal of Engineering Manufacture, 227(8), pp.1129- 1137.

[4] Kartsonakis, I.A., Dragatogiannis, D.A., Koumoulos, E.P., Karantonis, A. and Charitidis, C.A., 2016. *Corrosion behaviour of dissimilar friction stir welded aluminium alloys reinforced with nanoadditives*. Materials & Design, 102, pp.56-67.

[5] Davis, J. R., 2001. *Aluminum and Aluminum Alloys*, pp. 351–416.

[6] Duparc, O.H., 2005. *Alfred Wilm and the beginnings of Duralumin.* Zeitschrift fuer Metallkunde/Materials Research and Advanced Techniques.

[7] Muster, T. H., Hughes, A. E., & Thompson, G. E., 2009. *Copper Distributions in Aluminium Alloys.* New York (p. 116). Nova Science Publishers.

[8] Kobe Steel, 2015. *Welding of Non-Ferrous Metals, The Arc Welding of Nonferrous Metals*, pp. 1–83.
<https://www.kobelco.co.jp/english/welding/events/files/2015_KOBELCO_Specific.pdf.>
[Accessed 06 June 2021]

[9] Joseph, O. O., Olubambi, P. A., Joseph, O. O., Edun, B. M., Okeniyi, J. O., & Abioye, O. P., 2021. *Effects of Alloying on Aluminium-Silicon Alloys – A Review*. IOP Conference Series: Materials Science and Engineering, 1107(1), 012116.

[10] Nese, O., 2016. *Corrosion properties of AA5083 and AA6082 in seawater-effect of temperature, pH and* potential (Master's thesis, NTNU).

[11] Fontana, M.G., 1986. *Corrosion principles*. *Corrosion engineering*, pp.12-38.

[12] Al-Sherrawi, M.H., Lyashenko, V., Edaan, E.M. and Sotnik, S., 2018. *Corrosion of metal construction structures.*

[13] Vargel, C., Jacques, M. and Schmidt, M.P., Corrosion of aluminium. 2004.

[14] Harsimran, S., Santosh, K. and Rakesh, K., 2021. Overview of corrosion and its control: A critical review. Proceedings on Engineering, 3(1), pp.13-24.

[15] Bahadori, A., 2014. Corrosion and materials selection: a guide for the chemical and petroleum industries. John Wiley & Sons.

[16] Canepa, E., Stifanese, R., Merotto, L. and Traverso, P., 2018. *Corrosion behaviour of*

aluminium alloys in deep-sea environment: A review and the KM3NeT test results. Marine structures, 59, pp.271-284.

[17] Sukiman, N.L., Zhou, X., Birbilis, N., Hughes, A.E., Mol, J.M.C., Garcia, S.J., Zhou, X. and Thompson, G.E., 2012. *Durability and Corrosion of Aluminium and Its Alloys: Overview, Property Space, Techniques and Developments. Aluminium Alloys-New Trends in Fabrication and Applications*, *5*, pp.47-97.

[18] Adeosun, S.O., Sekunowo, O.I., Balogun, S.A. and Obiekea, V.D., 2012. *Corrosion behaviour of heat-treated aluminum-magnesium alloy in Chloride and EXCO Environments*. International Journal of Corrosion, International Journal of corrosion, 9, pp. 1-9

[19] Abolusoro, O.P. and Akinlabi, E.T., 2019. *Wear and corrosion behaviour of friction stir welded aluminium alloys—an overview*. International Journal of Mechanical and Production Engineering Research and Development, 9(3), pp.967-982.

[20] Lacki, P., Więckowski, W. and Wieczorek, P., 2015. *Assessment of joints using friction stir welding and refill friction stir spot welding methods.* Archives of Metallurgy and Materials, 60, pp. 2297–2306.

[21] Stepinski, T., Lingvall, F., Wennerström, E. and Ping, W., 2004. *Inspection of copper canisters for spent nuclear fuel by means of ultrasound*. NDE of friction stir welds, nonlinear acoustics, ultrasonic imaging (No. SKB-TR--04-03). Swedish Nuclear Fuel and Waste Management Co..

[22] Khan, A.A., 2001. *Guide Book for the Fabrication of Non-Destructive Testing (NDT) Test Specimen.*

[23] International Atomic Energy Agency, 2001. *Guidebook for the Fabrication of Non-Destructive.*

[24] Hobart Institute of Welding, 2010. *Destructive Testing Methods Training Workbook.*

[25] American Welding Society, American Welding Society. Committee on Mechanical Testing of Welds and American Welding Society. Technical Activities Committee, 2007. *Standard methods for mechanical testing of welds*. American Welding Society.

[26] Abnar, B., Kazeminezhad, M. and Kokabi, A.H., 2015. *Effects of heat input in friction stir welding on microstructure and mechanical properties of AA3003-H18 plates*. Transactions of Nonferrous Metals Society of China, 25(7), pp.2147-2155.

[27] Khan, N.Z., Siddiquee, A.N. and Khan, Z.A., 2017. *Friction stir welding: dissimilar aluminum alloys. CRC* Press.

[28] Mishra, R.S. and Sidhar, H., 2016. *Friction stir welding of 2xxx aluminum alloys including Al-Li alloys*. Butterworth-Heinemann.

[29] Megastir, 2018, Friction Stir Welding Vs. Fusion Welding [Image]. <Https://Megastir.Com/Trad-Vs-Stir-Welding/> [Accessed 06 June 2021]

[30] Kumar, H.A., Ramana, V.V. and Pawar, M., 2018, March. *Experimental Study on Dissimilar Friction Stir welding of Aluminium Alloys (5083-H111 and 6082-T6) to investigate the mechanical properties.* In IOP Conference Series: Materials Science and Engineering (Vol. 330, No. 1, p. 012076). IOP Publishing.

[31] Buffa, G., Campanella, D., Di Lorenzo, R., Fratini, L. and Ingarao, G., 2017. *Analysis of electrical energy demands in friction stir welding of aluminum alloys.* Procedia Engineering, 183, pp.206-212.

[32] Verma, S., Kumar, V., Kumar, R. and Sidhu, R.S., 2021. *Exploring the application domain of friction stir welding in aluminum and other alloys.* Materials Today: Proceedings, 50, pp.1032-1042.

[33] Phillips, D. H., 2016. https://boilersinfo.com/. 1st edn. Edited by D. Phillips. John Wiley & Sons, Ltd Registered.

[34] Godiganur, V.S. and Biradar, S., 2014. *Comparison of friction stirs welding technique with conventional welding methods.* International Journal of Research in Engineering and Technology, 3(04).

[35] Siddiqui, M.A., Jafri, S.A.H., Bharti, P.K. and Kumar, P., 2014. *Friction stir welding as a joining process through modified conventional milling machine: A review.* International Journal of Innovative Research & Development, 3(7), pp.149-153.

[36] Kristensen, V.B., 2020. *Langenuen Suspension Bridge Aluminium Bridge Grider Alternative*.

[37] Kallee, S.W., 2010. *Industrial applications of friction stir welding*. In Friction stir welding (pp. 118-163). Woodhead Publishing.

[38] Yisong, W., Jianhua, T. and Congqing, L., 2012. *Application of Friction Stir Welding on the Large Aircraft Floor Structure.* China FSW Center, BAMTRI.

[39] Prabha, K.A., Putha, P.K. and Prasad, B.S., 2018. *Effect of tool rotational speed on mechanical properties of aluminium alloy 5083 weldments in friction stir welding*. Materials Today: Proceedings, 5(9), pp.18535-18543.

[40] Birol, Y. and Kasman, S., 2013. *Effect of welding parameters on microstructure and mechanical properties of friction stir welded EN AW 5083 H111 plates.* Materials Science and Technology, 29(11), pp.1354-1362.

[41] Al-Roubaiy, A.O., Nabat, S.M. and Batako, A.D., 2020. *An Investigation into Friction Stir Welding of Aluminium Alloy 5083-H116 Similar Joints.* Materials Today: Proceedings, 22,

pp.2140-2152.

[42] Ravindar, B., Gururaj, K. and Reddy, A.S., 2015. *The Influence Of Process Parameters On Microhardness And Mechanical Properties Of FSW Aluminium 5083 Alloy Butt Joint*. International Journal Of Engineering Sciences & Research Technology.

[43] Ullegaddi, K., Murthy, V. and Harsha, R.N., 2017. *Friction stir welding tool design and their effect on welding of AA-6082 T6.* Materials Today: Proceedings, 4(8), pp.7962-7970.

[44] Forcellese, A., Simoncini, M. and Casalino, G., 2017. *Influence of process parameters on the vertical forces generated during friction stir welding of AA6082-T6 and on the mechanical properties of the joints*. Metals, 7(9), p.350.

[45] Gopi, S. and Manonmani, K., 2012. *Influence of shoulder profile and shoulder penetration on joint strength; of friction stir welded AA6082 in conventional milling machine*. European Journal of Scientific Research, 73(1), pp.20-32.

[46] Adamowski, J., Gambaro, C., Lertora, E., Ponte, M. and Szkodo, M., 2007. *Analysis of FSW welds made of aluminium alloy AW6082-T6.* Archives of Materials Science and Engineering, 28(8), pp.453-460.

[47] Kumar, H.A. and Ramana, V.V., 2020. Influence of tool parameters on the tensile properties of friction stir welded aluminium 5083 and 6082 alloys. Materials Today: Proceedings, 27, pp.951-957.

[48] Sarathkumar, E., Venkatesan, K., Sundararaj, P., 2019. *Optimization And Characterization Of Dissimilar Welding Of AA5083 & AA6082 Aluminium Alloys* 5088–5093.

[49] Kasirajan, T., Ravindran, R., ... Selvakumar, M., 2020. *Investigation of the microstructural, mechanical, and thermal evolution of dissimilar aluminium alloys during friction stir welding.* Transactions of the Canadian Society for Mechanical Engineering 44, 38–48

[50] Kumar, R. and Pancholi, V., 2021. *Three-dimensional material flow during friction stir welding of AA5083. Journal of Manufacturing Processes,* 68, pp.1214-1223.

[51] Torzewski, J., Grzelak, K., Wachowski, M. and Kosturek, R., 2020. *Microstructure and low cycle fatigue properties of AA5083 H111 friction stir welded joint*. Materials, 13(10), p.2381.

[52] Zhou, N., Song, D., Qi, W., Li, X., Zou, J. and Attallah, M.M., 2018. *Influence of the kissing bond on the mechanical properties and fracture behaviour of AA5083-H112 friction stir welds*. Materials Science and Engineering: A, 719, pp.12-20.

[53] Dada, O.J., 2020. *Fracture mechanics and mechanical behaviour in AA5083-H111 friction stir welds*. Scientific African 8.

[54] Mroczka, K., Pietras, A. and Kurtyka, P., 2012. *Microstructure and properties of 6082 aluminium alloy friction stir welded with different parameters of welding.* Zvaranie/Svarovani, 61(1-2), pp.7-12.

[55] Cavaliere, P., Squillace, A. and Panella, F., 2008. *Effect of welding parameters on mechanical and microstructural properties of AA6082 joints produced by friction stir welding.* Journal of materials processing technology, 200(1-3), pp.364-372.

[56] Khan, N., Rathee, S. and Srivastav, M., 2021. *Parametric optimization of friction stir welding of Al-Mg-Si alloy: A case study*. Yugoslav Journal of Operations Research, (00), pp.7-7.

[57] Kasman, S., Kahraman, F., Emiralioğlu, A. and Kahraman, H., 2017. *A case study for the welding of dissimilar EN AW 6082 and EN AW 5083 aluminum alloys by friction stir welding*. Metals, 7(1), p.6.

[58] Gungor, B., Kaluc, E., Taban, E. and Sik, A., 2014. *Mechanical, fatigue and microstructural properties of friction stir welded 5083-H111 and 6082-T651 aluminum alloys*. Materials & Design (1980-2015), 56, pp.84-90.

[59] Cho, J.H., Kim, W.J. and Lee, C.G., 2014. *Evolution of microstructure and mechanical properties during friction stir welding of A5083 and A6082*. Procedia Engineering, 81, pp.2080-2085.

[60] Svensson, L.E., Karlsson, L., Larsson, H., Karlsson, B., Fazzini, M. and Karlsson, J., 2000. *Microstructure and mechanical properties of friction stir welded aluminium alloys with special reference to AA 5083 and AA 6082*. Science and technology of welding and joining, 5(5), pp.285-296.

[61] Brum, N., Amavisca, C., Schroeder, J.G., Buzzatti, J., Lemos, G.V.B., Tolotti, D. and Favaro, M., 2021. *Influence of process parameters on mechanical properties of friction stir welded 5083-O aluminum alloy.* Tecnologia em Metalurgia, Materiais e Mineração, 18, pp.0-0.

[62] Babu, G.R., Murti, K.G.K. and Janardhana, G.R., 2008. *An experimental study on the effect of welding parameters on mechanical and microstructural properties of AA 6082-T6 friction stir welded butt joints*. ARPN Journal of engineering and applied sciences, 3(5), pp.68-73.

[63] Srinivasulu, P., Rao, G.K.M. and Gupta, M.S., 2015. *Evaluation of bending strength of friction stir welded AA 6082 aluminum alloy butt joints*. International Journal of Advance Research in Science and Engineering, 4(1), pp.1262-1270.

[64] Dickerson, T.L. and Przydatek, J., 2003. *Fatigue of friction stir welds in aluminium alloys*

that contain root flaws. International Journal of Fatigue, 25(12), pp.1399-1409.

[65] Saravanakumar, R., Krishna, K., Rajasekaran, T. and Siranjeevi, S., 2018, August. *Investigations on friction stir welding of AA5083-H32 marine grade aluminium alloy by the effect of varying the process parameters.* In IOP Conference Series: Materials Science and Engineering (Vol. 402, No. 1, p. 012187). IOP Publishing.

[66] Gharavi, F., Matori, K.A., Yunus, R., Othman, N.K. and Fadaeifard, F., 2016. *Corrosion evaluation of friction stir welded lap joints of AA6061-T6 aluminum alloy.* Transactions of Nonferrous Metals Society of China, 26(3), pp.684-696.

[67] Davoodi, A., Esfahani, Z. and Sarvghad, M., 2016. Microstructure and corrosion characterization of the interfacial region in dissimilar friction stir welded AA5083 to AA7023. Corrosion science, 107, pp.133-144.

[68] Laska, A., Szkodo, M., Cavaliere, P., 2022. *Resistance of Friction Stir-Welded AA6082*. Metals, pp.1-16.

[69] Naumov, A., Morozova, I., Rylkov, E., Obrosov, A., Isupov, F., Michailov, V. and Rudskoy, A., 2019. *Metallurgical and mechanical characterization of high-speed friction stir welded AA 6082-T6 aluminum alloy.* Materials, 12(24), p.4211.

[70] Garg, A., Raturi, M. and Bhattacharya, A., 2019. *Experimental and finite element analysis of progressive failure in friction stir welded AA6061-AA7075 joints*. Procedia Structural Integrity, 17, pp.456-463.

[71] Yokoyama, T., Nakai, K. and Katoh, K., 2018. *Tensile properties of 6061-T6 friction stir welds and constitutive modelling in transverse and longitudinal orientations.* Welding international, 32(3), pp.161-171.

[72] de Giorgi, M., Scialpi, A., Panella, F.W. and De Filippis, L.A.C., 2009. *Effect of shoulder geometry on residual stress and fatigue properties of AA6082 FSW joints.* Journal of Mechanical Science and Technology, 23(1), pp.26-35.

[73] Verma, S. and Misra, J.P., 2021. Experimental investigation on friction stir welding of dissimilar aluminium alloys. Proceedings of the Institution of Mechanical Engineers, Part E: Journal of Process Mechanical Engineering, 235(5), pp.1545-1554.

[74] University of Cape Town, 2020. *Scanning Electron Microscopes | Electron Microscope Unit* .[Image]. < http://www.emu.uct.ac.za/scanning-electron-microscopes> [Accessed 06 June 2021].

[75] El-Shennawy M.O., Abdel-Aziz K.H., Omar A.A., 2017. *Metallurgical and mechanical properties of heat treatable aluminum alloy AA6082 welds*. Int. J. Appl. Eng. Res, 12(11), pp.2832-2839.

[76] Huang, C., Wu, Z., Huang, R., Wang, W. and Li, L., 2017. *Mechanical properties of AA5083 in different tempers at low temperatures.* In IOP conference series: materials science and engineering (Vol. 279, No. 1, p. 012002). IOP Publishing..

[77] Mrówka-Nowotnik, G., Sieniawski, J. and Wierzbińska, M., 2007. *Intermetallic phase particles in 6082 aluminium alloy.* Archives of materials science and engineering, 28(2), pp.69-76.

[78] Atabaki, M.M., Yazdian, N. and Kovacevic, R., 2016. *Partial penetration laser-based welding of aluminum alloy (AA 5083-H32).* Optik, 127(16), pp.6782-6804.

[79] Nam, S.W. and Lee, D.H., 2000. *The effect of Mn on the mechanical behavior of Al alloys.* Metals and materials, 6(1), pp.13-16.

[80] Albannai, A., 2020. *Review the common defects in friction stir welding.* International Journal Of Scientific & Technology Research, 9, pp.318-329.

[81] Safeen, M.W. and Russo Spena, P., 2019. *Main issues in quality of friction stir welding joints of aluminum alloy and steel sheets.* Metals, 9(5), p.610.

[82] Mehta, K.P. and Badheka, V.J., 2016. *A review on dissimilar friction stir welding of copper to aluminum: process, properties, and variants.* Materials and Manufacturing Processes, 31(3), pp.233-254.

[83] Balasubbramanian, V., 2008. *Relationship between base metal properties and FSW process parameters.* Materials science and engineering A, 480, pp.397-403.

[84] Shen, Z., Yang, X., Yang, S., Zhang, Z. and Yin, Y., 2014. *Microstructure and mechanical properties of friction spot welded 6061-T4 aluminum alloy.* Materials & Design (1980-2015), 54, pp.766-778.

[85] Khan, N.Z., Siddiquee, A.N., Khan, Z.A. and Shihab, S.K., 2015. *Investigations on tunneling and kissing bond defects in FSW joints for dissimilar aluminum alloys.* Journal of alloys and Compounds, 648, pp.360-367.

[86] Balos, S. and Sidjanin, L., 2014. *Effect of tunneling defects on the joint strength efficiency obtained with FSW.* Mater Technol, 48(4), pp.491-6.

[87] Kosturek, R., Śnieżek, L., Torzewski, J. and Wachowski, M., 2020. *The influence of welding parameters on macrostructure and mechanical properties of Sc-modified AA2519-T62 FSW joints.* Manufacturing Review, 7, p.28.

[88] Patel, V., Li, W., Wang, G., Wang, F., Vairis, A. and Niu, P., 2019. *Friction stir welding of dissimilar aluminum alloy combinations: state-of-the-art.* Metals, 9(3), p.270.

[89] Wahab, M.A., Dewan, M.W., Huggett, D.J., Okeil, A.M., Liao, T.W. and Nunes, A.C., 2019. *Challenges in the detection of weld-defects in friction-stir-welding (FSW).*

Advances in Materials and Processing Technologies, 5(2), pp.258-278.

[90] Tamadon, A., Pons, D.J., Sued, K. and Clucas, D., 2018. *Thermomechanical grain refinement in AA6082-T6 thin plates under bobbin friction stir welding.* Metals, 8(6), p.375.

[91] Moldovan, P., Stanica, C.N., Ciobanu, G., Ungureanu, I., Iorga, G.M. and Buţu, M., 2014. *Intergranular corrosion of AA 5083-H321 aluminum alloy.* UPB Sci Bull Series B, 76(3), pp.169-180.

[92] Salih, O.S., Neate, N., Ou, H. and Sun, W., 2020. *Influence of process parameters on the microstructural evolution and mechanical characterisations of friction stir welded Al-Mg-Si alloy*. Journal of Materials Processing Technology, 275, p.116366.

[93] Sun, Y., Tsuji, N. and Fujii, H., 2016. *Microstructure and mechanical properties of dissimilar friction stir welding between ultrafine grained 1050 and 6061-t6 aluminum alloys.* Metals, 6(10), p.249.

[94] Scialpi, A., De Filippis, L.A.C. and Cavaliere, P., 2007. *Influence of shoulder geometry on microstructure and mechanical properties of friction stir welded 6082 aluminium alloy*. Materials & design, 28(4), pp.1124-1129.

[95] Hu, J., Wang, X., Zhang, J., Luo, J., Zhang, Z. and Shen, Z., 2021. *A general mechanism of grain growth─ I. Theory*. Journal of Materiomics, 7(5), pp.1007-1013.

[96] Esmaeili, A., Sbarufatti, C. and Hamouda, A.M.S., 2019. *Characteristics of intermetallic compounds in dissimilar friction stir welding: a review.* Metallography, Microstructure, And Analysis, 8(4), pp.445-461.

[97] Nelson, T.W., Lippold, J.C. and Mills, M.J., 1999. *Nature and evolution of the fusion boundary in ferritic-austenitic dissimilar weld metals, Part 1-Nucleation and growth.* Welding Journal-New York-, 78, pp.329-s.

[98] Prangnell, P.B. and Heason, C.P., 2005. *Grain structure formation during friction stir welding observed by the 'stop action technique'.* Acta Materialia, 53(11), pp.3179- 3192.

[99] Frodal, B.H., Dæhli, L.E.B., Børvik, T. and Hopperstad, O.S., 2019. *Modelling and simulation of ductile failure in textured aluminium alloys subjected to compression-tension loading. International Journal of Plasticity,* 118, pp.36-69.

[100] Lumley, R. ed., 2010. *Fundamentals of aluminium metallurgy: production, processing and applications.* Elsevier.

[101] Dickerson, T.L. and Przydatek, J., 2003. *Fatigue of friction stir welds in aluminium alloys that contain root flaws.* International Journal of Fatigue, 25(12), pp.1399-1409.

[102] Li, P., Ma, X., Jia, Y., Meng, F., Tang, L. and He, Z., 2019. *Microstructure and*

mechanical properties of rapidly solidified β-type Ti–Fe–Sn–Mo alloys with high specific strength and low elastic modulus. Metals, 9(11), p.1135.

[103] Palanivel, R., Mathews, P.K., Murugan, N. and Dinaharan, I., 2012. *Effect of tool rotational speed and pin profile on microstructure and tensile strength of dissimilar friction stir welded AA5083-H111 and AA6351-T6 aluminum alloys.* Materials & Design, 40, pp.7-16.

[104] Dilip, J.J.S., Koilraj, M., Sundareswaran, V., Janaki Ram, G.D. and Koteswara Rao, S.R., 2010. *Microstructural characterization of dissimilar friction stir welds between AA2219 and AA5083.* Transactions of The Indian Institute of Metals, 63(4), pp.757- 764.

[105] Banik, A., Roy, B.S., Barma, J.D. and Saha, S.C., 2018. *An experimental investigation of torque and force generation for varying tool tilt angles and their effects on microstructure and mechanical properties: friction stir welding of AA 6061-T6.* Journal of Manufacturing Processes, 31, pp.395-404.

[106] Sahu, P.K. and Pal, S., 2018. *Effect of FSW parameters on microstructure and mechanical properties of AM20 welds*. Materials and Manufacturing Processes, 33(3), pp.288-298.

[107] Marzoli, L.M., Strombeck, A.V., Dos Santos, J.F., Gambaro, C. and Volpone, L.M., 2006. *Friction stir welding of an AA6061/Al2O3/20p reinforced alloy*. Composites science and technology, 66(2), pp.363-371.

[108] Msomi, V., Mabuwa, S. and Merdji, A., 2022. *Correlation Between Heat Input and Mechanical Properties of Submerged Friction Stir Processed TIG-Welded AA8011/AA6082 Dissimilar Joint: Sampling Aspect.* Pakistan Journal of Engineering and Applied Sciences.

[109] Anderson-Wedge, K., Stubblefield, G., Zhu, N., Long, B., Daniewicz, S.R., Allison, P., Sowards, J., Rodriguez, O. and Amaro, R., 2021. *Characterization of the evolution of 2219-T87 aluminum as a function of the friction stir welding process*. International Journal of Fatigue, 142, p.105954.

[110] Kumbhar, N.T. and Bhanumurthy, K., 2008. *Friction stir welding of Al 6061 alloy.* Asian Journal Of Experimental Sciences, 22(2), pp.63-74.

[111] Jata, K.V., Sankaran, K.K. and Ruschau, J.J., 2000. *Friction-stir welding effects on microstructure and fatigue of aluminum alloy 7050-T7451*. Metallurgical and materials transactions A, 31(9), pp.2181-2192.

[112] Leitao, C., Leal, R.M., Rodrigues, D.M., Loureiro, A. and Vilaça, P., 2009. *Mechanical behaviour of similar and dissimilar AA5182-H111 and AA6016-T4 thin friction stir*

welds. Materials & Design, 30(1), pp.101-108.

[113] Luo, Z.C. and Huang, M.X., 2018. *Revealing the Fracture Mechanism of Twinning-Induced Plasticity Steels.* Steel Research International, 89(9), p.1700433.

[114] Lampman, S. ed., 1997. *Weld integrity and performance: a source book adapted from ASM international handbooks, conference proceedings, and technical books*. Asm International.

[115] Kasirajan, T., Ravindran, R., Ramkumar, T. and Selvakumar, M., 2019. *Investigation of the microstructural, mechanical, and thermal evolution of dissimilar aluminium alloys during friction stir welding.* Transactions of the Canadian Society for Mechanical Engineering, 44(1), pp.38-48.

[116] Jweeg, M.J., Takhakh, A.M. and Kareem, N.K., 2015. *Comparison Between Friction Stir Welding (FSW) And Friction Stir Processing (FSP) of AA5086 Aluminium Alloy.* International Journal of Technical Research and Applications, 3(6), pp.205-210.

[117] Moreira, P.M.G.P., Santos, T., Tavares, S.M.O., Richter-Trummer, V., Vilaça, P. and De Castro, P.M.S.T., 2009. *Mechanical and metallurgical characterization of friction stir welding joints of AA6061-T6 with AA6082-T6*. Materials & Design, 30(1), pp.180- 187.

[118] Balos, S. and Sidjanin, L., 2014. *Effect of tunneling defects on the joint strength efficiency obtained with FSW.* Mater Technol, *48*(4), pp.491-6.

[119] Ahmed, M.M.Z., Ataya, S., Seleman, M.M.E.S., Allam, T., Alsaleh, N.A. and Ahmed, E., 2021. *Grain structure, crystallographic texture, and hardening behavior of dissimilar friction stir welded aa5083-0 and aa5754-H14.* Metals, 11(2), p.181.

[120] Kasman, Ş., 2013. *Optimisation of dissimilar friction stir welding parameters with grey relational analysis.* Proceedings of the Institution of Mechanical Engineers, Part B: Journal of Engineering Manufacture, 227(9), pp.1317-1324.

[121] Msomi, V. and Mbana, N., 2020. *Mechanical properties of friction stir welded AA1050-H14 and AA5083-H111 joint: sampling aspect*. Metals, 10(2), p.214.

[122] Raturi, M., Garg, A. and Bhattacharya, A., 2019. *Tensile strength and failure of dissimilar friction stir welded joints between 6061-T6 and 2014-T6 aluminum alloys.* Procedia Structural Integrity, *17*, pp.495-502.

[123] Das, U. and Toppo, V., 2018. *Bending strength evaluation of friction stir welded AA6101-T6 and AA6351-T6 aluminum alloys butt joint*. Materials Today: Proceedings, 5(5), pp.11556-11562.

[124] Wei, W., 2017. *Study of sensitization in AA5083 aluminium alloy*. The University of Manchester (United Kingdom).

[125] Heidarzadeh, A., Mironov, S., Kaibyshev, R., Çam, G., Simar, A., Gerlich, A., Khodabakhshi, F., Mostafaei, A., Field, D.P., Robson, J.D. and Deschamps, A., 2021. *Friction stir welding/processing of metals and alloys: a comprehensive review on microstructural evolution*. Progress in Materials Science, *117*, p.100752.

[126] Kumar, S. and Curtin, W.A., 2007. *Crack interaction with microstructure*. Materials today, 10(9), pp.34-44.

[127] Ponge, D. and Gottstein, G., 1998. *Necklace formation during dynamic recrystallization: mechanisms and impact on flow behavior.* Acta materialia, 46(1),pp.69-80.

[128] Ranjan, R., de Oliveira Miranda, A.C., Guo, S.H., Walbridge, S. and Gerlich, A., 2019. *Fatigue analysis of friction stir welded butt joints under bending and tension load.* Engineering Fracture Mechanics, *206*, pp.34-45.

[129] Xu, W., Liu, J., Luan, G. and Dong, C., 2009. *Microstructure and mechanical properties of friction stir welded joints in 2219-T6 aluminum alloy*. Materials & Design, 30(9), pp.3460-3467.

[130] Çevik, B., Ozcatalbas, Y. and Gülenç, B., 2016. *Effect of welding speed on the mechanical properties and weld defects of 7075 Al alloy joined by FSW*. Kovove Mater, 54(4), pp.241-247.

[131] Ni, D.R., Chen, D.L., Yang, J. and Ma, Z.Y., 2014. *Low cycle fatigue properties of friction stir welded joints of a semi-solid processed AZ91D magnesium alloy*. Materials & Design (1980-2015), *56*, pp.1-8.

[132] Whang, S.H. ed., 2011. *Nanostructured metals and alloys: processing, microstructure, mechanical properties and applications*. Elsevier.

[133] Lin, C.Y., Lui, T.S., Chen, L.H. and Hung, F.Y., 2014. *Hall–Petch tensile yield stress and grain size relation of Al–5Mg–0.5 Mn alloy in friction-stir-processed and post- thermal-exposed conditions.* Materials Transactions, 55(2), pp.357-362.134-135.

[134] Aval, H.J., 2015. *Influences of pin profile on the mechanical and microstructural behaviors in dissimilar friction stir welded AA6082–AA7075 butt joint*. Materials & Design, 67, pp.413-421.

[135] Mabuwa, S. and Msomi, V., 2020. *The impact of submerged friction stir processing on the friction stir welded dissimilar joints.* Materials Research Express, 7(9), p.096513.

[136] Jayabalakrishnan, D. and Balasubramanian, M., 2017. *Friction stir weave welding (FSWW) of AA6061 aluminium alloy with a novel tool-path pattern*. Australian Journal of Mechanical Engineering.

[137] Liu, H.J., Li, J.Q. and Duan, W.J., 2013. *Friction stir welding characteristics of 2219- T6*

aluminum alloy assisted by external non-rotational shoulder. *The International Journal of Advanced Manufacturing Technology, 64(9), pp.1685-1694.*

[138] Chitturi, V., Pedapati, S.R. and Awang, M., 2020. *Investigation of Weld Zone and Fracture Surface of Friction Stir Lap Welded 5052 Aluminum Alloy and 304 Stainless Steel Joints.* Coatings, 10(11), p.1062.

[139] Morozova, I., Obrosov, A., Naumov, A., Królicka, A., Golubev, I., Bokov, D.O., Doynov, N., Weiß, S. and Michailov, V., 2021. *Impact of impulses on microstructural evolution and mechanical performance of al-mg-si alloy joined by impulse friction stir welding.* Materials, 14(2), p.347.